CMOS BASED OPTOELECTRONIC CATHETER LOCALIZATION SYSTEM FOR MAGNETIC RESONANCE IMAGING ENVIRONMENT

by

Baykal Sarıoğlu

B.S., Electrical and Electronics Engineering, Kadir Has University, 2004

M.S., Electrical and Electronics Engineering, Boğaziçi University, 2007

Submitted to the Institute for Graduate Studies in
Science and Engineering in partial fulfillment of
the requirements for the degree of
Doctor of Philosophy

Graduate Program in Electrical and Electronics Engineering
Boğaziçi University
2013

ACKNOWLEDGEMENTS

I have spent eight years of my life in my beloved university. Six of those years were dedicated to the Ph.D. education and research. Those six years made me understand that Ph.D. is not just a way of being a scientist or doing research in a lab putting your white coat on; it is a journey of falling and rising. It is like a thrill ride in an amusement park. It is really frightening; and most possibly an impossible affair without the help of so many people. They are there for you to hold your hand and to whisper your ears that “Everything will be OK”. This page is reserved for those great people.

Family comes first. They always supported me during Ph.D. education and I cannot describe how I am grateful to have such a family. I want to thank my dearest friend Dağhan Gökdel. His “You can do it!” perspective affected my view of life and put me on track. As a brother to me, Okan Zafer Batur helped me during all of my hardest moments in life. Without Ozan Aktan’s rigorous work, Murat Tümer’s practicality and vast knowledge, Berk Çamlı, Umut Çindemir and Işıl Kalafat’s hard working, the project couldn’t be finished. The BETA family; I thank you all. I love them, not because they are worse than me in table tennis, because they are better than me in every other way.

I want to express my gratitude to Prof. Ergin Atalar and his very talented team of students in UMRAM, Bilkent University and Acıbadem Hospital for their support in our MRI experiments.

I would like to express my sincere thanks and appreciation to Prof. Cengizhan Özturk, Prof. Korkut Yeğin, and Prof. Şenol Mutlu for serving on my thesis committee and providing me some invaluable and very innovative ideas.

I would like to thank TÜBİTAK 1001 projects 108E119, 11E197 and Boğaziçi University Life-Sciences Research Center Project (09K120520) for supporting this work.

My supervisor Prof. Arda D. Yalçınkaya gave me to chance to realize this wonderful project and taught me and showed me to become a multidisciplinary person. Lastly, I want to thank Prof. Gunhan Dundar for accepting me to this great university. His endless and vast knowledge always remind me how much I still need to work.

Some says time is the most precious thing in this universe; and I think they are right. Therefore, I want to say how grateful I am to you for giving your precious time to read this text.

Thank you very much.

ABSTRACT

CMOS BASED OPTOELECTRONIC CATHETER LOCALIZATION SYSTEM FOR MAGNETIC RESONANCE IMAGING ENVIRONMENT

The use of minimally invasive medical techniques has greatly reduced risks to patients and has increased our understanding of how the body works. Detection of catheters is one of the most important tasks in these techniques. Magnetic resonance imaging provides a safe environment for catheter driven operations. On the other hand, implementation of catheter localization architectures are problematic due to the impossibility of long conductor usage due to RF induced heating problem in MRI environment. There is a need for devices that use transmission systems other than electrical for realizing catheter driven operations in MRI environment. This thesis presents design and implementation of a micro-system that uses optical transmission for localization of catheters in MRI environment. The micro-system is composed of a radio frequency (RF) integrated circuit (IC) designed in 0.18 μm triple well CMOS technology and optoelectronic components. The RF integrated circuit covers an RF receiver architecture and an optical power supply unit that provides power to the receiver. The power to the system is served by a laser with a wavelength of 660 nm. RF receiver is connected to a micro-coil antenna with a diameter of 2 mm, and it can transmit very low powered magnetic resonance signals to the external environment via a fiber-coupled LED with a wavelength of 1310 nm. The external optical receiver and signal processing unit detect the location of the catheter using the frequency information of the received signal. The implemented system is tested successfully in 3 T MRI environment. The tests show that the system has 350 μm spatial resolution, which proves that the implemented system can be used for the catheter driven minimally invasive operations.

ÖZET

MANYETİK REZONANS GÖRÜNTÜLEME ORTAMINDA KATATER POZİSYON TESPİTİ İÇİN CMOS TABANLI SİSTEM

Minimal girişimsel ameliyatlar gün geçtikçe yaygınlaşarak ve daha büyük bir önem kazanmaya başlamıştır. Bu ameliyatlarda kullanılan kateterlerin tespiti ise ameliyatın başarılı olması için en önemli unsur teşkil etmektedir. Manyetik rezonans görüntüleme (MRG), bu tip ameliyatlar için çok güvenli bir ortam sunmaktadır. Öte yandan, MRG de yer alan yüksek şiddetteki manyetik alan ve kullanılan radyo frekansı (RF) darbe işaretleri katater yer tespiti gerçekleştirecek sistemlerin tasarımı için önemli kısıtlamalar getirmektedir. Bu tip cihazlarda uzun iletken hatların kullanımı, iletken üzerinde yüksek sıcaklıklara sebebiyet vermesi nedeniyle mümkün olmamaktadır. Bu tez MRG ortamında yer tespitini iletken kablolar olmaksızın optik iletişim yöntemleri kullanarak gerçekleştirecek aktif bir mikro-sistem tasarımını ve MRG ortamında başarı ile gerçekleşen deneylerin sonuçlarını sunmaktadır. Mikro-sistem bir $0.18\,\mu$m üçlü kuyu CMOS teknolojisinde üretilmiş bir RF tümdevre ile bunun etrafına yerleştirilmiş optoelektronik komponentlerden oluşmaktadır. RF tümdevre içerisinde bir RF alıcı sistemi ve bu alıcıya güç sağlayan bir optik güç kaynağı bulunmaktadır. Optik güç 660 nm dalga boyundaki bi lazer tarafından sağlanmaktadır. RF alıcı sürekli ve aralıklı olarak çalıştırılabilmektedir. 2 mm çapında bir mikro-anten bağlı olan RF alıcı 120 dB kazanca sahiptir ve çok düşük güçlü MRG işaretlerini çıkışta yer alan 1310 nm dalga boyunda ışık üreten bir LED aracılığı ile dışarı aktarmaktadır. Dışarıda yer alan optik alıcı ve işaret işleme üniteleri ile gelen işaretin frekans değerinden katater 3 T gücündeki bir MRG tarayıcıda başarı ile tespit edilmiştir. Yapılan hesaplamalar MRG alıcının çözünürlüğünün $350\,\mu$m olduğunu göstererek mikro-sistemin minimal girişimsel ameliyatlarında başarı ile kullanıbileceğini ortaya koymuştur.

TABLE OF CONTENTS

LIST OF FIGURES

LIST OF SYMBOLS

Al	Aluminium
A_v	Voltage gain
B_0	Main static magnetic field
B_1	Magnetic field generated by an applied radio frequency pulse
C	Carbon
C	Capacitance
D	Duty cycle
C_{par}	Parasitic capacitance in the DC-DC converter
C_{st}	Stage capacitance in the DC-DC converter
C_S	Storage capacitance
d	Distance
d_s	Slice thickness
d_{coil}	Average diameter of the coil antenna
E_g	Bandgap energy
f	Focal distance
f	Frequency
f_{CLK}	Clock frequency in the DC-DC converter
$f_{\text{isocenter}}$	Isocenter frequency
f_{Larmor}	Larmor frequency
f_{ref}	Reference frequency
f_s	Sampling frequency
F	Flourine
Fr	French scale
G	Gain of a stage
G_d	Gradient magnetic field in d dimension
g_m	Transconductance of the device
Gd-DTPA	Gadopentetate dimeglumine
h	Planck constant

H	Hydrogen
$\mathbf{I}$	Total spin angular momentum
I	Spin quantum number
I_{CC}	Supply current of the discrete component based LNA
I_{DD}	Supply current of the system
I_0	Intensity of the light at the surface of the semiconductor
I_{IN}	Input current
I_{PAR}	Parasitic current
I_{Ph}	Photogenerated current
I_{PD}	Photodiode current
I_S	Supply current of the system
J	First correction factor for the inductance calculation
$\mathbf{J}$	Total orbital angular momentum
k	Boltzmann constant
k_p	Intrinsic transconductance parameter
k_{sw}	Voltage swing ratio
K	Second correction factor for the inductance calculation
K_s	Stability factor
K_s	Potassium hydroxide
L	Lithium
L	Inductance
$\mathbf{L}$	Total orbital angular momentum
l_{coil}	Average length of the coil antenna
L_{coil}	Equivalent inductance of the coil antenna
$\mathbf{M}$	Net magnetic moment
$\mathbf{M}_{xy}$	Net transverse magnetic moment
$\mathbf{M}_z$	Net longitudinal magnetic moment
$\mathbf{M}_{z,eq}$	Net longitudinal magnetic moment at thermal equilibrium
mA	Milli-Ampere
n	Integer number
N	Stage number

n_{coil}	Number of turns in the coil antenna
N	Nitrogen
N_i	Input noise power
N_o	Output noise power
Na	Sodium
NaCl	Sodium chloride
NF	Noise Figure
O	Oxygen
P	Phosphorus
P_{dyn}	Dynamic power losses
P_{min}	Minimum power
P_{out}	Power delivered to the load
P_{res}	Resistive power losses
P_0	Incident optical power
q	Electronic charge
R	Resistance
R_{cf}	Feedback resistance
R_{coil}	Equivalent resistance of the coil antenna
$R_{\mathrm{O,dcdc}}$	Equivalent system resistance
R_i	Spatial resolution
R_λ	Optical responsivity of the material
$R_{\nu 0}$	Frequency resolution
r_O	Small signal output resistance
$R_{\mathrm{O,dcdc}}$	Output resistance of the DC-DC converter
R_{st}	Resistance of the coil antenna with skin effect
S11	Input reflection coefficient
S22	Forward gain
S_i	Input signal power
S_o	Output signal power
Si	Silicon
SNR_i	Input signal-to-noise ratio

SNR_o	Output signal-to-noise ratio
T	Tesla
T	Absolute temperature
T_1	Longitudinal relaxation time
T_2	Transverse relaxation time
T_2^*	Transverse relaxation time with dephasing effects
V_{BE}	Base-emitter voltage
V_{CE}	Collector-emitter voltage
V_{DD}	Supply voltage of the system
v_{in}	Small signal input voltage
V_{in}	Input voltage
v_{mixout}	Small signal output voltage of the mixer
$\overline{v_n^2}$	Noise power spectral density
$\overline{v_n^2}$	Input referred noise power spectral density
v_n^2	Input referred noise voltage density
v_{Iout}	Small signal in-phase output voltage
V_{GS}	Gate-to-source voltage of the transistor
v_{out}	Small signal output voltage
V_{out}	Output voltage
V_{OV}	Overdrive voltage
V_{PD}	Photodiode voltage
v_{Qout}	Small signal quadrature output voltage
V_S	DC-DC converter voltage
V_t	Threshold voltage
W/L	Channel width-channel length ratio
z	Depth
$\mathbb{Z}^+$	Positive integer numbers
α	Absorption coefficient
α_{FA}	Flip angle
α_Q	Voltage gain of the passive network

δ	Skin depth
$\Delta\omega$	Frequency difference
Δt	Temporal difference
η	Power efficiency
η_{quantum}	Quantum efficiency
ξ	Enhancement factor
γ	Gyromagnetic ratio
γ_M	Noise paramater of the device
λ	Wavelength of the light
μ	Magnetic moment
μ_0	Permeability of vacuum
μ_r	Relative permeability of the conductor
ν	Frequency of the light
Ω	Ohm
τ	Time constant
ω_{FID}	Frequency of free induction decay signal
ω_{RF}	Frequency of radio frequency excitation pulse
ω_{RFsec}	Frequency of the secondary radio frequency pulse
ϕ	Phase shift
ρ	Sheer resistance

LIST OF ACRONYMS/ABBREVIATIONS

3D	Three dimensional
AC	Alternating current
BW	Bandwidth
CMOS	Complementary Metal Oxide Semiconductor
DC	Direct current
DC-DC	Direct current to direct current
ESD	Electrostatic discharge
EHP	Electron and hole pair
FA	RF pulse flip angle
FC	Ferrule connector
FET	Field-effect transistors
FID	Free Induction Decay
FF	Fill factor
IC	Integrated circuit
IF	Intermediate frequency
IR	Infrared
LC	Inductor-capacitor
LED	Light-emitting diode
LNA	Low noise amplifier
LO	Local oscillator
MDS	Minimum detectable signal
MEMS	Micro electromechanical systems
MIM	Metal-insulator-metal
MIP	Maximum intensity projection
MOS	Metal oxide semiconductor
MR	Magnetic resonance
MRI	Magnetic resonance imaging
nMOS	n-channel metal oxide semiconductor

NMR	Nuclear magnetic resonance
PCB	Printed circuit board
PV	Photovoltaic
pMOS	p-chanel metal oxide semiconductor
RC	Resistor-capacitor
RF	Radio frequency
RLC	Resistor-inductor-capacitor
RPA	Rectangular pulse flip angle
SMU	Source-measure units
SNR	Signal-to-noise ratio
SOI	Silicon on insulator
TE	Echo time
TR	Repetition time
UMC	United Microelectronics Corporation
VHDL-AMS	Very high speed integrated circuit hardware language for analog and mixed signal
VHF	Very High Frequency

1. INTRODUCTION

Magnetic Resonance Imaging (MRI) is an imaging technique that is used for noninvasively examining the structure and function of tissues from the cellular to the macroscopic level. MRI is advantageous in many ways to the other imaging techniques. The most important advantage is that it does not use ionizing radiation which is harmful for both patient and medical personnel. In addition to this major advantage, its soft-tissue differentiation and its ability to construct images in any plane, as well as its ability of functional analysis of tissues also make MRI as the one of the most preferred conventional noninvasive imaging techniques [9–11].

MRI is based on the interaction between radio waves and nuclei composing the object being examined in the presence of a static magnetic field. This interaction is called Nuclear Magnetic Resonance (NMR) phenomenon. MRI relies on NMR principles. Therefore, an understanding of NMR physics is essential for understanding MRI, and developing new techniques for it.

1.1. Physics of Nuclear Magnetic Resonance

Each proton and neutron contained in the nucleus of an atom has a magnetic dipole moment. Consequently, the nucleus as a whole has a magnetic moment, μ, that depends on the number of protons and neutrons it contains. The expression for the magnetic moment can be written as;

$$\mu = \gamma \mathbf{J}, \tag{1.1}$$

where γ is a nuclei specific constant named gyromagnetic ratio in T/MHz, and $\mathbf{J}$ is the total angular momentum of the particle in kgm^2/s.

The total angular momentum, $\mathbf{J}$, of a nucleus is the sum of total orbital angular momentum ($\mathbf{L}$) and total spin angular momentum ($\mathbf{I}$) vectors. $\mathbf{I}$ is also called the nuclear spin of the particle. **I** value is related to the spin quantum number I of the particle. The spin quantum number is quantized, and hence the nuclear spin is also quantized. I can have values of 0, 1/2, or integers. The interaction of a nucleus with a magnetic field is determined by the I value. I is 0 for nuclei with even atomic number and atomic weight. Such nuclei does not interact with a magnetic filed, hence it is not possible to observe such nuclei in MRI. The nuclei that have integer or 1/2 spin value interact with a magnetic field, and they can be detected by MRI equipment. However, nuclei having spin number of 1/2 ,i.e. ^{1}H (hydrogen), ^{17}O (oxygen), and ^{23}Na (sodium) etc., are the interest of MRI research in medicine. The most common nuclei used in MRI is ^{1}H which is basically a single proton. ^{1}H is highly abundant in biological tissue, and its high sensitivity generates stronger MRI signals.

In the absence of a magnetic field, the nuclear spin and magnetic moment are randomly distributed. The random distribution of individual magnetic moments results in a zero net magnetic moment (**M**=0). In the presence of a net magnetic field, the

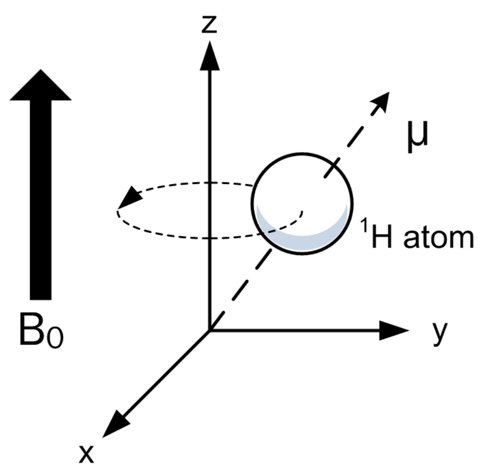

Figure 1.1. Parallel magnetic moment μ of a ^{1}H atom in the presence of a static magnetic field B_0.

spins are aligned with the applied magnetic field, causing them to have individual z components, where z is the direction of the applied magnetic field as shown in Figure 1.1. The alignment can be parallel (low energy) or antiparallel (high energy) to the magnetic field. Thus, the total distributed magnetic moment of the nuclei yield a nonzero net magnetic moment ($\mathbf{M}\neq 0$). Due to the external magnetic field, the spins experience a torque that causes them to precess. At the equilibrium state, the distribution of the transverse component of the magnetic moment is uniform, and the precession is not observable.

The frequency of precession depends on the applied magnetic field B_0, and it is called Larmor frequency. This frequency can be calculated using the Larmor equation;

$$f_{\text{Larmor}} = \gamma B_0, \tag{1.2}$$

where f_{Larmor} is precession frequency in MHz and B_0 is the strength of the external magnetic field in T. Gyromagnetic ratio γ is also the decisive factor for the precession frequency. Each nucleus has a unique precession frequency related to its γ value. Approximate γ values for some common nuclei are given in the Table 1.1.

Table 1.1. Gyromagnetic ratio (γ) values for different nuclei.

Nucleus	γ (MHz/T)
^{1}H	42.576
^{7}Li	16.546
^{13}C	10.705
^{14}N	3.077
^{17}O	-5.772
^{19}F	40.053
^{23}Na	11.262
^{31}P	17.235

^{1}H atom has an approximate γ value of 42.576 MHz. Therefore, if the static magnetic field strength of 1 T is applied to a ^{1}H atom, the atom precesses at a frequency of 42.576 MHz.

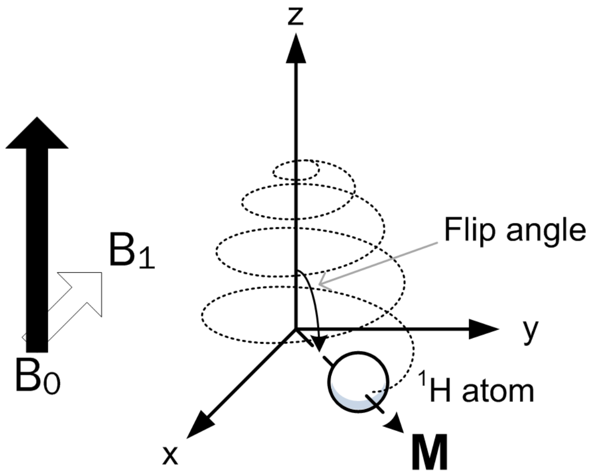

Figure 1.2. 90° RF pulse excitation represented in the stationary (laboratory) frame.

By applying a radio frequency (RF) pulse signal, the magnetic field can be perturbed, and the orientation of the nuclei in the equilibrium state (z direction) can be changed as shown in Figure 1.2. The applied RF signal perturbs B_0 by generating a magnetic field B_1 perpendicular to the z direction. The orientation change is most efficient at the Larmor frequency, since it is the resonance frequency of the particle in the magnetic field. While B_1 is applied, the net magnetic moment vector $\mathbf{M}$ rotates relative to the z axis. The angle of magnetic moment rotation is proportional both to the B_1 amplitude and the pulse duration. The angle can be altered by choosing sufficient B_1 and pulse duration. This rotation angle is usually called "flip angle", and it is an important factor in the design of MRI pulse sequences.

The net magnetic moment vector, $\mathbf{M}$, can be considered as the sum of its longitudinal component vector $\mathbf{M}_z$ and transverse component vector $\mathbf{M}_{xy}$. The magnitude of $\mathbf{M}_{xy}$ and $\mathbf{M}_z$ are inversely proportional, i.e. $|\mathbf{M}_{xy}|$ decreases while $|\mathbf{M}_z|$ increases or vice versa.

When the RF signal is switched off, $\mathbf{M}$ returns to its equilibrium state. This process is called relaxation. Two relaxation times namely T_1 and T_2 times exist. They are independent of one another. T_1 relaxation time is the rate which the net magnetization along with the static magnetic field (longitudinal) direction ($\mathbf{M}_z$) returns to the net magnetization in equilibrium. If the flip angle is 90°, $\mathbf{M}$ is flipped into the

xy plane, $\mathbf{M}_z(0)$=0 and the recovery is simply

$$\mathbf{M}_z(t) = \mathbf{M}_{z,eq}\left(1 - e^{-t/T_1}\right), \tag{1.3}$$

where $\mathbf{M}_{z,eq}$ is the thermal equilibrium value of $\mathbf{M}_z$. The value of T_1 reflects how quickly the energy can be transferred from nuclei to the molecular environment.

Due to the precession motion there is also a net magnetization vector $\mathbf{M}_{xy}$ along xy (transverse) plane. The return to the equilibrium $\mathbf{M}$ from a certain $\mathbf{M}_{xy}$ is defined as T_2 relaxation time. The transformation of $\mathbf{M}_{xy}$ can be expressed as

$$\mathbf{M}_{xy}(t) = \mathbf{M}_{xy}(0)\left(e^{-t/T_2}\right), \tag{1.4}$$

where $\mathbf{M}_{xy}(0)$ is the equilibrium value of $\mathbf{M}_{xy}$.

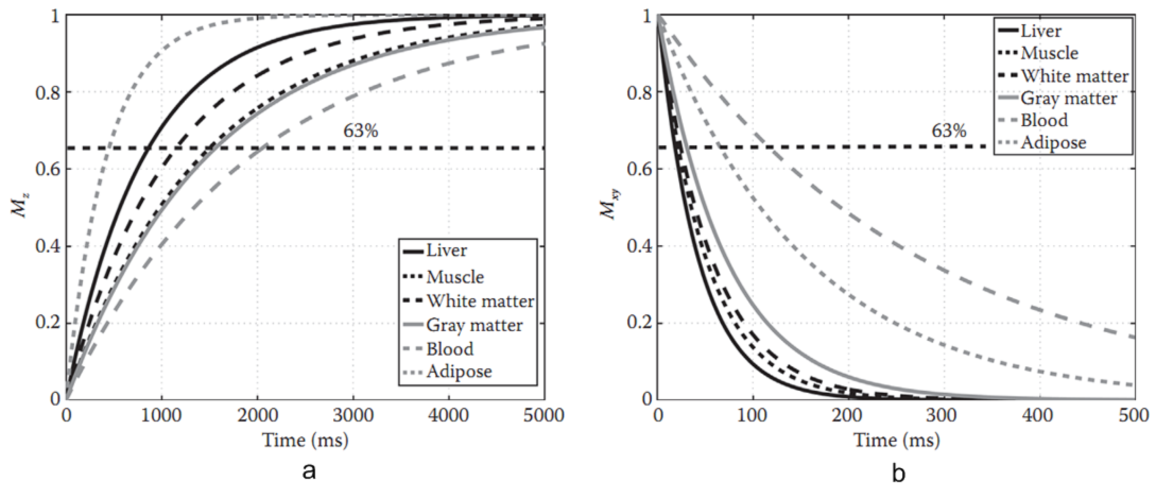

Figure 1.3. (a) T_1 and (b) T_2 relaxation times for sample tissues [1].

The precession motion during the transverse relaxation can be detected by a radio frequency antenna placed in the laboratory frame, as shown in Figure 1.4. The induction of the current on the antenna is determined by the Lenz law. The signal captured is a decaying sinusoidal, henceforth it is called a free induction decay (FID) signal.

Due to the loss of phase coherence in a group of spins, total vector sum of the magnetic moments within a sample decreases, and thus, the FID signal amplitude decreases much quicker than T_2 . The total decay caused by dephasing effects is called T_2^*.

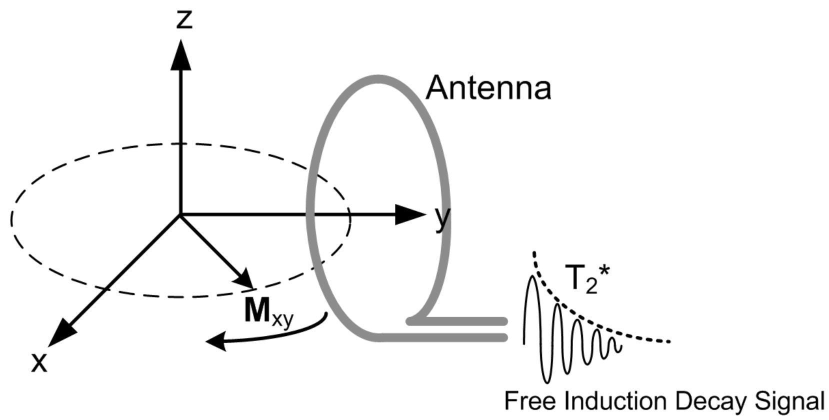

Figure 1.4. Free induction decay (FID) signal induces from transverse magnetization precession by a receiving antenna placed perpendicular to the longitudinal magnetization plane.

Actually, the FID signal is not used imaging applications, since T_2^* process partly destroys the signal. Imaging applications generally use another type of MRI response signal. When a 90° pulse and a 180° are applied sequentially a spin-echo signal shown in Figure 1.5 is induced on the antenna. When the 90° pulse is switched-off, transverse magnetization vector $\mathbf{M}_{xy}$ decays as protons lose phase coherence due to inhomogeneity in the magnetic field. The 180° pulse is applied to restore the phase coherence, and thereby to recover the transverse magnetization. After application of the 180° pulse protons once again lose the coherence. During this procedure a spin echo signal is induced on the antenna. Echo signal can also be generated by a dephasing gradient application. The dephasing gradient is in the negative sign of the readout gradient, and it is applied before the readout gradient. During data acquisition, the readout gradient rephases the spins in the first half of the readout operation. In the second half, the spins dephase again. As a consequence an echo signal is created.

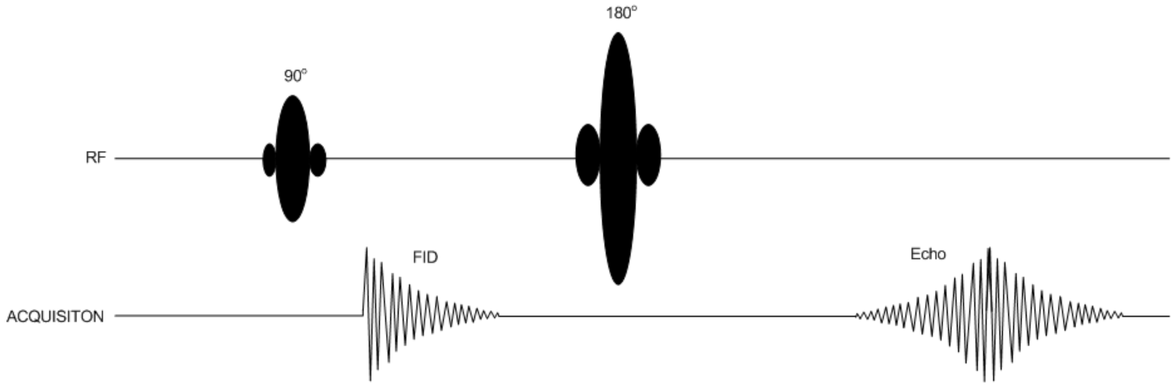

Figure 1.5. Sequential appllication of 90° pulse and 180° pulses result a spin-echo signal.

1.1.1. Localization of Atoms in MRI Environment

Localization of ^{1}H atoms is possible from processing the FID signal. There are two major methods for obtaining the spatial information and detecting the atoms at different spatial locations; frequency and phase encoding.

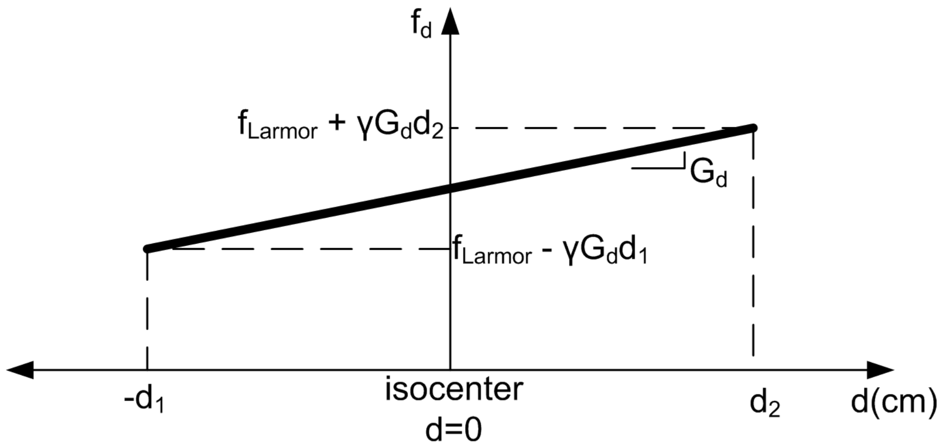

Figure 1.6. Frequency and location relation in frequency encoding in which a gradient magnetic field G_d is applied.

<u>1.1.1.1. Frequency Encoding.</u> In the frequency encoding method, the frequency value of the FID signal is used for extracting the location of the atoms. The frequency of the FID signal is proportional to the applied B_0 as expressed in Equation 1.2. It is evident from this relation that the frequency of the signal can be altered by applying a

gradient magnetic field as;

$$f(d) = \gamma(B_0 + G_d d), \tag{1.5}$$

where G_d is the gradient strength (T/m) at a particular distance d (m) relative to the isocenter (d=0). By incorporating this method, the ^{1}H atoms at each location in a particular dimension will have different frequencies as shown in Figure 1.6, and thus, by detecting the frequency of the captured signal, it is possible to detect and differentiate the location of the atoms.

During utilization of the gradient, a specific slice ($d_1 \leq d \leq d_2$) in the spatial domain is desired to be excited or selected. The corresponding frequency ($f_{d1} \leq f_d \leq f_{d2}$) band can be selected by applying an RF excitation pulse with an envelope of sinc function (sin(t)/t) since its fourier transform corresponds a rectangular band in the frequency domain. In this way, by altering the envelope, desired frequency band can be selected.

In order to visualize a desired slice, series of pulses and gradients are applied sequentially by the MRI scanner. This procedure is called pulse sequence. There are vast number of pulse sequences available for different tasks. Some common pulse sequences used are gradient echo sequence, spin-echo pulse sequence, diffusion pulse sequence, and echo-planar pulse sequence [12].

1.1.1.2. Phase Encoding. The other possible localization method in MRI is phase encoding which is also based on the application of gradient magnetic fields. After an RF pulse, the spins can be considered in phase. When a gradient is applied, the spins have location dependent frequencies and different phases. After the removal of the gradient, the relaxation of each ^{1}H atom to the equilibrium $\mathbf{M}$ generates a phase shift in ^{1}H atoms at different locations.The accumulated phase dispersion can be written as;

$$\phi(d) = \int_{t_1}^{t_2} \gamma d G_d \, dt = \gamma(t_2 - t_1) d G_d, \tag{1.6}$$

where t_1 and t_2 are the starting and ending time of the applied gradient, respectively. The accumulated phase shift $\phi(d)$ is is also unique for different positions (d), and therefore, it can be used for detection of the spatial locations of the ^{1}H atoms in the sample.

1.2. Review of Conventional Catheter Localization Architectures

1.2.1. Catheter Description

Catheters are medical devices that can be inserted in the body to treat diseases or perform surgical procedures. They are, in the most basic form, flexible tubes made out of biocompatible materials. They can be inserted into body cavity, duct, or vessel. Catheters provides drainage, administration of different fluids or gases, access by other surgical means, and also perform wide variety of other medical tasks.

Different catheter sizes are available for different surgical tasks. The sizes are generally given in the French scale which is abbreviated as Fr [13]. Fr value of a catheter is basically calculated as multiplying the diameter of the catheter (mm) by three. For example, if French size is 6, the diameter of the catheter is 2 mm.

The catheter localization is very important for minimally invasive surgical operations where tracking of the catheter movements has an absolute importance. The incomplete or faulty detection of the catheter location can risk the patient's life, and therefore, there is a great need for architectures to track the catheter location successfully.

Currently, X-ray fluoroscopy is widely used for tracking the catheters in surgical operations. However, presence of ionizing radiation present in the X-ray procedures is harmful for the patient and the operating medical personnel. Therefore, it is not possible to realize long duration operations in such environments [14, 15]. On the other hand, MRI provides a safe environment for catheter tracking.

There are number of proposed devices which is specifically designed for catheter localization in MRI environment in the literature. Those devices can be grouped in two basic categories; active and passive catheters.

1.2.2. Passive Catheters

The simplest approach to track a catheter in the MRI environment is placing a magnetic material at the tip of the catheter. This type of devices are named as passive catheters, since no active transmission is involved. The intrinsic material properties, i.e. the magnetic susceptibility [16], of the magnetic material create signal voids (dark spots) and artifacts in the constructed image. These artifacts are basically used for the tracking procedure.

Although it is a very simple method, tracking of the passive catheters is challenging in many ways. The tracking is based on visualization of distortions in the image which can be considered as a detail lost prohibiting some interventional operations. For example, the signal voids can obscure the tissue of interest or vessel walls. Furthermore, the catheter can be lost during the tracking process when it moves out of the selected slice. Therefore, out of slice operation is not possible for the passive tracking devices.

Despite its challenges, successfully conducted passive catheter tracking operations have been reported. CO_2 filled balloon catheters (Figure 1.7a) [2] and catheters that are coated with gadolinium contrast agent, Gd-DTPA, [3, 17] (Figure 1.7b), catheters embody paramagnetic materials [16,18] are successfully tracked in the MRI environment.

1.2.3. Active Catheters

A more advanced method for tracking is usafe an active catheter in which electronic components are placed at the tip of the catheter. Usually micro-coils are used as the electrical component in such devices.

The coil can be used to induce electronically controlled magnetic field inhomo-

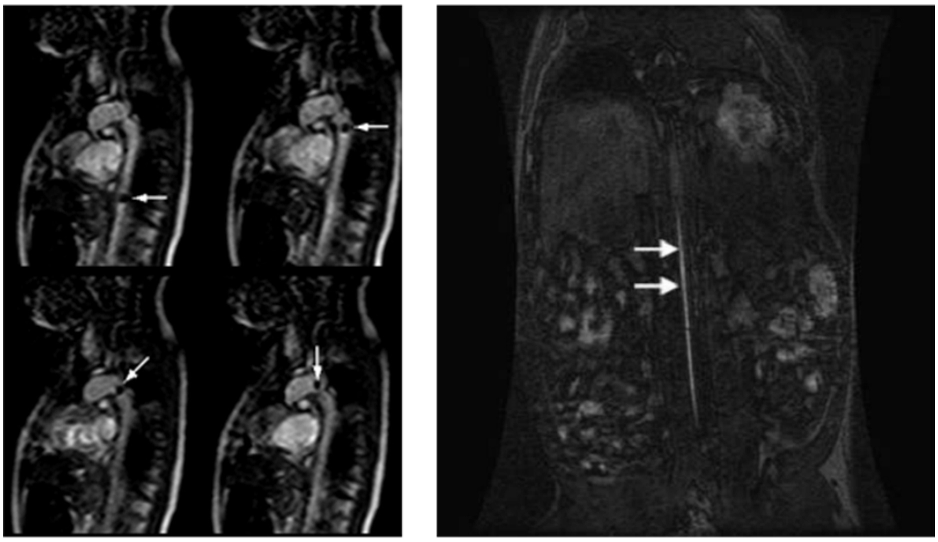

a b

Figure 1.7. Passive tracking examples; (a) CO_2 filled balloon catheter [2], (b) coronal MIP images of a 6-French catheter filled with 4% Gd-DTPA [3]; white arrow shows the position of the catheter.

geneities that cause image distortion [19, 20]. These type of active devices suffer similar limitations to passive devices, since they create signal voids in the image.

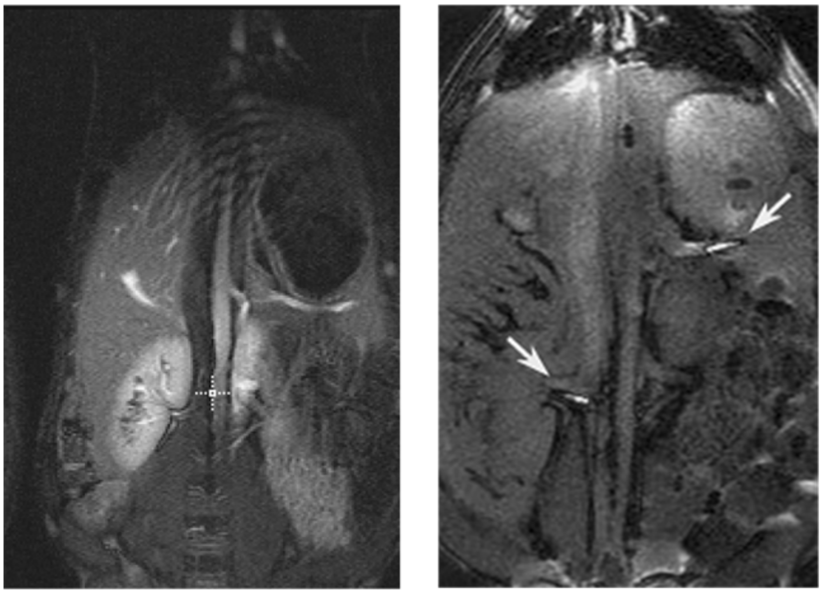

a b

Figure 1.8. Active tracking examples; (a) the position of a 5 Fr catheter is represented by a cross-hair [4], (b) white arrow shows the position of two stents implanted in renal and splenic arteries [5].

A better approach is using the coil for transmission of the FID signals to the outer environment of MRI equipment. This method requires some modifications (e.g. incorporation of non-selective RF pulses) in the pulse sequences used to acquire images. The acquired position is then represented in the image by placing a cursor (or cross-hair) in 2D space [4] (Figure 1.8a). Additional benefit of this approach is that the device can be used for interventional visualization [21] or functional examinations. Moreover, an out-of slice and hands-free solution in which MRI scanner sets its parameters according the data gathered in tracking is possible [22]. Inductive coupling can also be used for realizing a fully wireless localization [5]. In reality, the inductively coupled stents can be considered as semi-active tracking devices which are displayed on the image as white spots (Figure 1.8b) due to their resonance characteristics.

Active catheter designs have the risk of heating during the RF excitation that can generate standing waves along the long conductors [23, 24]. High temperature values up to 74° C have been reported for active devices [25] . Incorporation of detuning or decoupling circuits can be used to decrease the heating problem [26]. The decoupling circuit simply detunes the micro-coil during the RF excitation, and prevents the standing wave generation. The other proposed solution is placing transformers into the transmission lines, but wide spread use of in-vivo active tracking is still limited due to design challenges.

1.3. Motivation of the Thesis

As previously mentioned in the Section 1.2.3, the active devices, currently used for localization of the catheters, suffer from RF induced heating problem. Those devices require electronic systems that can communicate with the external world using transmission means other than electrical. As a solution, communication takes place in the optical medium using components such as fiber optic cables, light emitting diodes, lasers, etc. Optical signal transmission using specifically designed receivers and transmitters is well practiced [27,28]. However, the power is generally transmitted to the systems by electrical means (such as an external battery in the environment [29]) rather than optical in such conditions. The reason behind this preference is that large sized, non-CMOS optical-to-electrical converters, e.g. photovoltaic (PV) cells [30] are required in order to generate sufficient electrical power from optical power for the electronic systems. The other option for obtaining sufficient electrical power is connecting multiple external photodiodes in series [31, 32]. Resulting systems formed by optical-converters and electronic circuits cover large areas in both cases; and thus, they are not convenient for most micro-scale applications (i.e biomedical implants [33–36], sensors [37,38]) where a monolithic approach in which a single on-chip CMOS photodiode is incorporated with the electronic circuits can be more appropriate for such cases. Alternatively, a single CMOS photodiode can only provide voltage levels up to 0.65 V which is considered to be insufficient for most electronic systems that need supply voltages of at least 1.2 V. Connecting CMOS photodiodes in series on the same die can be considered as a solution to this problem; however, since CMOS photodiodes and electronic circuits cannot be connected in series on the same substrate [30], special technologies and processes other than standard CMOS have to be used in the fabrication. [35, 39, 40].

In this thesis, design of an ultra-low power CMOS based optoelectronic catheter localization system implemented in a standard 0.18 μm UMC CMOS triple-well technology is presented as an active device that can be used in MRI environment. Two possible system architectures are investigated in the thesis. Other than the system design, two possible configurations of operation are presented; (i) continuous operation by a set of on-chip CMOS photodiodes and (ii) intermittent operation by a novel optical power supply unit. In summary, the motivation of the thesis is presenting an active device which is more compact, lower cost, much safer, and has a higher sensitivity than the conventional localization devices used in interventional operations. Besides this main motivation, examining other possible system-level architectural approaches are also aimed in the thesis.

1.4. Accomplishments made in the thesis

1.4.1. A novel optical power supply unit

A novel, fully on-chip, optical power supply unit that can convert optical power to electrical power from a single photodiode has been designed and successfully tested. The power supply is novel in the way that a single on-chip photodiode is connected to a DC-DC converter architecture, and this photodiode is the main power source for the overall electronic system. Several CMOS photodiode topologies have been studied and realized. Measurements show that the designed on-chip photodiodes have short circuit current values higher than 15 mA. For accomplishing a proper operation, a novel DC-DC converter architecture that can boost the very low voltage of the photodiode up to 1.8 V has also been realized.

1.4.2. Low power on-chip and discrete component based low noise amplifier design

An ultra low noise amplifier (LNA) having noise figure of 0.4 dB and power gain of 57 dB has been implemented by using discrete components. Using the LNA, localization of micro-coils in 1.5 T MRI environment is carried out successfully.

A fully differential on-chip CMOS low noise amplifier (LNA) with input noise voltage density of $2\,\mathrm{nV}/\sqrt{\mathrm{Hz}}$ with voltage gain of 30 dB has been designed. Measurements show that the designed LNA can still operate appropriately when single on-chip photodiode is used as the power supply.

1.4.3. Low power low noise receiver architectures

Very low power on-chip receivers, which consume approximately 4 mW, have been designed and implemented to process FID signals that has power levels down to -80 dBm. With the experiments, it has been shown that the receivers can successfully operate at the very low power supplied by a single on-chip photodiode. A novel self-mixing receiver architecture is developed in which LNA output is squared by a double balanced mixer.

Custom on-chip protection diodes are implemented to protect the circuit from high powered RF pulses. The receivers are successfully tested in the laboratory and MRI environment without any RF power related damage, which demonstrates the successful operation of the designed protection diodes.

1.4.4. Novel operational schemes

In order to obtain higher power values, an intermittent operation where the charge supplied by the optical power supply unit is transferred to the electronics in short durations is proposed. The switching operation in proposed scheme is also done optically without need for any timing circuitry.

A squaring operation where RF pulses generated by the MRI scanner used as the reference signal is realized instead of on-chip oscillators. It has been shown that the proposed operational scheme does not require additional receiver circuits and it can also be implemented for other MRI related tasks. The overall system is successfully synchronized with the MRI scanner by taking outputs from MRI scanner and processing it by additional electronics which control the modulation of light. Thus, it has also been shown that implementing modulation signals is feasible for a MRI environment using custom pulse sequences programmed.

1.4.5. Fully optical catheter tracking in 3 T MRI environment

The overall system formed by the integrated circuit and optical components is successfully tested in a 3 T MRI scanner using only optical fibers as the communication medium. The location of a 7 Fr catheter sized micro-coil is successfully tracked at several locations in the MRI scanner. To the best of the author's knowledge, the proposed system is the world's first all optical catheter localization system which is designed with a standard CMOS process.

1.4.6. Scientific publications

Two journal papers have been published in scientific journals. While the first paper presents the design of the optical power-supply unit and its integration with a micro electro mechanical system (MEMS) platform [41], the second paper presents the all optical receiver design and the measurements carried out for an example 1.5 T intravascular tracking application [42]. Several conference papers presenting the findings have been presented in national and international conferences [43–47].

Additionally, two journal papers are being prepared to be submitted to scientific journals. The first journal paper present the inherent feedback mechanism in optical power supply unit which can be used as a optical power detector, while the next journal present the results obtained in the MRI experiments of fully optical localization system.

1.5. Organization of the Thesis

The thesis is organized in a way that it shows each step taken during the design process. In Chapter 1, a general system description for an optically powered active device is given together with the experiments realized for determining the system specification. Chapter 2 presents the optical power supply unit design which is the heart of the system. Three generations of integrated circuits are designed. Chapter 3 presents the second generation architecture and the experiments with the system, Chapter 4 the third generation system and final results taken in MRI environment. The last chapter concludes with the comments regarding possible future developments.

2. SYSTEM DESCRIPTION

A top-down design methodology is considered in the design of the overall system. Firstly, the general blocks of the system is determined, and then the blocks are identified by analyzing results obtained from series of experiments carried out in MRI environment.

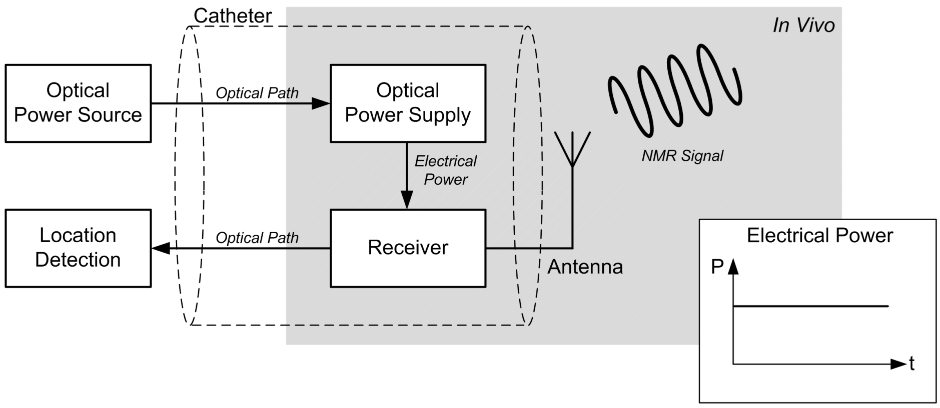

Figure 2.1. A general representation of an optically powered active tracking system; the electrical power is delivered continuously.

The general blocks of an active optical receiver is determined as shown in Figure 2.1. The heart of the system is an optical power supply unit which converts the optical power to the electrical power and delivers it to the rest of the system. The idea is detecting the spin of the atoms where the catheter tip is located, therefore the tip must include an antenna which is connected to an RF receiver. This receiver acquires the induced signal on the antenna and processes it and delivers the information related to the tip position to the outside world via optical means. All of the system components must fit into a Fr 7 catheter which is 2.33 mm in diameter in order to realize an intravascular architecture. The area restriction requires a very compact system which is basically a challenge for any optically powered system, since generally large components are needed for obtaining sufficient electrical power for the electronics.The electronics of the system, which is the receiver, must consume very low power. The low power consumption puts restriction for the receiver, since SNR and minimum power consumption in an analog circuit are proportionally related as;

$$P_{min} \approx 8kTfSNR, \tag{2.1}$$

where k is Boltzmann constant (8.6173×10^{-5} eV/K), T is the operating temperature in Kelvin, and f is the operating frequency in Hz [48].

The other factor is that the information related to the position has to be transmitted optically which requires light emission. This process can be realized by using light emitting diodes (LEDs) which emit light that has luminance linearly proportional to the applied current [49, 50]. Laser diodes are another optical emitters that can be incorporated to the system. Unlike the LEDs, they have to be driven by a current that is greater then a threshold current before emitting light [49, 50]. After this threshold current, the light intensity can be approximated as having a linear relationship with the applied current. Therefore, the required light intensity is an important factor in the power consumption of the architecture. The light emitted from the optical emitter has to have a sufficient intensity to be transmitted through lossy fiber optical cable for detection at the outside of the MRI scanner. The current values that generates sufficient emission is generally in the range of milliamperes which can be considered as a high current requirement for a low power system [49–51]. As a result, obtaining sufficient power in the limited area of the catheter is the determining factor in the design of the overall architecture.

The energy provided by the optical power supply unit can be consumed continuously or intermittently by the receiver circuitry. Both configurations should be investigated before designing the receiver circuitry, since the operation duration will be another major decisive factor in the design of the receiver architecture.

2.1. Continuous Mode Configuration

The continuous mode configuration is the simplest and the most basic configuration in which the receiver is powered by the optical power supply unit continuously.

Advantage of this configuration is that the operation is simple and the data acquisition is continuous. No complex signal schemes are needed. On the other hand, it requires a power supply unit that can deliver power continuously to the receiver; therefore, receiver has to function properly at very low power. However, the low power operation greatly limits the SNR, and thus the minimum detectable signal power. The other drawback is that LEDs and laser diodes require operating voltages closer to or higher than 1 V [49, 51]. An optical power supply unit that can both deliver high voltage and current in a standard CMOS process is a very challenging task to accomplish and may require special fabrication technologies [52–54].

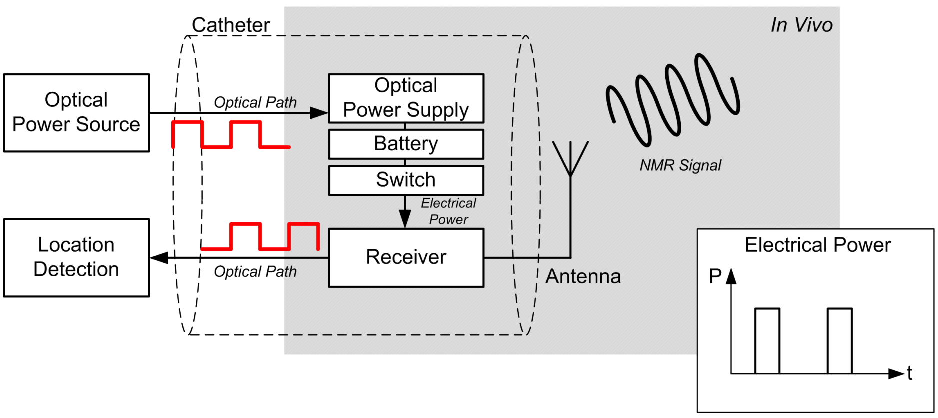

Figure 2.2. A general representation of an optically powered active tracking system operating intermittently; the electrical power is required only during localization.

2.2. Intermittent Mode Configuration

Second possible configuration is the intermittent mode configuration shown in Figure 2.2. In this mode, charge from the supply unit is stored in a battery unit, then the stored charge is delivered to the system for a short period of time through a switch. The receiver operates during this period consuming higher power. As a result, the noise and gain performance is greatly improved for a short period of time. This type of operation is feasible since the localization operation is done intermittently between the imaging operation. These two different operations are required to be implemented in a sequential manner. Once the imaging is done with the imaging sequence, the localization is carried by a localization pulse sequence. Hence, during imaging sequence the system can store the charge, an during the localization the system can use the stored charge. This cycle can continue on in an intermittent fashion.

Required time for charging operation limits the detection time, consequently it limits the obtainable spatial resolution and may prevent realizing real time tracking. Moreover, in this configuration, additional control circuits and a more complex signaling scheme is required. However, this configuration allows to implement very compact designs by eliminating the need for external bulky optical-to-electrical converters.

2.3. Receiver Architecture

The main duty of the receiver is detecting the location of the catheter tip by processing the MRI signal (FID or echo) that is induced on the antenna placed on the tip. Several methods can be implemented for the desired task. Previously in Section 1.1.1, it has been discussed that two possible encoding methods; frequency and phase encoding can be used for localization. The phase encoding requires a reference phase value that makes its utilization impractical for in-vivo applications [55]. In an interventional device case, such reference phase sources (oscillators) can be placed in the body of the patient, and their phase value may not be stable, due to temperature changes (i.e. noise power $\propto$ temperature) [56, 57]. On the other hand, frequency encoding just relies on the value of the frequency of the response signal, that is possible to localize the tip if the frequency of the received response at the antenna is detected [35, 54, 58]. As a result, the frequency encoding is decided to be utilized in the architecture.

The operation frequency of the MRI is related the static magnetic field B_0 by the Equation 1.2. The system is determined to be designed for 1.5 T and 3 T MRI scanners. Hence, the target frequency band for the receiver is between 60 MHz and 150 MHz which is in the Very High Frequency (VHF) band (30 MHz-300 MHz) [59]. The only limitation arises from the frequency band is that on-chip realizations may result a relative large sized monolithic systems. A full on-chip MRI localization system is reported with a size of 1 mm$\times$1.9 mm [58]. With the required additional optical and mechanical components, the overall system that utilizes the aforementioned full on-chip system may not fit into a Fr 7 catheter which is target catheter size in this thesis.

The design criteria for the receiver is set to implement a very compact, low power receiver which does not require high number of fiber optic cables for transmission. Therefore, a single output is desired, and if possible, the other signals should be provided in a wireless manner by the MRI scanner. In terms of power consumption and area, there is no limitation for the external circuitry that extracts the location information from the data transmitted by the receiver. Therefore, the complexity which may lead higher on-chip power consumption can be transferred from the integrated circuit to the outside. However complexity does not mean high power consumption, simplicity is preferred over complexity to obtain much more compact designs. With this purpose, the receivers are investigated from the simplest architecture toward more advanced ones.

2.3.1. Tuned Receiver

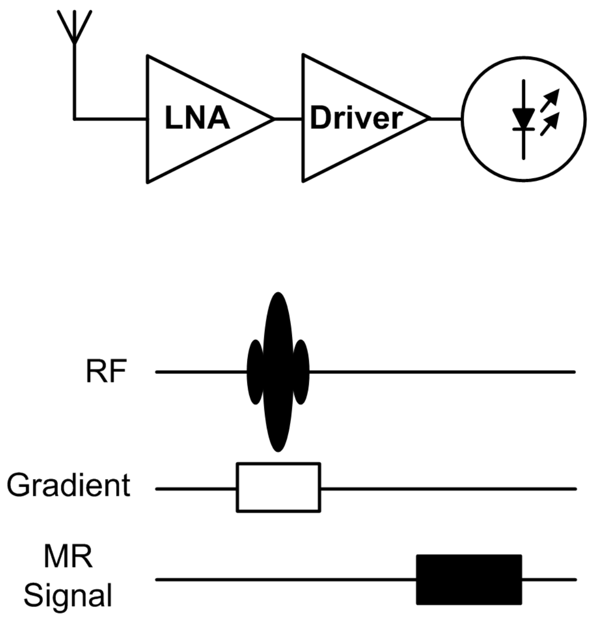

Figure 2.3. The simplest architecture for an active system is sending FID (echo) to the outside optically; the pulse sequence only includes gradients and RF excitation pulse.

The first possible receiver architecture for the desired task is the simple tuned receiver [59] shown in Figure 2.3. In this architecture, the MR response signal is received by a tuned antenna, and it is amplified and transmitted via optical means without any processing. The architecture does not require a complex MR sequence. A non-selective RF pulse is applied together with gradients in three dimensions. A single amplifier can be used to drive the optical emitter [35, 54]. Although the architecture is simple, the high frequency of the MRI response signal cannot be efficiently transmitted through optical emitters (LEDs and LDs) in low power applications. An additional driver may be needed for driving the emitters, which may also increase the power consumption.

Despite of the fact that no integrated circuit solution for this type of architecture is pursued, it is utilized for investigating the MRI signal powers with discrete circuits.

2.3.2. Zero Intermediate Frequency Receiver

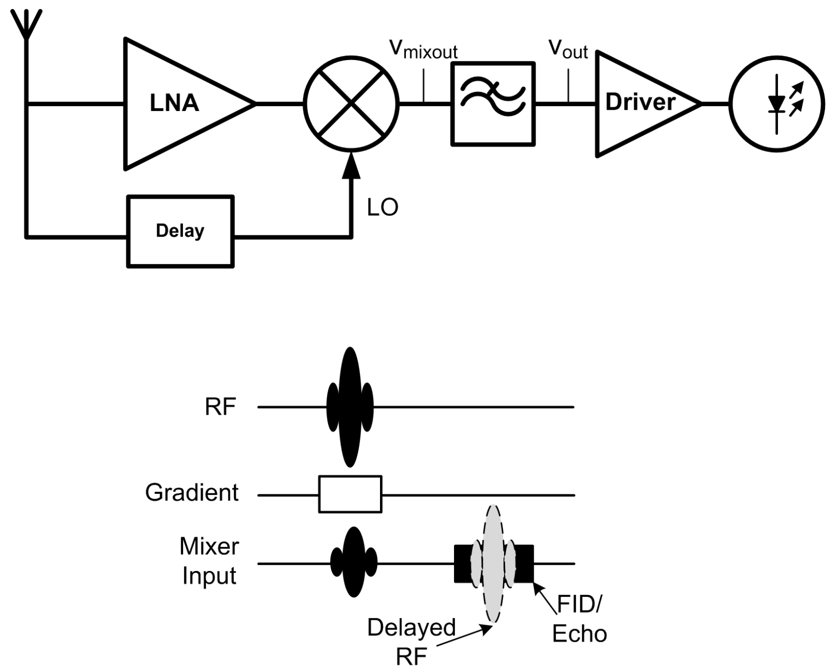

Figure 2.4. Zero-IF architecture in which delayed RF pulse is mixed with MR signal.

The other possible architecture is a zero intermediate frequency (IF) direct conversion receiver architecture shown in Figure 2.4. In zero-IF receivers, the received signal is directly down-converted to the baseband [59–61]. The IF is chosen to be zero. The direct conversion receiver has several advantages over the tuned receiver. The selectivity of the band can be controlled with a simple low-pass filter, gain can be spread through RF and baseband stages. They are simple and low cost, since there is no IF stage (IF amplifier, IF filter, IF local oscillator). However, a local oscillator (LO) with a high degree of precision and stability is needed for the baseband downconversion.

In order not to incorporate a local oscillator (LO) circuitry into the architecture, the RF excitation pulse can be used as the LO signal by delaying it. The delayed RF signal then can be mixed with the MR signal. In this way RF signal acts as a LO signal.

The analog delay requirement is one of the drawbacks of the architecture. The Laplace transform of an ideal delay is;

$$V_{out} = V_{in} \cdot e^{\tau s}, \tag{2.2}$$

where τ is the desired delay. A simple approximation to the ideal delay form can be achieved by first order Pade approximation [62];

$$\frac{V_{out}}{V_{in}} = \frac{1 - \tau s/2}{1 + \tau s/2}. \tag{2.3}$$

The required delay is directly related with T_1 and T_2 relaxation times of the tissue. In Section 1.1, Figure 1.3 lists some relaxation times for sample tissues. The relaxation times are, at best, in 1-100 milliseconds range. In this range, Equation 2.3 converges to $\tau/2$ value. If we assume $\tau = 2RC$ in a simple one-pole system then RC for obtaining a 1 ms delay is simply 5×10^{-4} which is a very impractical value for on-chip realizations. Even with a relatively large 100 pF capacitance value, an impractical value of 50 MΩ resistance is required to obtain desired 1 ms delay.

For the delay line, a Bucket Brigade type circuit may be employed [63]. In this circuit, the input signal is sampled and stored in a cascade of capacitors interconnected by switches operated with the same clock source. However, this type of delay line requires precise control and clock circuitry. Additionally, the charge loss may result a signal loss, and aliasing effects may occur [64].

The other drawback of the zero-IF architecture is that RF excitation pulse corresponds to the isocenter of the MRI scanner. Therefore, the RF excitation pulse is at the center of the MR signal band. If we denote the RF excitation signal at the

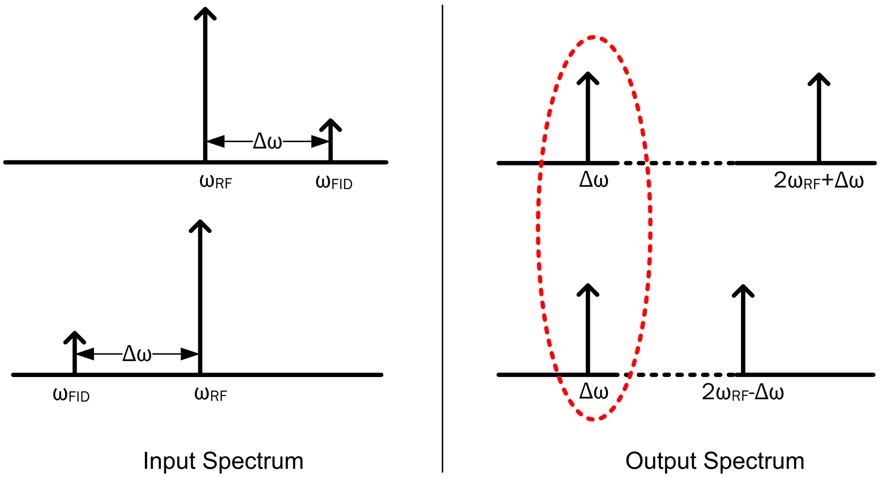

Figure 2.5. Upper and lower sideband inseparability in the zero-IF receiver.

isocenter as $A\cos(\omega_{RF}t)$, and the MR response signal as $B\cos[(\omega_{RF} \pm \Delta\omega)t]$, assuming $\Delta t = n2\pi$ $(n \in \mathbb{Z}^+)$, the output of the mixer can be written as;

$$\begin{aligned} v_{\text{mixout}}(t) &= A\cos(\omega_{RF}t - \Delta t) \cdot B\cos(\omega_{FID}t), \\ &= \frac{AB}{2} \cdot \{\cos[(2\omega_{RF} \pm \Delta\omega)t] + \cos(\Delta\omega t)\}, \\ v_{\text{out}}(t) &= \cos(\Delta\omega t). \end{aligned} \tag{2.4}$$

Please note that for the sake of clarity, the envelopes of the signals are ignored and signals are assumed to be cosine function.

The graphical representation of the expression (2.4) is shown in Figure 2.5. Mixing process results in folding of the spatial domain due to placement of the lower and upper sideband on top of each other, which means that two different halves of the spatial domain of interest is inseparable [60].

This problem is also confirmed by VHDL-AMS simulations in which each block, other than output emitter, is modeled. An example simulation is shown in Figure 2.6. For the example simulation, B_0=1 T and B_1 of the RF excitation pulse is modeled

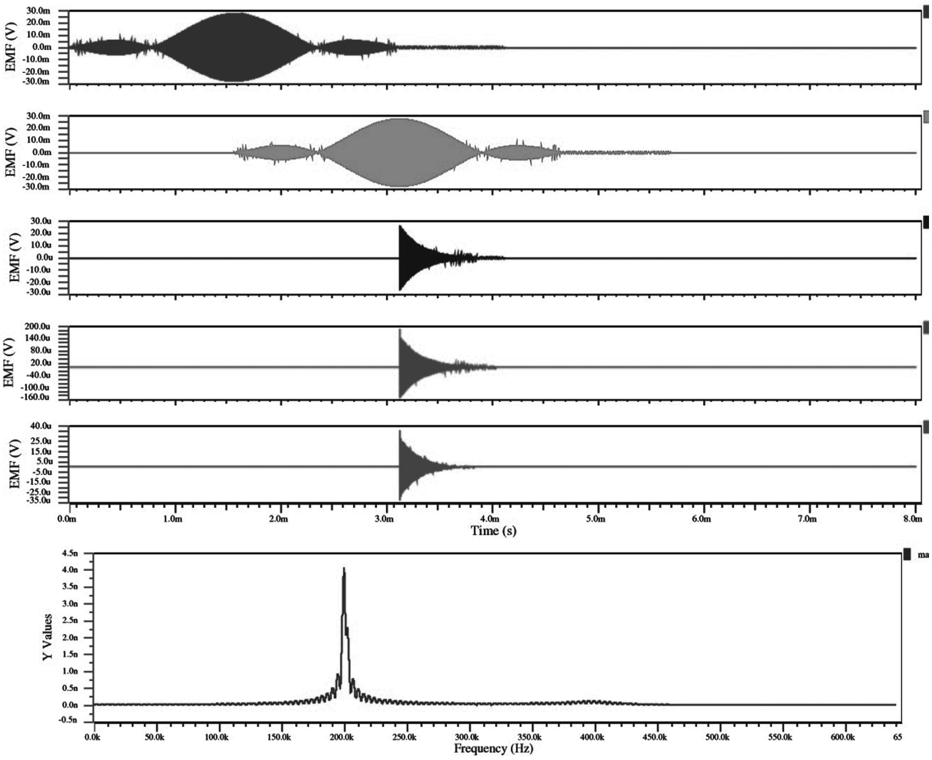

Figure 2.6. VHDL-AMS simulation of the zero-IF receiver; the RF sinc pulse is at 63.86 MHz, FID is at 63.66 MHz, and the delay is set to 1.56 ms.

as [9]

$$B_1(t) = Gd\frac{\sin(kd_s/2)}{kd_s/2}\sin\alpha_{FA}, \tag{2.5}$$

where G strength is 10 mT/m, slice thickness d_s=3 mm, $k = \gamma Gt$, and flip angle α_{FA}=90°. RF sinc pulse is truncated after one side lobe. For the delay τ=1.56 ms. The FID signal is provided at 63.66 MHz, and it is modeled by $e^{-t/250\mu}\sin(2\pi 63.66\times 10^6 t)$ (T_2^* relaxation time is assumed to be 250 μs).The output is as expected found to be at the 200 kHz which is the difference between RF excitation pulse and the FID signal frequencies. The lower and upper side band inseparability is observed while the FID frequency is set to 64.06 MHz. As expected the output is found to be at 200 kHz.

2.3.3. Quadrature Modulation Architecture

Problem related to seperation of left vs right hand side of the isocenter can be solved by realizing the downconversion twice; once with a sine and once with a cosine. The resulting modulation is called quadrature modulation [59, 60, 65]. The zero-IF architecture shown in Figure 2.4 is converted to a quadrature modulation architecture shown in Figure 2.7. In this architecture, delayed RF signal is mixed with the response signal two times in one of them it is shifted 90°. Assuming $\Delta t = n2\pi$ $(n \in \mathbb{Z}^{+})$, expression for the outputs can be written as;

$$\begin{aligned}
v_{\text{Imix}}(t) &= A\cos(\omega_{RF}t - \Delta t) \cdot B\cos[(\omega_{RF} \pm \Delta\omega)t], \\
v_{\text{Qmix}}(t) &= A\sin(\omega_{RF}t - \Delta t) \cdot B\ cos[(\omega_{RF} \pm \Delta\omega)t], \\
v_{\text{Iout}}(t) &= \frac{A \cdot B}{2}\cos(\Delta\omega t), \\
v_{\text{Qout}}(t) &= \pm\frac{A \cdot B}{2}\sin(\Delta\omega t).
\end{aligned} \tag{2.6}$$

The input signal can be reconstructed using v_{Iout} and v_{Qout} by a quadrature demodulator. The problem of the quadrature architecture is evident that two outputs must be transmitted optically, which increases the total block and optical component count that can also be an issue for a small sized catheter. Hence, this type of architecture is not pursued.

2.3.4. Low IF Architecture with Self Mixing

A simpler solution to solve the inseparability problem is to use a LO signal other then the RF excitation pulse. MRI scanner can generate RF pulses at a desired frequency and at a desired power. This inherent property of scanner can be used in advantage to generate a secondary RF pulse which is transmitted while the MRI response is being received. The secondary RF pulse can be placed at a further frequency than the isocenter frequency to resolve the inseparability problem. Additionally, since the secondary RF pulse can be generated at any interval, the delay block can be

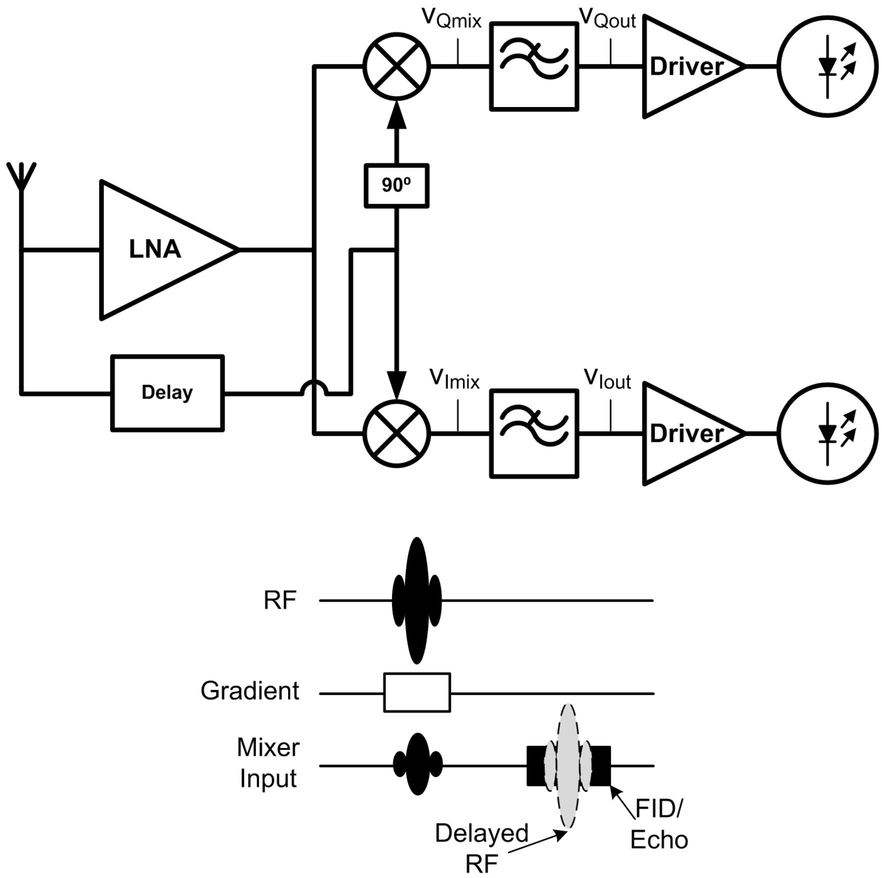

Figure 2.7. Zero-IF architecture is improved to separate the upper and lower sidebands utilizing quadrature modulation.

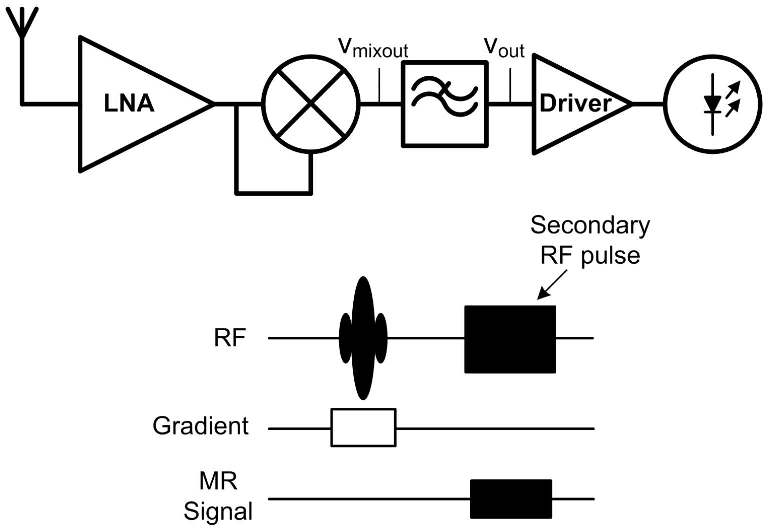

Figure 2.8. A simple low IF receiver with self mixing; a secondary RF pulse which is generated by the MRI scannner is added to the pulse sequence.

excluded from the system. With a self-mixing architecture shown in Figure 2.8, the secondary RF and the response signal can be squared; and, the desired low frequency output can be obtained by filtering. The expression for the self-mixing architecture can be written as;

$$\begin{aligned} v_{mixout}(t) &= \{A \cdot cos(\omega_{RFsec}t) + B \cdot cos[(\omega_{RFsec} \pm \Delta\omega)t]\}^2, \\ v_{out}(t) &= \frac{A^2 + B^2}{2} + AB \cdot cos(\pm\Delta\omega t), \end{aligned} \tag{2.7}$$

where ω_{RFsec} is the frequency of the secondary RF pulse and the MR response is simply modeled as $cos[(\omega_{RFsec} \pm \Delta\omega)t]$.

It is important to note that the amplitude of the secondary RF pulse greatly affects the operation of the device, since it can result a high DC offset value $\left(\frac{A^2 + B^2}{2}\right)$ which may degrade the performance of the electronic circuits [65, 66]. Therefore, preferably a secondary RF signal that has power in the range of the MRI response signal is desirable.

This architecture is employed in the system design. However, the LNA output is not connected to the mixer input directly. Mixer inputs are kept open to allow connecting other LO signal sources. If self mixing is desired, LNA outputs is connected externally.

2.4. Characterization of the Micro-coil Antenna

Minimally invasive tracking and localization operations require very small sized radio frequency antennas that can fit into the catheters with millimeter long diameter. Due to their small sizes, these antennas are named as micro-coils (or μ-coil). There are various micro-coil designs proposed in the literature. However, traditionally, they can be grouped in two main categories; solenoidal, planar coils.

Micro solenoid coils are used extensively in minimally invasive NMR and MRI research [22, 67–71]. They can provide homogeneous magnetic field even with a small number of turns and size. They can be wounded by hand, a process is shown to be feasible down to a diameter of 50 μm [70]. They have intrinsically higher sensitivity compared with designs such as saddle or birdcage [72, 73], hence they can conform to the size of small samples, and thus SNR obtained for a fixed sample volume generally increases as coil dimensions are reduced [74].

Planar antennas are coil structures that are manufactured in a planar fashion on a substrate. They are advantageous in the way that they can be produced by flexible polymer materials which enables them to be wrapped around the catheter. Planar microcoils are relatively easy to fabricate using standard lithographic techniques. They can have diameters in the range of 100 μ to 500 μm [75, 76].They can also be designed monolithically with the integrated circuits [58]. The mainly adopted design for the planar antennas is the spiral design shown in Figure. The sample can be placed on the coil while the coil is oriented perpendicular to the static magnetic field B_0. This type of coils usually have poor homogeneity in the center region due to the fields generated by the eddy currents in the region. Caused by the planar nature of them, their inductance value is also much lower than the solenoidal counterparts.

A solenoidal coil is determined to be used as the antenna to pick up MRI signals due to its higher SNR performance and higher availability.

2.4.1. Electrical Model

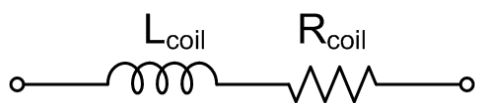

Figure 2.9. The equivalent circuit model for the receiver solenoidal coil.

The equivalent circuit model of a solenoid coil is given in Figure 2.9 shows that the coil as an inductor, L_{coil}, in series with a parasitic resistance, R_{coil}. The inductance (L_{coil}) value for a micro solenoidal coil can be calculated as

$$L_{\text{coil}} = \frac{9850 d_{\text{coil}} \cdot n_{\text{coil}}^2}{4.5 + 10(l_{\text{coil}}/d_{\text{coil}})} - 628 d_{\text{coil}} n_{\text{coil}} (J + K)[nH], \tag{2.8}$$

where n_{coil} is the number of turns, d_{coil} is the average diameter, and l_{coil} is the average length of the coil expressed in meters. J and Kvalues are empirically found correction factors.

J value only depends on the diameter d_{coil} of the coil wire and spacing s_{coil} between the adjacent wires as;

$$J = 2.33log_{10}\frac{d_{\text{coil}}}{s_{\text{coil}}} + 0.515. \tag{2.9}$$

K depends only on the number of turns, however, its values are given graphically since an analytic explanation is not possible [6]. Some K values are given in Figure 2.10.

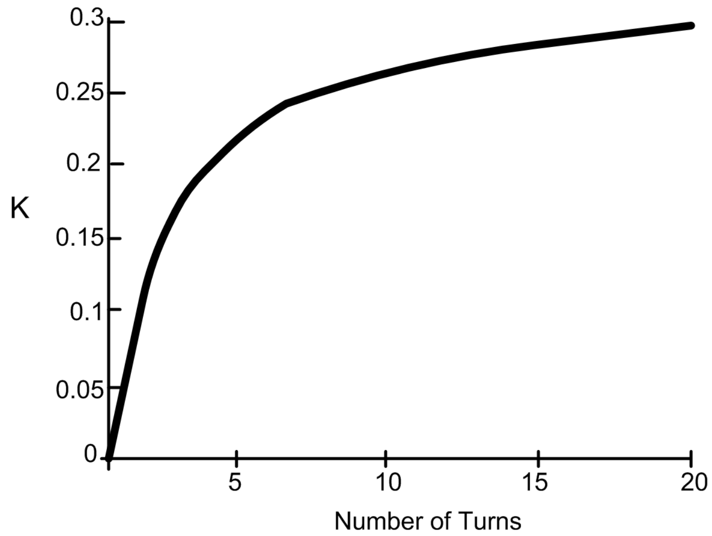

Figure 2.10. K correction factor for calculating self-inductance of a solenoid [6].

The solenoid can be accepted as a straight wire with a length of $l = n\pi d_{\text{coil}} + l_{\text{coil}}$. However, at high frequencies, due to eddy currents generated in the conductor, the current has a larger density near the surface. The depth at which the current density falls to 1/e of its surface value is called skin depth (δ) [6]. The value of the skin depth can be calculated as

$$\delta = \sqrt{\frac{\rho}{\pi\mu_0\mu_r f}}, \tag{2.10}$$

where ρ is the resistivity of the coil material, f is the operation frequency, and $\mu = \mu_0\mu_r$, where $\mu_0 = 4\pi 10^{-7}$ Tm/A is the permeability in vacuum, and μ_r is the relative permeability of the conductor. With the added skin effect, the resistance can be estimated as

$$R_{st} = \frac{l_{\text{coil}}}{d_{\text{coil}}}\sqrt{\frac{\mu\rho f}{\pi}}. \tag{2.11}$$

However, solenoid structure of the coil causes additional eddy currents that are induced in each turn by the changing magnetic fields in the adjacent turns. The dissipation due to this power reflects as a real resistance. By adding the proximity effect, the resistance of a solenoidal coil can be expressed as

$$R_{\text{coil}} = R_{st}\xi, \tag{2.12}$$

where ξ is an enhancement factor describes an enhancement factor that results from the proximity of adjacent turns.

2.4.2. Experimental Results

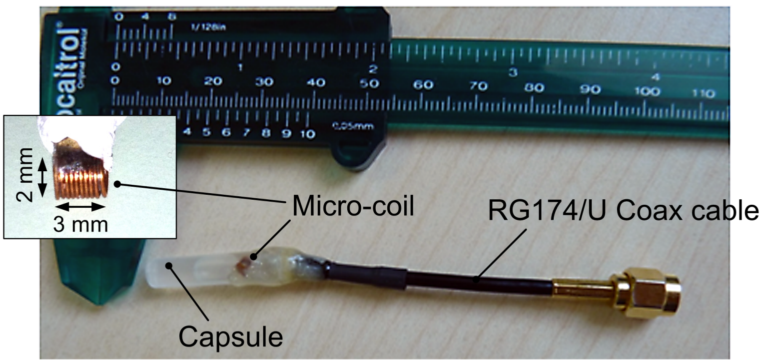

Figure 2.11. Photograph of the implemented micro-coil which is placed in a plastic capsule that is filled with 0.9% NaCl solution; and then, it is attached to a 6 cm RG174/U coaxial cable.

For test purposes of the receiver, a copper wire of 200 μm thickness was used to wind a coil with 10 turns. The coil had an average diameter (d_{coil}) of 2 mm, and an

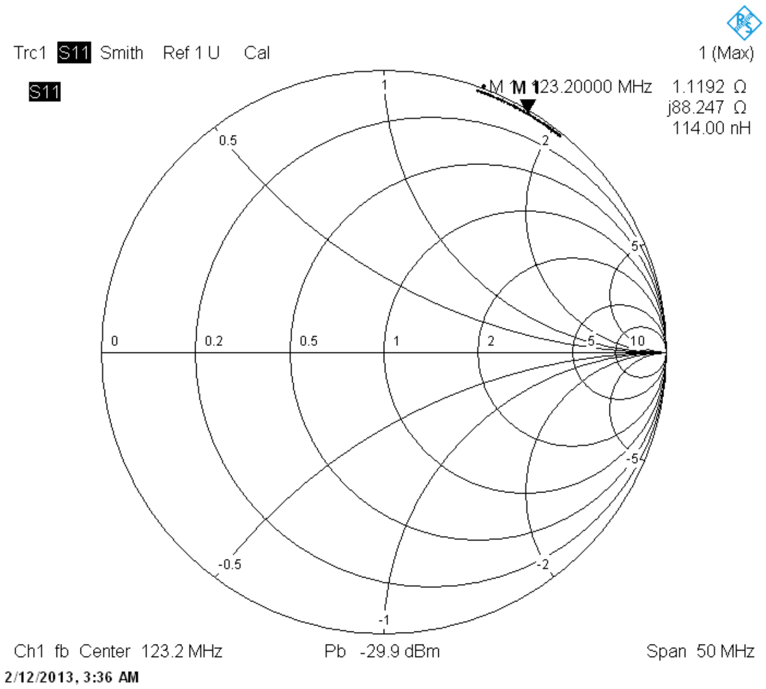

Figure 2.12. S11 measurement of the micro-coil which has self inductance L_{coil} of 114 nH and R_{coil} of 1.1 Ω at 123 MHz.

average length (l_{coil}) of 3 mm. The impedance measurement of the coil was performed using a vector network analyzer (Rohde Schwarz ZVB4). Figure 2.12 shows the measured values that are found for the air core coil as L_{coil}=114 nH and R_{coil}=1.1 Ω at 123 MHz. L_{coil} value for the coil is calculated using Equation 2.8 as 78 nH and the resistance is calculated as 1.36 Ω. The inductance value increases to 422 nH with the additional inductance of the coaxial cable and increased self inductance due to the higher permeability of the NaCl solution.

2.5. Determination of the Receiver Specifications

In order to determine gain and noise figure requirements, several discrete based electronic circuits are designed and tested in the MRI environment. Optical transmission is not targeted in the experiments. The output signal is transmitted electrically via custom made choked coaxial cables. The power is provided to the circuits by MRI compatible non-magnetic batteries.

In order to determine the power of the MRI FID and echo signals, a discrete

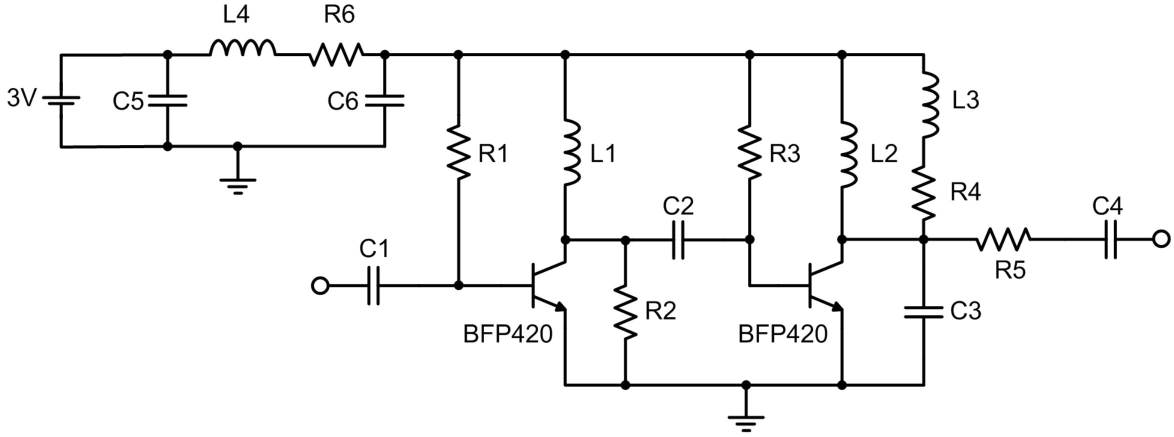

Figure 2.13. Schematics of the discrete component based two stage amplifier.

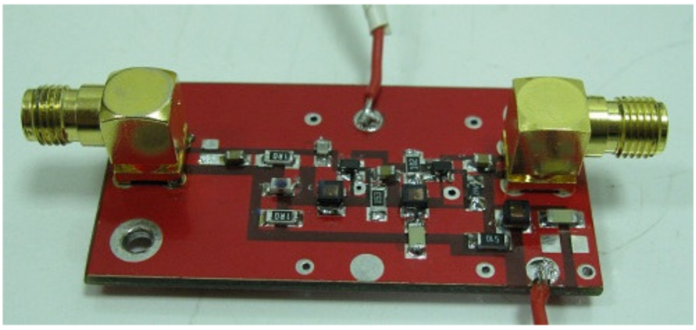

Figure 2.14. Manufactured discrete component based two stage amplifier.

component based two stage amplifier shown in Figure 2.13 is designed. Infineon BFP420 SIEGET transistors are selected to be used in the design, due to their low noise figure (1.1 dB at 1.8 GHz) and high power gain (21 dB at 1.8 GHz) values. The coil antenna is matched to 50 Ω and the noise matching for the PCB is done by properly biasing the first stage [77, 78]. The second stage provides voltage gain by the implemented LC peaking at 65 MHz (50 nH and 120 pF). The component values used in the design are listed in the Table 2.1.

The implemented two-stage amplifier consumes 42 mW total power (14 mA at 3 V supply voltage). Simulated and measured forward gain (S21) of the amplifier are shown in Figure 2.15a. At 64MHz, the amplifier has 58 dB forward gain (S21), and the noise figure is measured as 0.4 dB using HP8970B noise figure meter. Figure 2.15b shows that the stability factor K_s [79] is greater than one (i.e. $K_s > 1$) indicating that the amplifier is unconditionally stable. Simulation of the input reflection (S11) of the amplifier is shown in Figure 2.16. The simulated and measured values for the LNA are listed in Table 2.2.

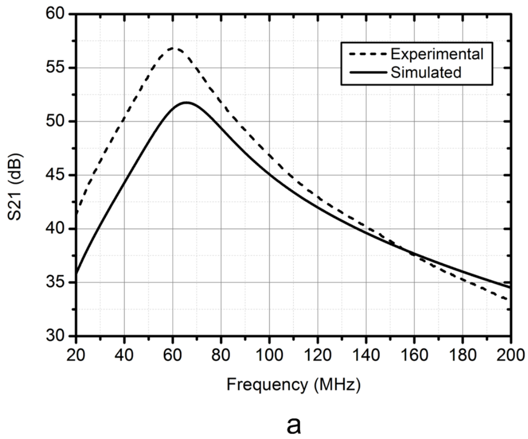

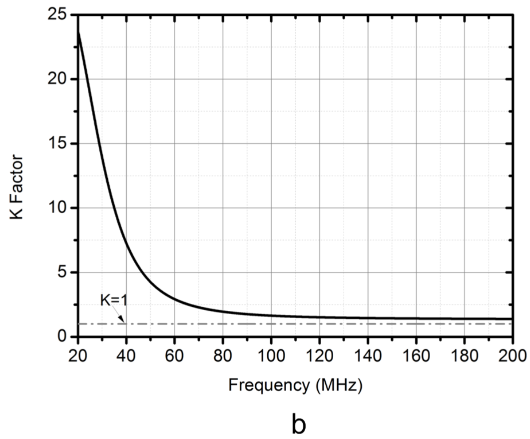

Figure 2.15. (a) Measured and simulated forward gain (S21), (b) Stability (K) factor simulation result of the two stage amplifier; K>1 in the spectrum, thus amplifier is unconditionally stable.

The experiments is carried out in a 1.5 T Siemens Espree MRI scanner in Acıbadem Hospital, Istanbul. The amplifier is used in a tuned receiver configuration. The solenoid coil described in Section 2.4 is connected to the amplifier. The output is transmitted to a Tektronix DPO4014B oscilloscope via a choked coaxial cable. Photograph of the experiment setup is shown in Figure 2.17. A simple spin echo sequence is applied with following specifications; Repetition Time [1] (TR)=5000 ms, Echo Time (TE)=40 ms,

Table 2.1. Component values used in the discrete component based two stage amplifier.

Component	Value	Component	Value
$C1$, $C2$, $C4$, $C5$, $C6$	100 nF	$R2$	1 kΩ
$C3$	120 pF	$R3$	15 kΩ
$L1$, $L2$, $L4$	1 μH	$R4$	5 Ω
$L3$	50 nH	$R5$	5 Ω
$R1$	27 kΩ	$R6$	50 Ω

[1]The reader is referred to Section A to see the definition of these MRI related parameters.

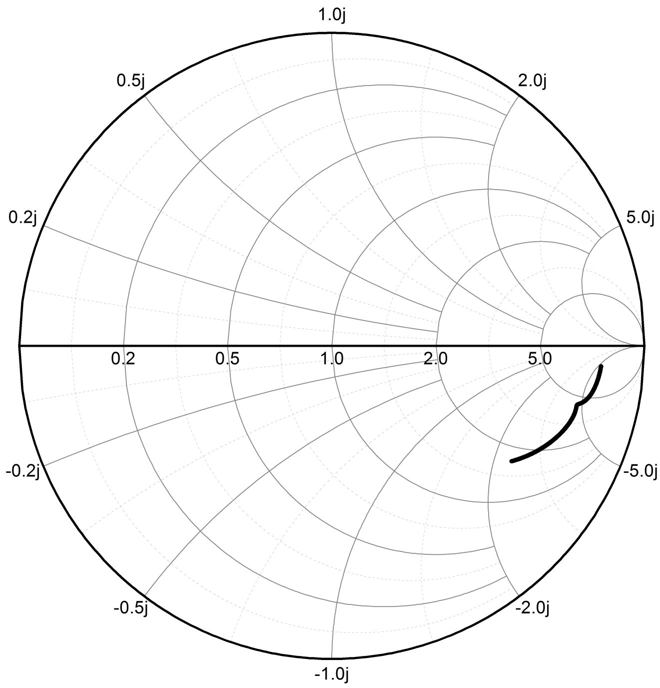

Figure 2.16. Input reflection (S11) simulation result of the two stage amplifier in the frequency range of 20 MHz-200 MHz.

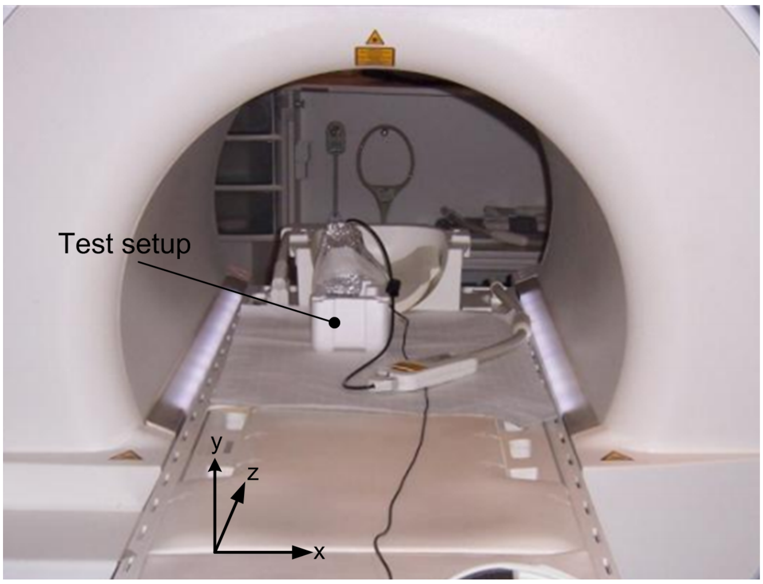

Figure 2.17. Experiment setup for the discrete component based circuitry in a 1.5 T MRI scanner.

Field of View (FoV)=300 mm, bandwidth= 750 Hz/pixel, resolution= 256×256, slice thickness=20 mm, $f_{\text{isocenter}}$= 63.622162 MHz. 300 mm field of view is represented by 256 pixels, thus one pixel has a length of 1.171875 mm. Since the bandwidth is 750 Hz/pixel, the expected frequency resolution for 1 cm can be calculated as 6.4 kHz.

Three coil positions in x (lateral) dimension, center, 8 cm right to the center, 8 cm left to the center are tried to be located. In order to locate the catheter, obtained time domain signals are converted to frequency domain with a Fourier transform algorithm in MATLAB software. The spectrum of these signals are shown in Figure 2.18. The frequencies of the coil positions are found to be 63.62 MHz, 63.57 MHz, and 63.67 MHz respectively. The coil positions can been calculated from the frequencies as $d_x = (f_{\text{isocenter}} - f_{d_x})/6400$ where d_x is the coil location in cm, f_{d_x} is the measured frequency. The calculated locations perfectly match to the measured values.

The experiment shows that the front-end of the receiver should have a voltage gain around 60 dB. The low noise operation is also important due to the fact that the experiment shows that the power of the MRI echo signals are lower than -50 dBm. Nevertheless, the linearity of the receiver is not critical, since the signals are very low power, and no interference is detected in the band. As a result, the integrated receiver is determined to have 60 dB voltage gain and sub-1 dB noise figure value.

Table 2.2. Comparison of simulation and experimental results for the implemented discrete component based LNA.

	Simulation	Experimental		Simulation	Experimental
V_{BEQ1}	0.976 V	0.833 V	V_{BEQ2}	0.996 V	0.846 V
V_{CEQ1}	2.38 V	2.05 V	V_{CEQ2}	2.38 V	2.05 V
I_{CC}	12.5 mA	14 mA	$S21$	51.8 dB	58 dB
NF	1.1 dB	0.4 dB	-	-	-

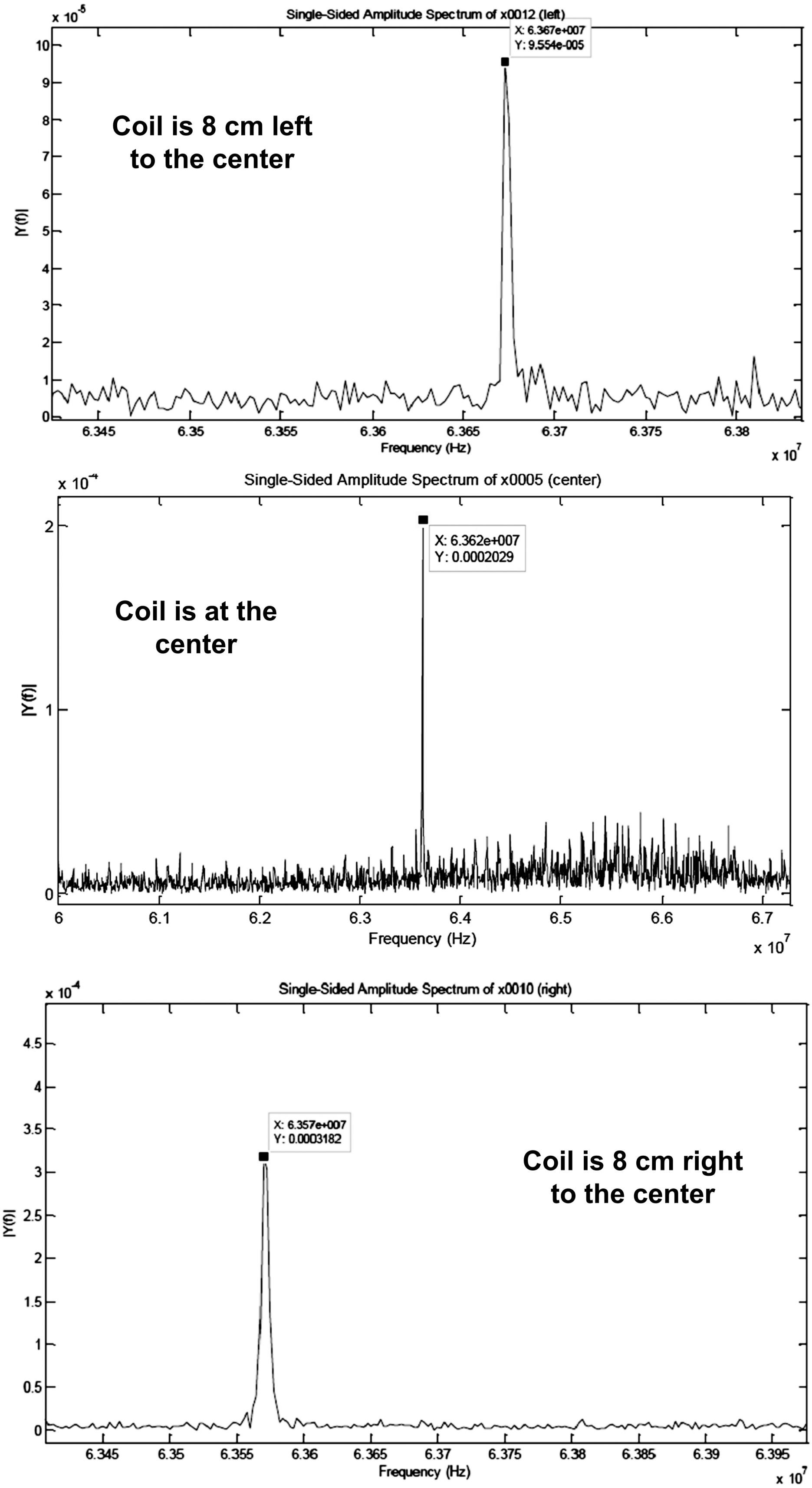

Figure 2.18. Frequency spectrum of three different coil locations detected in 1.5 T MRI scanner; the frequencies of the coil positions are found to be 63.67 MHz, 63.62 MHz, and 63.57 MHz respectively.

3. OPTICAL POWER SUPPLY UNIT

Optical powering is based on the principle of converting the optical power to electrical power and supplying the converted electrical power to the electrical system. There are three sub-blocks in any optical powering system. An optical power source (e.g. laser), a transmission medium (e.g. fiber optic cable) and an optical-to-electrical converter (e.g. photovoltaic cell). The blocks of the overall system should be selected specifically for a target application or environment.

Although photovoltaic cells have been frequently used as the optical-to-electrical converters, they are not convenient for micro-scale electronic systems such as biomedical implants and sensors which demand much more compact optical-to-electrical converters [33–38]

Photodiodes are another option for the optical-to-electrical converter and due to their small size, they could be used as the converter for such micro scale electronic systems. Discrete photodiodes can be utilized to supply the power to the integrated circuit [80]. However, integration and packaging of such devices are problematic due the increased complexity. Series connection of multiple photodiodes is also possible as a solution to reach desired supply voltage value. However, the light has to be uniformly distributed to serially connected photodiodes to obtain the maximum efficiency which restricts the laser beam size and therefore intensity. Another critical point about this configuration is that complexity and the total size of the optical power supply unit are increased by increased number of photodiodes. For these reasons, discrete photodiode based solutions are determined to be improper for an active interventional tracking device.

An on-chip solution is much more convenient for obtaining a compact size. Silicon on insulator (SOI) technology can be utilized to connect multiple photodiodes in series.As reported in the literature, in this way, a 50 V supply is generated by the series connection of 90 cells [37]. On the other hand, SOI process is a relatively expensive technology, which makes it a unsuitable technology for low cost realizations. A CMOS power supply unit that can be integrated with the electronics is favored due to its low cost and high integrability properties. However the very low power conversion efficiency, which is more pronounced in the sub-micron CMOS technologies, makes the design of a photodiode based monolithic optical power supply system challenging. Therefore, the number of attempts incorporating an on-chip photodiode to an optical power supply unit has remained very limited.

The challenge of realizing an on-chip optical power supply unit is that the unit should be able to supply voltage higher than the open-circuit voltage of a single on-chip CMOS photodiode (i.e. 0.6 V). Realizing very low voltage electronic circuits that can operate at a single photodiode voltage is possible, but high gain and dynamic range requirements of the required receiver, and the need for an output optical emitter that require turn on voltages close to 1 V may not be possible with on-chip photodiodes. A DC-DC converter may be required to boost the photodiode voltage to attain a sufficient supply voltage value.

3.1. Proposed Design

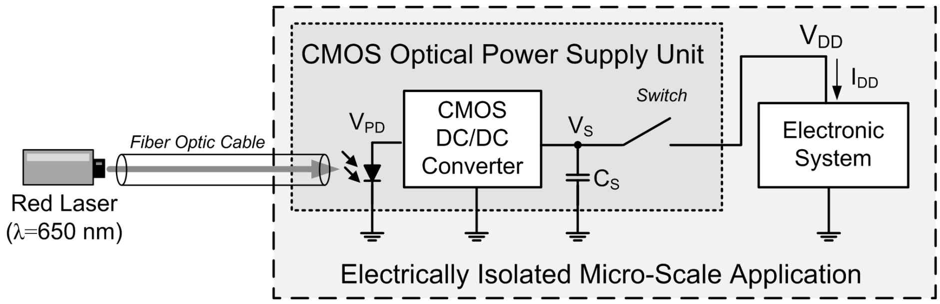

Figure 3.1. The architecture of the proposed CMOS power supply unit.

The architecture of the designed CMOS power supply unit and its utilization in an electrically isolated micro-scale application are shown in Figure 3.1 [81]. The operation principle of the proposed unit can be described as follows; the light from an optical power source (most commonly a laser) is transferred through a medium (in air or through a fiber-optic cable) to the on-chip photodiode of the proposed unit. The low voltage on the photodiode (V_{PD}) generated by the light from the optical power source serves as the input voltage for the DC-DC voltage converter, where the photodiode voltage is stepped up to a higher level (V_S) which is sufficient for an electronic system. The output voltage V_S could be used directly or an additional storage capacitor (C_S) can be used to accumulated charge that can be transferred directly to any electronic system via a switch. This operation corresponds to the intermittent configuration described in Section 2.2. Intermittent operation enables supplying more current (I_{DD}) at a voltage level (V_{DD}) for applications [42, 82].

3.2. CMOS Photodiodes

A photodiode is basically a p-n junction that is exposed to an incident light. Therefore, study of semiconductor behavior under an incident light is essential.

A photon that has higher energy than the bandgap energy of the semiconductor ($h\nu > E_g$) may cause an electron-hole pair generation, which results photogenerated current flow [49]. Bandgap of the silicon material is 1.12 eV at the room temperature, thus light that has lower energy than this value cannot generate a photogenerated current flow. The energy of light is inversely proportional, and photon with a wavelength longer than 1100 nm cannot generate a current flow in the silicon material. The lower limit for the silicon is defined by excess generation of electron-hole pairs at the surface. Photon with a wavelength shorter than 400 nm does not contribute the photogeneraed current flow. As a result, silicon material is sensitive to the light in the range of 400 nm-1100 nm.

The light intensity is exponentially decreases while light propagates in the semiconductor. The intensity of the light can be defined as

$$I = I_0 e^{-\alpha z}, \tag{3.1}$$

where I_0 is the intensity of light at the surface, and z is the depth, α is the absorption coefficient of a material that describes the probability of photogeneration. Absorption coefficient for some materials are depicted in Figure 3.2. The penetration depth for a material is defined as the depth value where the 63% of absorption occurs. This value corresponds to $1/\alpha$. α is wavelength ($\alpha(\lambda)$) dependent and it can be calculated for silicon as;

$$\alpha(\lambda) = 10^{13.2-36.7\lambda+48.1\lambda^2-22.5\lambda^3}. \tag{3.2}$$

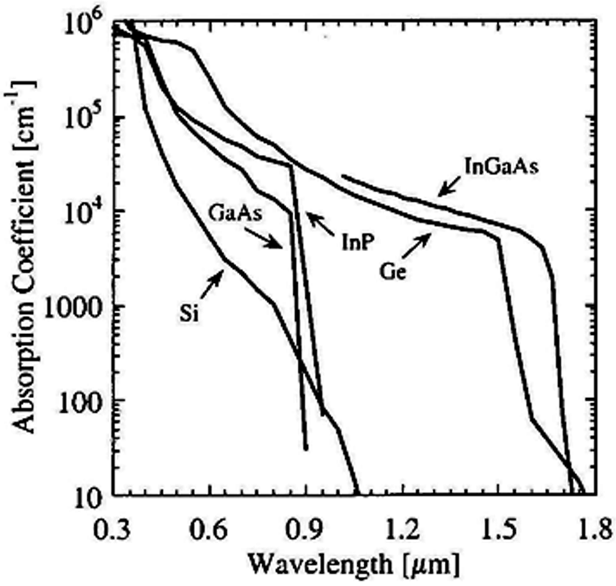

Figure 3.2. Absorption coefficient (α) versus wavelength for some materials [7].

This relation points that the light with a short wavelength is absorbed close to the surface while the long wave length light penetrates deep into silicon substrate [8]. The efficiency of photogeneration is related to the quantum efficiency ($\eta_{quantum}$) of the material. Quantum efficiency is the average number of generated and collected carrier pairs per photon. Quantum efficiency is ideally one. However, all of the carrier pairs cannot be collected, which makes the quantum efficiency value less than one. Quantum efficiency depends on the absorption coefficient, hence it is also wavelength dependent. The quantum efficiency for a photodiode can be defined as

$$\eta_{quantum} = \frac{I_{ph}q}{P_0 h\nu}, \tag{3.3}$$

where I_{ph} is the measured photogenerated current, q is the electronic charge, P_0 is the incident optical power, and hv is the energy of a single photon.

Another important merit for the photodiode is the responsivity (R_λ) of the material. It is defined as

$$R_\lambda = \frac{I_{ph}}{P_0}. \tag{3.4}$$

Responsivity is also wavelength dependent and it can also be calculated using the quantum efficiency value as;

$$R_\lambda = \frac{\eta_{quantum}\lambda}{1.24}, \tag{3.5}$$

where the optical wavelength λ is expressed in μm. Figure 3.3 shows the responsivity of a silicon photodiode as a function of the wavelength. Responsivity decreases rapidly in the short wavelength region (λ<500 nm) due to the shallow penetration depth of photons, which lead to a higher surface recombination rate. For large wavelengths (λ>850 nm), the responsivity also decreases; the photons penetrate deep into the substrate and the generated carrier pairs recombine with majority carriers. The responsivity of a silicon photodiode is highest for wavelengths ranging from 600 nm to 800 nm since the carrier pairs are generated near the depletion region of the photodiode junction.

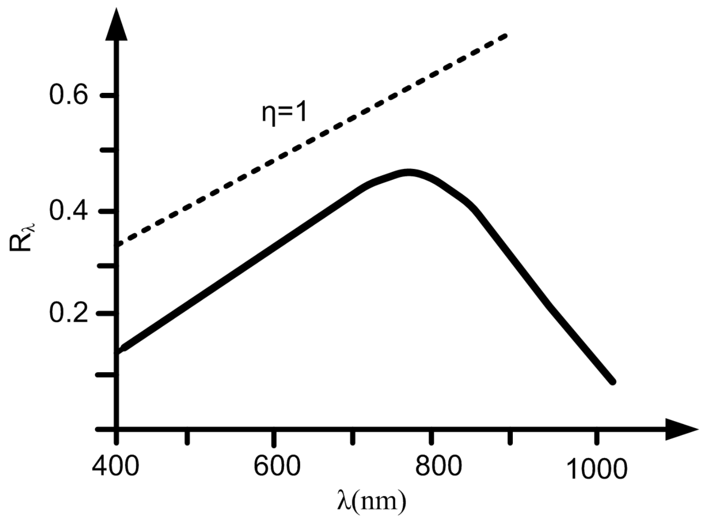

Figure 3.3. The responsivity of a typical silicon photodiode together with its ideal characteristic ($\eta_{quantum}$=1) [8].

In order to generate high current flow in the CMOS photodiodes, a laser light with a wavelength of 650 nm is determined to be suitable as the optical power source in the system. Although the main reason for this preference is that the silicon responsivity for the 650 nm is high, it is also beneficial that 650 nm lasers are low cost and highly available.

3.2.1. Photodiodes in the Triple Well Technology

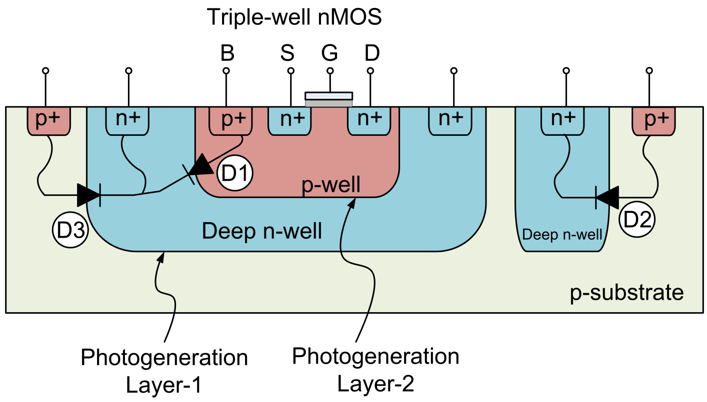

Figure 3.4. Triple-well technology cross section and possible photodiode architectures.

The cross-section of used triple well technology and the *pn* junctions which can be exploited as on-chip photodiodes are shown in Figure 3.4. There are three types of *pn* junctions that can be used as effective photo generated current sources. The first *pn* junction marked as D2 forms a photo-generation layer between the deep n-well diffusion and the p-type substrate. This type of diode is referred as n-well photodiode in this work. The second type of photodiode, marked as D3 in Figure 3.4, is between the deep n-well and the p-type substrate having a common anode port with D2. D3 is referred as a parasitic photodiode for the reasons that will be explained shortly. Finally, the third photodiode, shown as D1, is the junction between the p-well and the deep n-well which is isolated from the p-type substrate. This type of diode is referred as triple-well photodiode in this work. As n-well photodiodes have a common anode connection through p-type substrate, it is not possible to tie them in series to increase the overall voltage.

Anode of the n-well photodiode is the substrate, thus it is inherently grounded. Therefore, it is not possible to use it as a positive voltage source. However, n-well phtoodiode is more efficient than the triple-well photodiode, since it has the largest junction area and it is the deepest junction ($\sim 2\mu$m deep from the surface of the Si die.).

Triple-well photodiode (D1) and deep n-well photodiode (D3) have common cathode connection and they form a Buried Double Junction photodiode [83–87]. During the normal operation of D1, the junction between the deep n-well and p-well diffusion is illuminated, which means that the junction between the deep n-well and the substrate receives light as well since the junction is shallower then the penetration depth of the 650 nm light in the silicon. As a result whenever D1 is optically turned on, D3 turns on too, acting as a parasitic photodiode. As a solution, p-type substrate and the n+ contact diffusion of the deep n-well are shorted at the ground potential. Because of the necessity to tie cathode of D1 to ground level, it is not possible to have a series connection of triple-well photodiodes. Although it is allowed to tie n-well (D2) and triple-well (D1) photodiodes in series, this connection puts a severe restriction to the usage of triple-well nMOS transistors [88].

Three generations of integrated circuits have been designed and manufactured. In each generation, different photodiode topologies are tested in order to obtain best power conversion efficiency. Following sections present the design and characterization of the photodiodes designed in each generation respectively.

3.2.2. First Generation Photodiodes

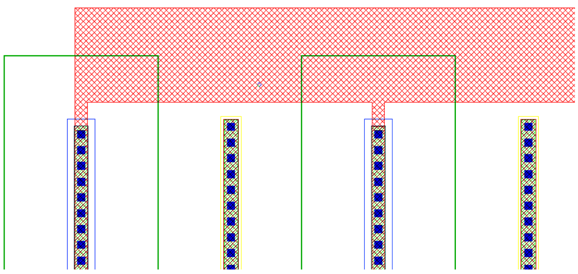

Figure 3.5. Close-up view of the first generation n-well photodiode layout, 4.5μm wide n-well fingers are used.

3.2.2.1. n-well photodiode. n-well photodiode designed in the first generation integrated circuit has an area of 300 μm×300 μm, because of the dummy metal patterns with gaps automatically placed on the photodiodes for the uniformity of the metalization process at the foundry, the effective area of the photodiode is reduced. Experiments are done on n-well photodiodes covered with metal patterns. These characteristics are shown in Figure 3.6. A short-circuit current of around 0.93 mA is achieved from an optical power of 80 mW.

However, these results do not represent the full capacity of the n-well photodiode since they are mostly covered with shielding metal patterns. In order to measure the maximum capacity of this photodiode, metal layers over the n-well photodiode were removed by in-house wet chemical etching. Figure 3.6b shows the current versus the voltage between the terminals of the n-well photodiode after the dummy metal patterns are removed. In these results, the photodiode goes into saturation at tested optical power levels greater than 30 mW. The current of the photodiode does not increase much as the optical power is increased beyond this level. A short-circuit current of 0.91 mA is achieved from an optical power of 13.4 mW indicating a responsivity of 0.068 A/W. Thus, removing the metal patterns over the n-well photodiode increases its capacity by a factor of 6 meaning that metal patterns over the photodiode reduces its area to 1/6th (122 μm×122 μm). That is why the metal covered n-well results in Figure 3.6a does not show any saturation even at measured optical power of 160 mW.

3.2.2.2. Triple-well photodiode. The triple-well photodiode on the chip is one of the most determinant elements of the system, since it allows integration of other circuitry (DC-DC converter in this case) on the same die. Even though the triple-well photodiode used to power the DC-DC converter circuit consumes an area of 300 μm×300 μm, it can be deduced from the experimental results of n-well photodiodes presented in the previous subsection that the effective area is reduced to 122 μm×122 μm due to the dummy metal patterns put on top of them at the foundry.

While determining the current through the triple-well photodiode, the cathode of

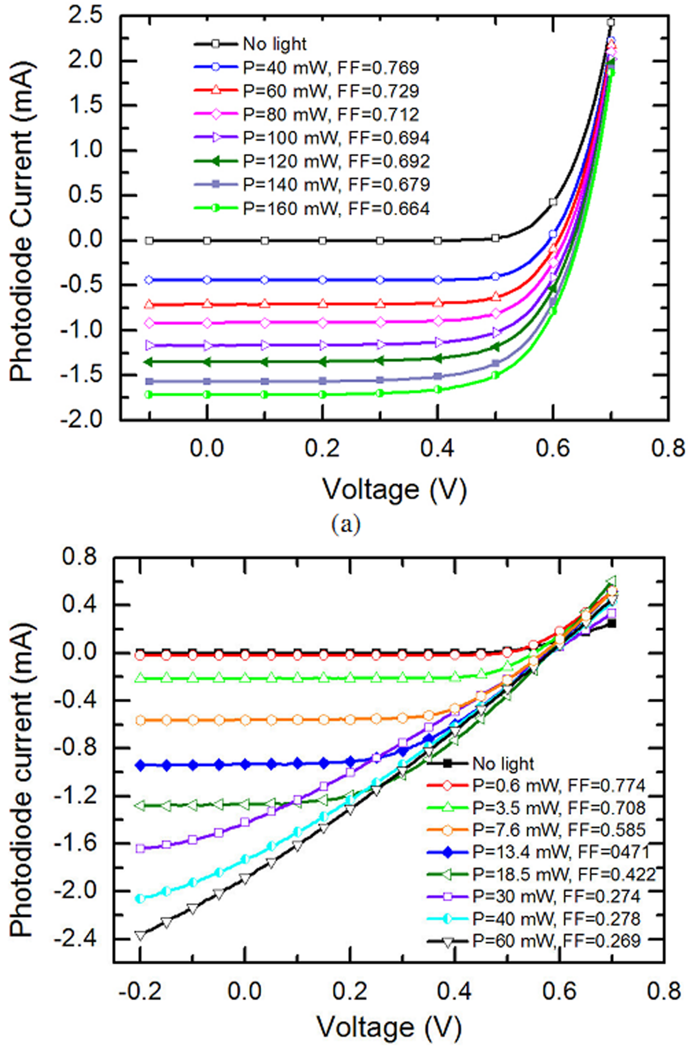

Figure 3.6. Current-Voltage characteristics of (a) metal covered (b) uncovered n-well photodiode illuminated with a laser by varying the optical power.

the photodiode, deep n-well and the p-substrate are shorted to eliminate the effects of the parasitic current due to deep n-well/substrate junction (D2) in Figure 3.4.

During the measurements, optical power of the laser is varied from 40 mW to 200 mW. Measurements results are shown in Figure 3.8, where both parasitic current (I_{PAR}) due to D3 and the useful photodiode current (I_{PD}) of D1 are plotted. Generated photodiode current increases linearly with the optical power level of the illumination. These current levels permit the DC-DC converter to function properly with an efficiency around 50%. At 200 mW of incident light power, 0.85 mA of photodiode current is measured, indicating a responsivity of 0.0043. From the results of the n-well photodiode

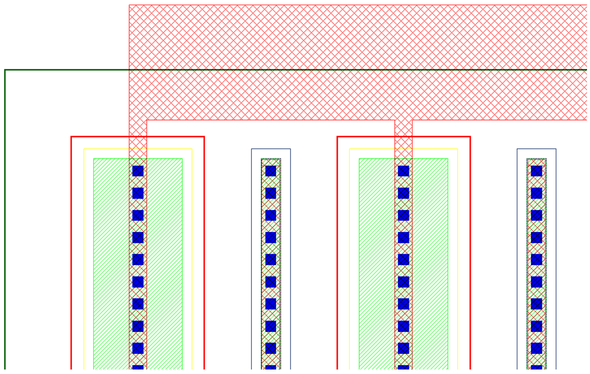

Figure 3.7. Close-up view of the first generation triple well photodiode layout, 3μm wide p-well fingers are used.

covered with metal patterns in the previous subsection, it is extrapolated that the same photo current can be generated at an optical power of around 33 mW, indicating a responsivity of 0.026 A/W. This implies that n-well photodiodes are roughly 2.5 times (at high optical power levels) to 3.8 times (at low optical power levels) more efficient than the triple-well photodiodes. The triple-well photodiode current is lower than the n-well photodiode measured at the same optical power levels, mainly due to the regions where photo-generation occurs. This is expected since the junction depth of the n-well photodiode is deeper than the one of triple-well diode. The reason for the variation of the efficiency difference between these two photodiodes is that the n-well photodiode enters into saturation regime more rapidly than the triple-well diode.

3.2.3. Second Generation Photodiodes

In the second generation IC, the size of the triple-well (D1) photodiode is increased to 600 μm$\times$600 μm to increase current output of the photodiode. The dummy metal layers are prevented by dummy-block layers added. In order to decrease the parasitic loss due to D3, a metal window on the perimeter of the D1 is designed using six metal layers available in the technology. A single junction n-well (D2) structure is designed to be used as a negative voltage supply. The size of D2 photodiode is 50 μm$\times$50 μm. The D2 is placed at a close proximity (50 μm away from D1), allowing an efficient focusing of a single light beam on both photodiodes.

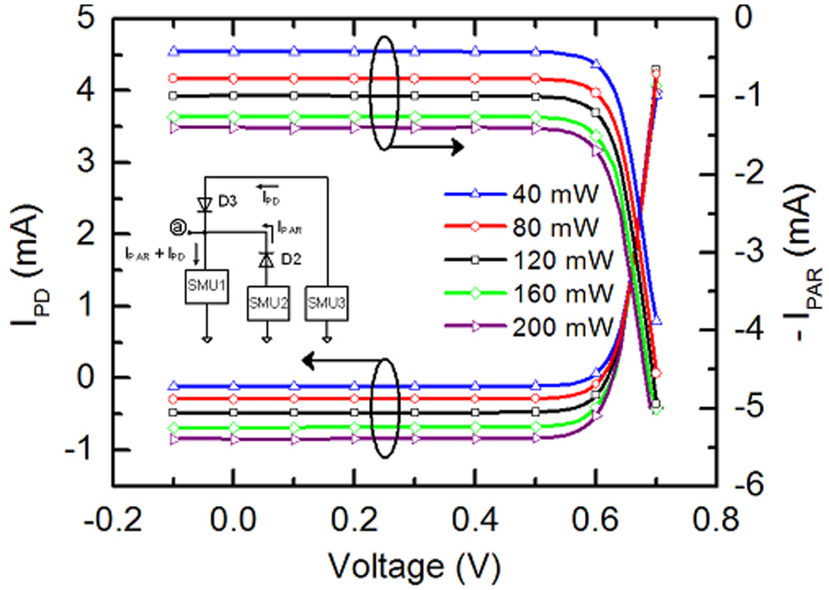

Figure 3.8. Current-voltage characteristics of the parasitic photodiode (D3) and the metal covered triple-well photodiode (D1) at different optical power levels of illumination.

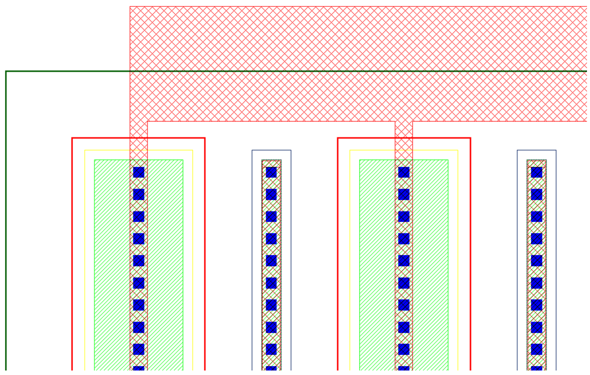

Figure 3.9. Close-up view of the second generation triple well photodiode (D1) layout.

In order to characterize the optical power supply unit and photodiodes, a test platform is formed. The specified platform is mounted on an optical breadboard to align the on-chip photodiode with the laser module. Six different optical power intensities from 10 mW to 160 mW are applied to observe the behavior of the proposed unit. Figure 3.10 shows the current-voltage characteristics of the D1 photodiode while Figure 3.11 shows the output voltage versus current of D2 photodiode. The dummy metals are removed using dummy metal block layer in the technology. Therefore, the efficiency value is increased. One n-well photodiode is kept as covered with dummy metals in order to investigate the metal coverage effects on the conversion efficiency.

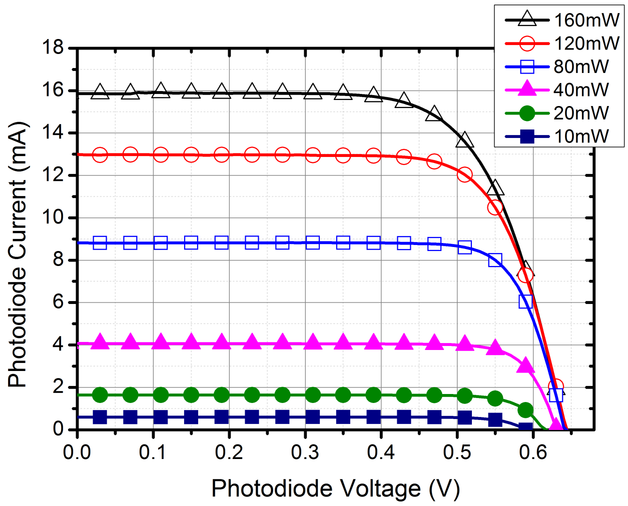

Figure 3.10. Current-voltage characteristics of uncovered triple-well, D1, photodiode.

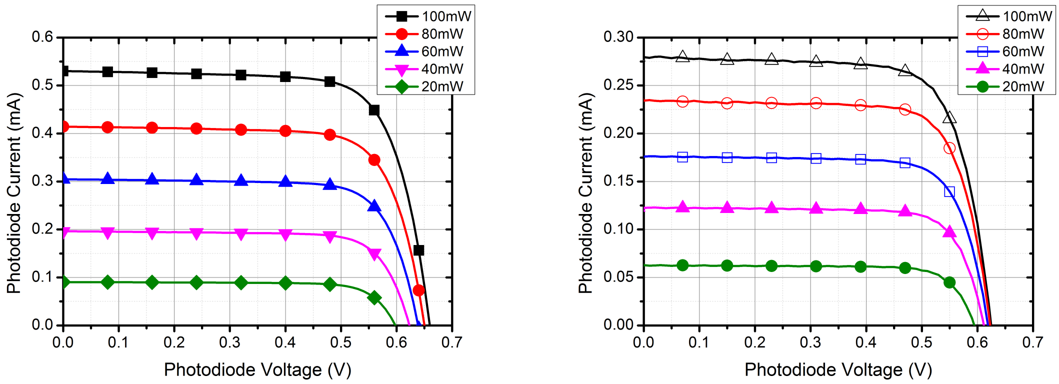

(a) (b)

Figure 3.11. Current-voltage characteristics of second generation (a) uncovered, (b) covered n-well photodiodes.

The dummy metal removal process and the four time increase in the area result high short-circuit current values for the D1 photodiodes. At 160 mW optical power, D1 generates 16 mA current while in the first generation, this value is measured as 500μA approximately.

3.2.4. Third Generation Photodiodes

The design goal in the third generation IC is increasing the coupling efficiency by implementing a dough-nut shaped triple-well (D1) photodiode shown in Figure 3.12. The size of D1 is decreased to 500 μm$\times$500 μm; however the efficiency value is increased by increased finger density in the layout as shown in Figure 3.13. Additionally, for transmission purposes, a single well triple well photodiode with a size of 140 μm$\times$140 μm is realized as the secondary photodiode.

The fiber coupling to the on-chip photodiodes is also investigated with this generation photodiodes. The coupling process can be done in various ways. The simplest approach is butt-coupling process, shown in Figure 3.25, in which the fiber core is aligned onto the photodiodes using a 3D micro-meter stage by measuring the magnitude of the induced current, and when the maximum current level is obtained the core is fixed with an epoxy adhesive. In this method, refractive index matching confines the optical signal within the epoxy-fiber system.

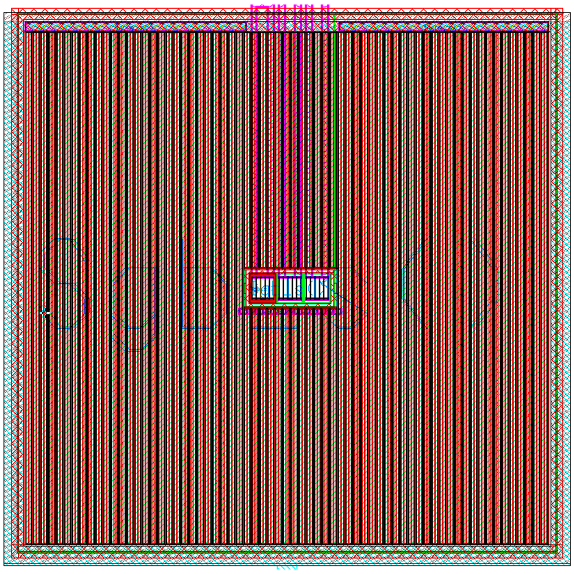

Figure 3.12. Layout of the third generation triple-well photodiode (D1).

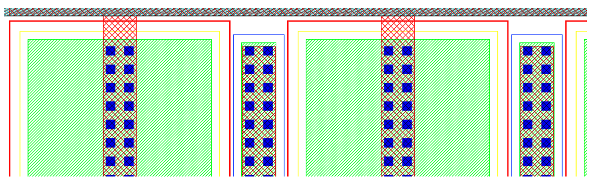

Figure 3.13. Close-up view of the third generation triple well photodiode layout.

The obtained current-voltage characteristics of large triple well (D1) and single finger triple well photodiode are shown in Figure 3.14a and Figure 3.15a respectively. In this measurements the power of the 650 nm laser is focused on to the photodiodes using the lens. On the other hand, in order to operate the power supply unit properly,

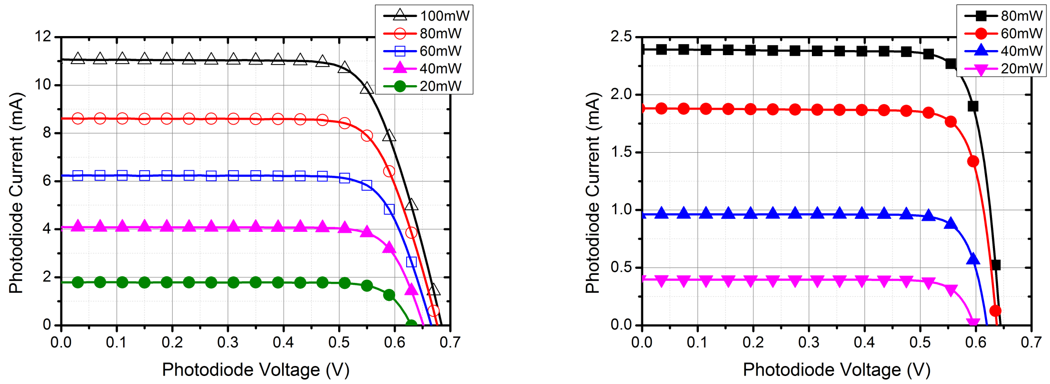

(a) (b)

Figure 3.14. Current-voltage characteristics of third generation large triple-well photodiode with (a) lens focusing, (b) butt-coupling.

the laser light has to fall on both photodiodes. A cube shaped Plexyglass holder (length of the one side of 1 cm) is manufactured and used for the butt-coupling process. A multi-mode fiber optic cable with the core diameter of 62.5 μm is placed inside this holder, and with an epoxy adhesive, both cube holder and fiber optic cable are sealed to the IC package. During this process output currents of both photodiodes are observed and the sealing is done when the optimum values are obtained. Fiber-coupled laser (Coherent CUBE 660-75 FP) with a maximum power of 80 mW is used in butt-coupling characterization. The characterization of butt-coupled photodiodes are shown in Figure 3.14b and Figure 3.15b. It is very important to note that, these two photodiodes are on the same chip and illuminated with a single fiber. However, in the lens coupling different chips are used for characterization of two photodiodes to observe the maximum available current. These situation and loss related to the fiber-optical cable result in a high efficiency loss in butt-coupled photodiodes. For D1 photodiode, there is a 71% loss in the current output in the but-coupling process. While the loss for D2 photodiode is 99.6% . It is important to note D2 photodiode is utilized for controlling the optical switch located between DC-DC current source and the receiver. It is used in photovoltaic mode, and it provides voltage to the optical switch circuit. Thus, high current loss in the D2 does not effect the operation of the system.

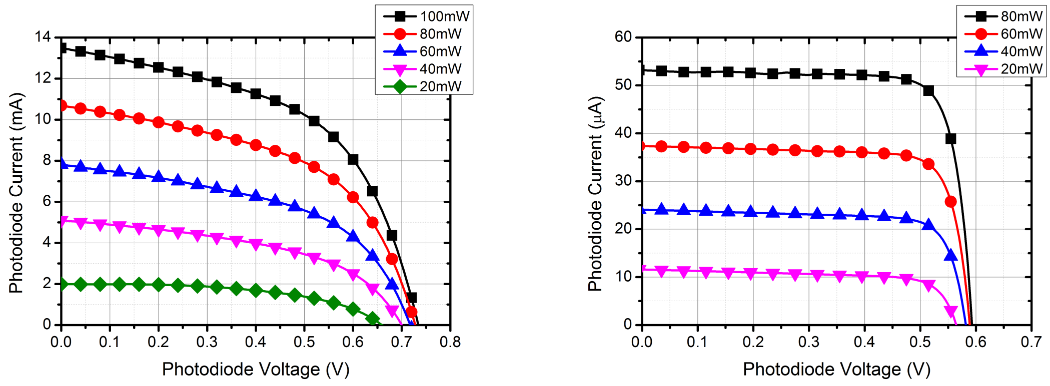

(a) (b)

Figure 3.15. Current-voltage characteristics of third generation single finger triple-well photodiode with (a) lens focusing, (b) butt-coupling.

3.2.5. Comparison of the Photodiodes

Photodiode structures are improved in each generation. In the first generation, a metalization layer severly effects the quantification of the overall performance of the photodiodes. However, measurements done with them point out that the photodiode size has to be increased to obtain higher currents. Therefore, the second generation photodiode that acts as the main power supply is determined to cover an area as four times larger than the area of the first generation photodiodes. For the third generation photodiode, the area is decreased by approximately 17%. On the other hand, the number of fingers increased by 5% to form a denser photodiode architecture. Figure 3.16 shows the maximum power output of second and third generation photodiodes at different optical power levels. Power output of both photodiodes have a linear relationship with the applied optical power level. However, the larger size of the second generation photodiode allows it to provide more power at lower optical powers. However, when the optical power level increased beyond 30 mW the power values are leveled. At higher optical power levels, the power output starts to saturate at 7 mW.

Figure 3.17 shows the efficiency comparison of two photodiodes. Efficiency values increases linearly up to 50 mw-60 mW optical power level. Higher optical power levels saturate the photodiodes. The average efficiency of photodides can be approximated as 5% .

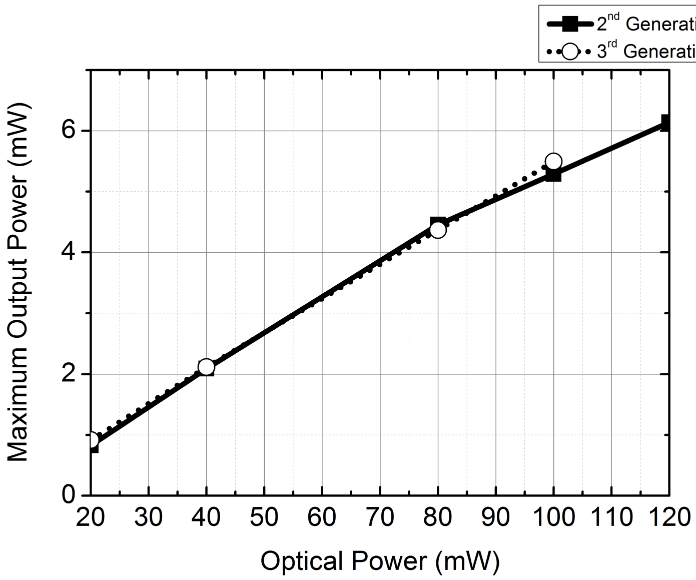

Figure 3.16. Output power comparison of second and third generation photodiodes at different power levels of illumination.

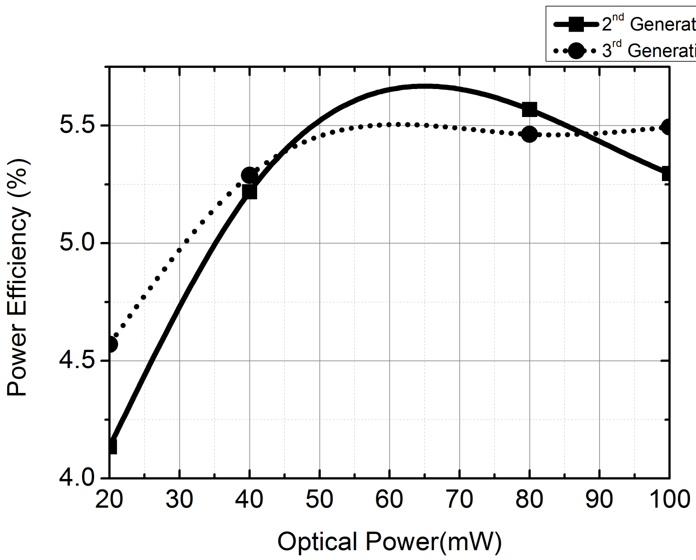

Figure 3.17. Power efficiency comparison of second and third generation photodiodes at different power levels of illumination.

The fill factor (FF) is an important parameter in evaluating the performance of photodetectors. It is defined as the ratio of the maximum obtainable power to the product of the open circuit voltage and short circuit current. Photodiodes with a high fill factor have a low equivalent series resistance and a high equivalent shunt resistance, thus less amount of the current is dissipated internally. Figure 3.18 shows the fill-factor comparison of second and third generation photodiodes at different optical

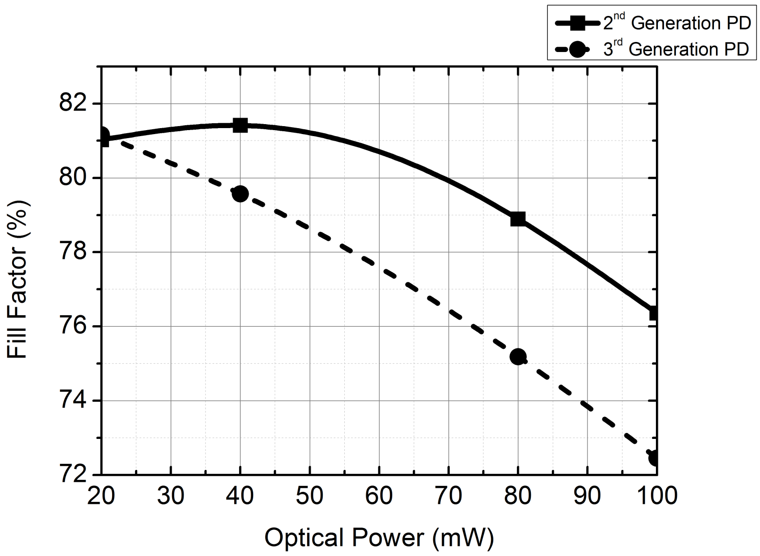

Figure 3.18. Fill-factor (FF) comparison of second and third generation photodiodes at different power levels of illumination.

power levels. Second generation photodiode has better fill-factor performance that points out its eqivalent series resistance is lower and shunt resistance is higher than the third generation photodiode. The higher fill-factor of second generation photodiode also implies that there is a lower parasitic power dissipation in the second generation photodide. This result can be attributed to the larger area, hence two photodiodes provide approximately same power levels. As a result, the power density of the second generation photodiode is lower, which can explain the fill-factor increase in the second generation photodiode. It is also important to note that fill-factor values decrease with the increased optical power level due to exponential characteristic of the photodiode open circuit voltage.

3.3. DC-DC Converter

Designed DC-DC converter is shown in Figure 3.19 [81]. The converter has two main parts; a two stage voltage doubler [89] and a clock generator circuit which is basically a ring oscillator connected to two buffer circuits. Buffers are designed to drive the large stage capacitors of 40 pF in the voltage doubler circuitry. The photodiode voltage is denoted as V_{PD}; and it is the input voltage of the DC-DC converter. Additionally, it serves as the power supply voltage for the clock generator circuitry.

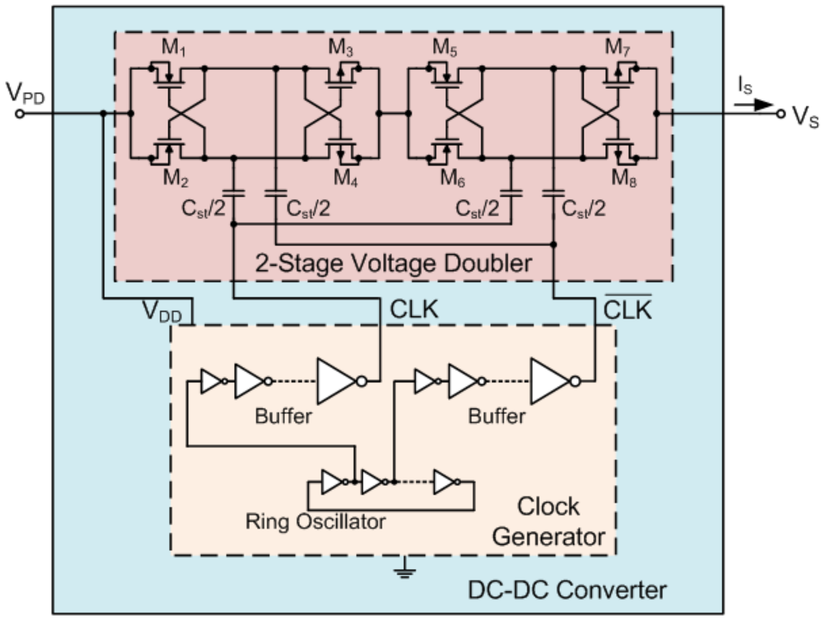

Figure 3.19. Schematic of the DC-DC converter.

The supply voltage provided by optical power supply unit decreases while the receiver draws current from it. The maximum supply voltage $V_{DD,max}$ is directly related to the DC-DC converter output V_S while the transmission gate switch is open. V_{DD} is ideally equal to $(N+1)V_{PD}$. On the other hand, since there is a leakage current at the output in addition to the body effect, the ideal voltage cannot be attained experimentally. When there is a current drawn from the output, V_S can be calculated by the following formula [90];

$$V_S \approx (N+1)V_{PD} - R_{O,dcdc}I_S, \tag{3.6}$$

where N=2 is the number of stages, I_S is the output current, and $R_{O,dcdc}$ is the output resistance of DC-DC converter which can be calculated as $N/f_{CLK}C_{st}$ where N=2 is the number of stages, f_{CLK}=50 MHz is the ring oscillator frequency, C_{st}=40 pF is the stage capacitor. As a result, $R_{O,dcdc}$ of the designed DC-DC converter is calculated as 1 kΩ.

The theoretical power efficiency of the DC-DC converter can be calculated as [90, 91]

$$\eta = \frac{P_{out}}{P_{res} + P_{out} + P_{dyn}} = \frac{V_S I_S}{V_S I_S + R_{O,dcdc} I_S^2 + k_{sw} N f_{CLK} C_{par} V_{PD}^2}, \tag{3.7}$$

where C_{par} is the sum of parasitic capacitances in one stage, and k_{sw} is a coefficient which is simplified as the ratio between the voltage swing across any parasitic capacitance and the supply voltage, V_{PD}. The efficiency depends on the output current, thus it is different for different load currents.

Maximum efficiency of the DC-DC converter can be found by finding the maxima of the Equation 3.7 while assuming I_S as the variable. The first derivation of this function is found to be;

$$\eta(I_S)' = \frac{V_S (k_{sw} N f_{CLK} C_{par} V_{PD}^2 - R_{O,dcdc} I_S^2)}{[I_S (V_S + R_{O,dcdc} I_S) + k_{sw} N f_{CLK} C_{par} V_{PD}^2]^2}, \tag{3.8}$$

where k_{sw} and C_{par} values are technology dependent, and they are not readily available. Nevertheless, with a pessimistic approach, if it is assumed that $C_{par} k_{sw}$ is 10% of C_{st} (i.e. 4 pF) and V_{PD} is 0.5 V, the maxima of the efficiency function is found to be approximately at 300 μA.

3.4. Characterization of the Optical Power Supply Unit

Characterization of the DC-DC converter unit is repeated for three generation ICs, since photodiode structures differ in each generation. Three coupling processes are used; (i) lens coupling shown in Figure 3.23, (ii) micro-platform coupling shown in Figure 3.21, and (iii) butt-coupling shown in Figure 3.25.

In the lens-coupling, a convex lens (f=50 mm) is used to focus the light onto the photodiodes. This method does not involve any fiber optic cables, hence the loss is minimum. Therefore, it is the reference method that is used to determine the maximum attainable power from the photodiodes. Micro-platform is used to test the integrability of the system into the catheter by reflecting light with a silicon micro-mirror manufactured in house using KOH etching. Butt-coupling is direct coupling of fiber-optical cable to the photodiode structures using micro-manipulators. The fiber is sealed in a cube shaped plexy-glass holder (one side is1 cm) with an epoxy adhesive to increase the rigidity of the integrated system.

3.4.1. Characterization of the First Generation Power Supply Unit

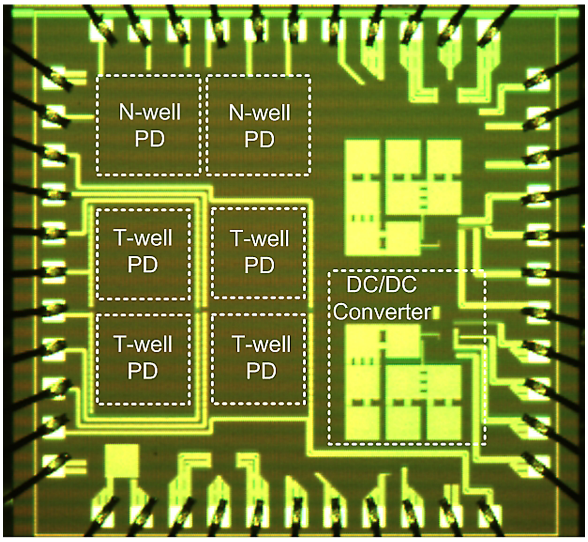

Figure 3.20. Micrograph of the first generation IC.

The first generation IC shown in Figure 3.20 is characterized with lens-coupling and with a micro mirror platform. The lens coupling results are given in Figure 3.22a.

Registration of optical power to the CMOS integrated photodiodes is performed by using a micromachined silicon mirror which allows efficient optical coupling of the light coming out of a multi-mode fiber optic cable. Design of the fiber platform is performed by running geometrical optics simulation. The light sensitive area, where the CMOS photodiode of the chip is going to be aligned, receives the light reflected from the 54.7 degree inclined mirror. Angle of the mirror is defined by the physical realization process (Potassium Hydroxide-KOH etching) [54, 92]. Important design parameters of the fiber-platform are width (w) and depth (h) of the V-shaped groove, width of the mirror opening (y), separation between the fiber end and the mirror (d) and distance between the center of the fiber core and the bottom of the V-groove. A mask design is performed by first assuming intimate contact with the CMOS chip and the fiber platform and by considering square-shaped triple-well photodiode on the CMOS chip with an area of 300 μm $\times$ 300 μm, diameter of the multimode fiber as 2r= 62.5 μm, numerical aperture as 0.275. Since KOH etch is used for defining the three dimensional structure in silicon, additional structures for etch compensation are included.

Silicon mirror platforms are fabricated in house using basic bulk micromachining processes. Coating the silicon mirrors with a reflective material such as aluminum is necessary in order to increase their reflection performances. The reflectivity of the silicon mirrors are measured by inserting a fiber optic cable inside the silicon V-grooves and measuring the incident laser power inside the fiber and the reflected laser power from the silicon mirror using the optical power meter. A multimode fiber optic cable with a diameter of 125 μm and a core diameter of 62.5 μm is used in the experiments.

Finally, the micromachined silicon optical platform and the IC die are integrated together. The fiber optic cable is placed on the V-groove of the silicon platform. This platform is then aligned to the IC die under a probe station. Probes are used as electrical feeds from the IC die. By using micromanipulators' linear and rotational motions, the reflected laser beam from the silicon mirror is aligned to the triple-well photodiode while monitoring the short circuit current and the open circuit voltage of the photodiode using the semiconductor parameter analyzer. After successful alignment, positions of the fiber optic cable, silicon platform and the integrated circuit die are fixed by applying epoxy. The pictures of the packaged system are shown in Figure 3.21. The packaged system is characterized by monitoring the output current and voltage of the DC-DC converter circuit while a laser beam is applied to the triple-well photodiode on the same die at different power levels through fiber optic cable

Micro-fabricated silicon mirror platform for the fiber optic cable is separately characterized, before it is integrated to the CMOS circuit die. After the optical fiber is placed into the V-groove of the Si platform, reflectivity measurements of the mirrors are done. As the optical power inside the fiber is changed and measured, the reflected power from the silicon mirror surface is measured by the optical power meter. The measurements are done by using two samples to see the variance caused by the processes.

The uncoated micro-machined Si mirrors had a reflectivity of 33% for the laser input at a wavelength of 650 nm. Since low reflectivity of the mirror surface is an important constraint for integration of the micro-machined Si platform and the IC die, platforms are coated with 25 nm thick aluminum film using a high vacuum thermal evaporator, which has more reflectivity than Si. Addition of this coating increased the reflectivity of the mirror to about 80%.

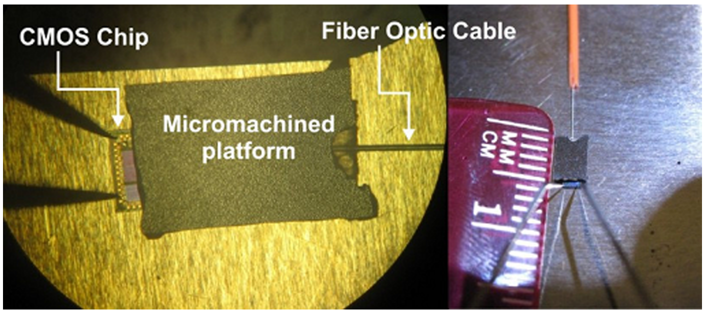

Figure 3.21. The first generation IC coupled to a fiber optical cable using a micro-platform.

The measurement results from the packaged system, containing a fiber optic cable, silicon mirror platform and IC die shown in Figure 3.22b. As the optical power through the fiber optic cable is changed and measured, the output voltage and the current of the DC-DC converter circuit is measured. About 120 mW of optical power is enough to turn on the DC-DC converter circuit and generate 1.2 V. However, this same voltage levels were available from a 40 mW optical power in the experiments done with lens coupling. This means that 67% of the optical power is lost during the packaging of the fiber optic cable, silicon mirror and the IC die. From the characterization results, we know that 20% of the optical power is lost in the Al coated silicon mirror. The remaining percentage of the loss, however, is due to the scattering of the light from the mirror surface and the misalignment of the mirror to the photodiode surface. Since, the Si mirror does not focus the beam onto the photodiode like the way convex lens does, the illuminated area becomes greater than the area of the triple-well photodiode area. As a result collected optical power is reduced. However, still, by inserting optical power levels of 120 mW and above, the DC-DC converter can be run to generate 1.2 V.

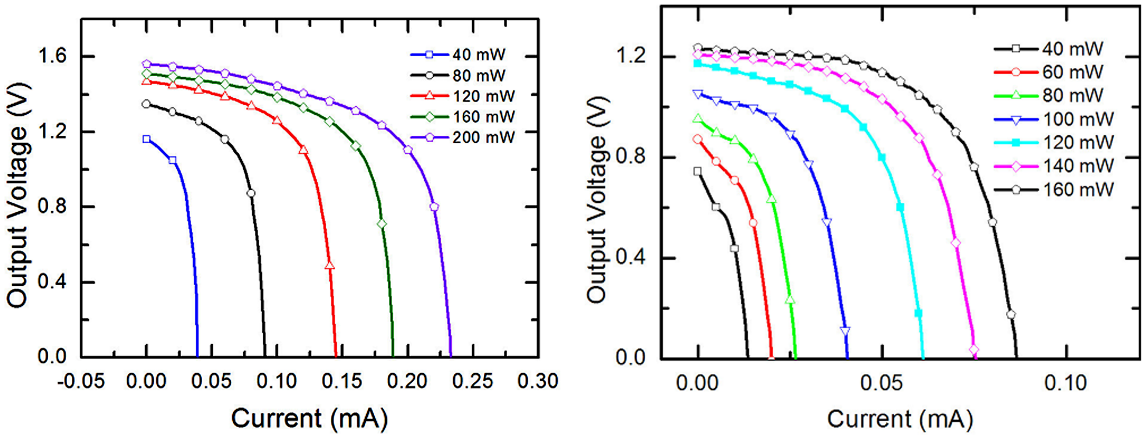

(a) (b)

Figure 3.22. Characterization of the first generation optical power supply unit (a) with lens coupling and (b) with the silicon micro-mirror platform at different optical power levels of illumination.

It is important to note that, this system would be operational even with mirror loses and alignment errors with optical power levels of 20 mW if it had not been for the metal patterns over the triple-well diodes.

3.4.2. Characterization of the Second Generation Power Supply Unit

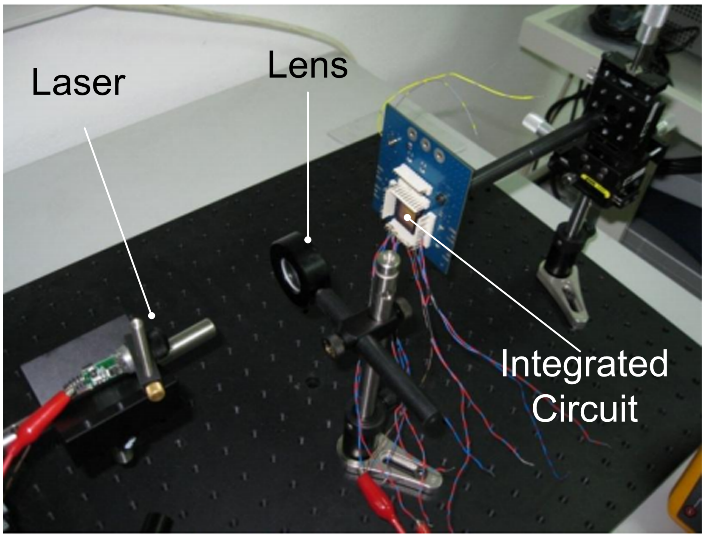

Figure 3.23. Second generation IC is coupled to a laser source using a convex lens (f=50 mm).

In the second generation, the lens coupling utilized. In order to characterize the optical power supply unit, a test platform consisting of the test chip and an off-chip capacitor C_S of 10 μF is fabricated. $D1$ photodiode is connected to the input of the DC-DC converter to provide the input voltage V_{PD}. The specified platform is mounted on an optical breadboard to align the on-chip photodiode with the laser module. Six different optical power intensities from 10 mW to 160 mW are applied to observe the behavior of the proposed unit. Figure 3.24 shows the output voltage versus current loading for the overall power supply unit at different optical power levels of illumination. The presented integrated system is able to deliver 450 μA of bias current with more than 1.2 V of supply voltage to an electronic system continuously, when an external optical power of 120 mW is given as the input. It is important to note that at high optical power levels the proposed unit saturates and the overall power conversion efficiency starts to decrease.

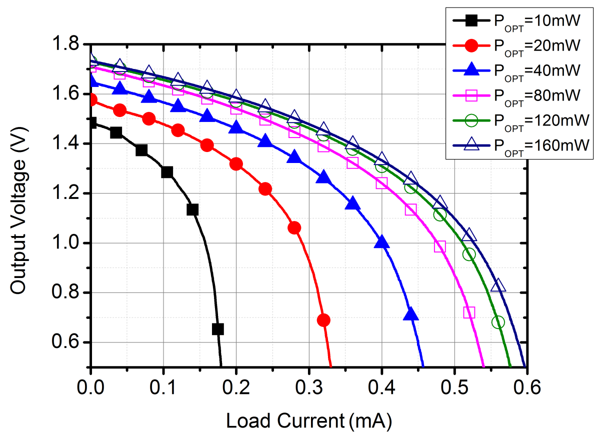

Figure 3.24. Characterization of the second generation unit at different optical power levels of illumination.

The measurement results show that maximum power conversion efficiency of the unit is 53%; while it can deliver 540 μW electrical power which is 9 times greater than the first generation configuration under the same condition.

3.4.3. Characterization of the Third Generation Power Supply Unit

In the third generation, lens-coupling and butt-coupling processes are utilized. A test PCB with the off-chip storage capacitor C_S of 22 μF is fabricated. This platform is used for both coupling tests. In the lens coupling, five different optical power intensities

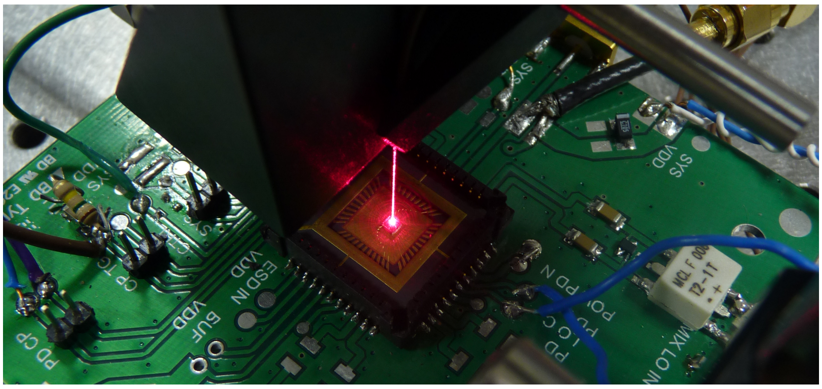

Figure 3.25. A fiber optic cable is butt-coupled to an IC using micro manipulators.

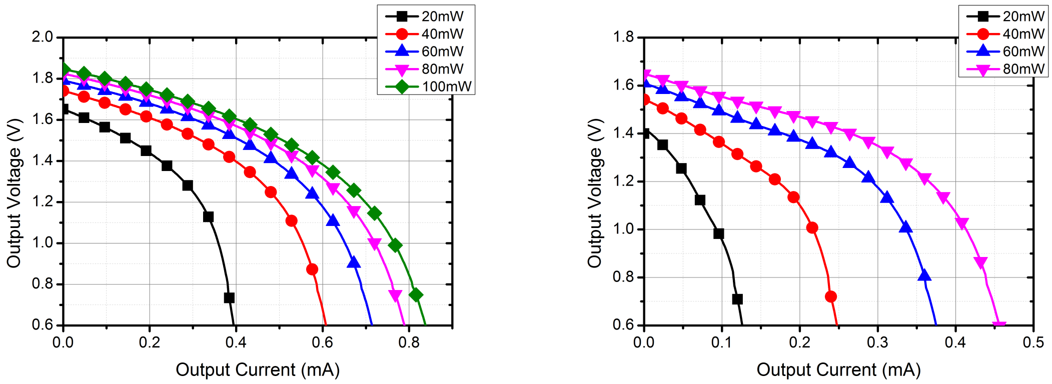

(a) (b)

Figure 3.26. Characterization of the second generation optical power supply unit (a) with lens coupling and (b) with the silicon micro-mirror platform at different optical power levels of illumination.

from 20 mW to 100 mW are applied. Results are shown in Figure 3.26a. The results show that the overall unit can deliver 656 μA and 1.2 V at 80 mW optical power. This value is approximately 1.6 times greater than the second generation results at the same optical power level. The increase in the number of fingers results a higher pn junction area; and therefore, a higher efficiency for the same optical power levels.

The unit is also tested with the butt coupling method. A bore of 500 μm in diameter is created in a cube shaped plexy-glass holder using a laser cutter. The cube holder is used to stabilize a pig-tailed fiber-optical cable with a core size of 62.5 μm. An FC connector is attached to the one end of the fiber-optical cable which is then placed in the bore. Since the aim in the butt-coupling process is the efficient coupling of the fiber to the two photodiodes placed on the third generation IC, two photodiode currents are observed during the coupling process. When the maximum values are attained the fiber is sealed to the plexy-glass holder cube and to the package by administering epoxy adhesive to the bore and perimeter of the holder. A fiber coupled laser (Coherent CUBE 660-75 FP) with maximum output optical power level of 80 mW is used in the experiments. The results are given in Figure 3.26b. The butt-coupled unit can deliver 365 μA with 1.2 V at 80 mW optical power level. The efficiency during coupling process is calculated as 56%.

3.5. The Inherent Feedback Mechanism

The combination of the on-chip photodiode together with the DC-DC converter circuit forms an inherent feedback in the presented system. The feedback mechanism can be explained as follows. The photovoltaic voltage of the photodiode, V_{PD} serves as the supply voltage for the clock generator circuit, and it determines the clock frequency f_{CLK} for the voltage doubler circuit. The input current of the converter circuit, I_{IN}, is directly related with the clock frequency, f_{CLK} and therefore V_{PD}. Thus, all parameters of the proposed unit is in some way related to each other; and the final operation point of the power supply unit must be found by solving the relation between V_{PD}, f_{CLK}, I_{IN} and the photodiode current I_{PD}. Since the input current of the converter I_{IN} is supplied from the photodiode, $I_{IN} = -I_{PD}$ is the solution of the relation. Any increase in load current would create a decrease in photodiode voltage, thereby decreasing f_{CLK}, hence decreasing current demanded from the photodiode, thus pushing the system into the maximum efficiency point.

In order to illustrate this feedback mechanism, three different relations; the clock frequency versus the supply voltage of the clock generator circuit, input current versus input voltage of the DC-DC converter circuit for an output current loading of 0.2 mA and current-voltage characteristics of the second generation on-chip photodiode (D1) at 15 mW of incident optical power are shown in Figure 3.27. I_{IN} vs V_{PD} and I_{PD} vs V_{PD} curves are shown on the same graph, while f_{CLK} vs V_{PD} curve is shown separately on a second graph for clarity. On the graphs, it can be shown step by step how the system

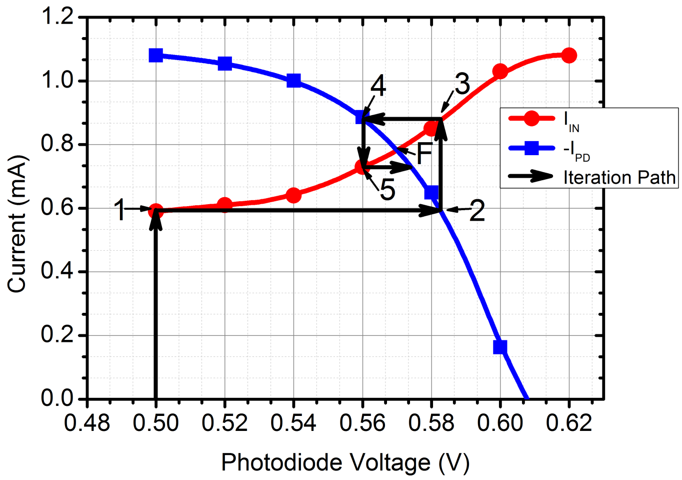

(a)

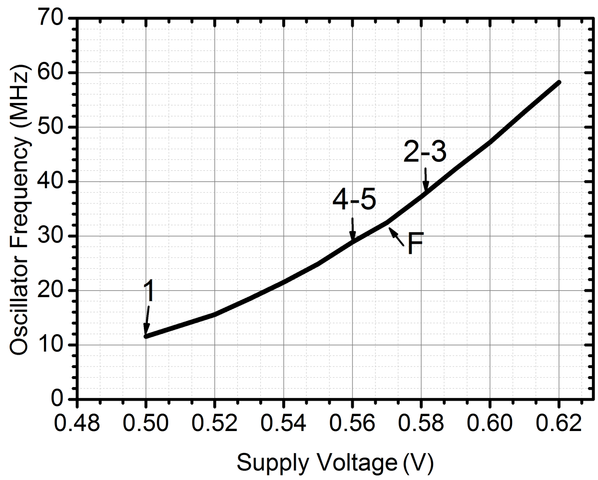

(b)

Figure 3.27. An example feedback iteration on the current-voltage curves (a) and the corresponding frequency values on the frequency-supply voltage curve (b).

converges to the final $I_{IN} = -I_{PD}$ operation point by the feedback. The iteration path on the graph shows a possible convergence path with an initial photodiode voltage, V_{PD}, of 0.5 V. The iteration starts at "point 1" and ends at the "point F". In summary, one point on the I_{IN} curve corresponds to a V_{PD}value on the I_{PD} curve and this V_{PD} value then again corresponds to an I_{IN} value. Even if the initial value is changed, the final current-voltage operation point is always found to be at the intersection of I_{IN} and I_{PD} curves. The final clock frequency value is obtained from f_{CLK} vs V_{PD} curve using the final voltage value. On the given example, the final I_{IN} and I_{PD} current values are found to be 0.77 mA (point F) where the photodiode voltage V_{PD} is equal to 0.57 V (point F) and the corresponding clock frequency f_{CLK} is 32 MHz (point F). This iteration procedure can also be applied to the other possible conditions where the load current and the incident power are different than our example. As a result, due to the inherent feedback mechanism, the proposed unit adapts itself for different loading conditions and regulates its output against the load changes moving towards the maximum efficiency point. Hence the proposed unit has some load regulation even if there is no specific load regulation circuitry used in the design. The proposed unit is also robust against the process variations due to the inherent feedback. The line regulation is not considered, since the laser provides a constant power to the system.

4. SECOND GENERATION ARCHITECTURE

The first generation integrated circuit is designed mostly for testing the optical power supply unit, hence no receiver architectures are added. In the second generation, the direct conversion receiver described in the Section 2.3.4 is implemented. The overall second generation system is composed of an integrated circuit and peripheral off-chip components in the transceiver configuration. The integrated circuit contains on-chip photodiodes, a DC-DC converter, and a receiver that consists of a fully differential low-noise amplifier, a fully differential gain stage, a single ended differential input Gilbert-cell mixer, an RC low-pass filter, and a laser driver. The receiver is a very simplistic version of the low-intermediate frequency (IF) receiver in which the acquired signal is downconverted by mixing it with an applied local oscillator (LO) signal which can be gathered optically or electrically from outside. The downconverted signal is filtered through a simple RC network and transmitted via a fiber coupled infrared (IR) laser diode ($\lambda = 1310\,\text{nm}$).

Supplying power to the receiver is realized optically in two different configurations

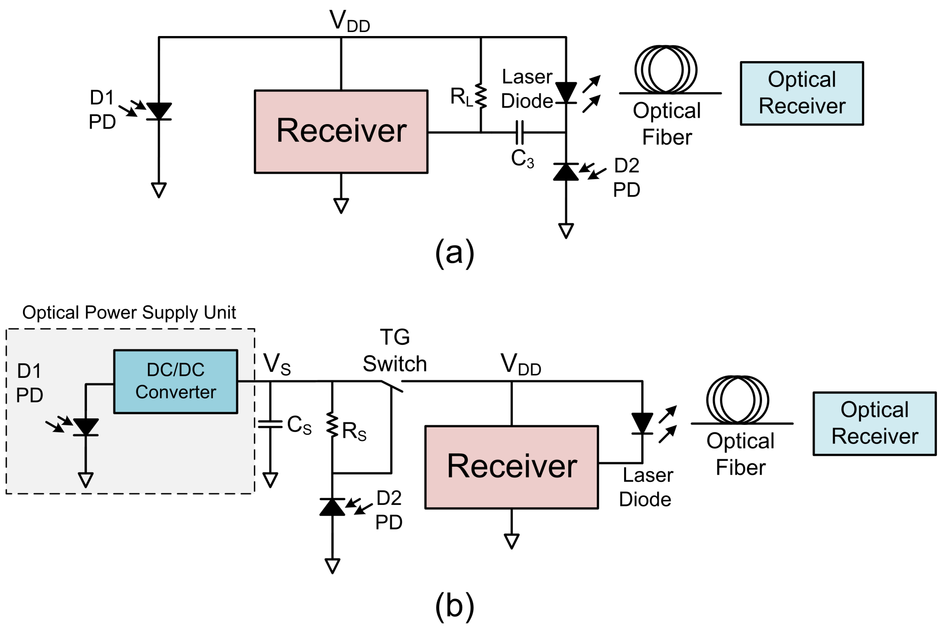

Figure 4.1. Proposed system in (a) ultra low power continuous and (b) integrated mode configurations.

as defined in Section 2.1 and Section 2.2. The two configurations, namely continuous and intermittent mode configurations, are shown in Figure 4.1a and Figure 4.1b respectively.

In the continuous mode configuration, the receiver is powered from an on-chip photodiode ($D1$) which converts the supplied optical power from a laser source ($\lambda = 650\,\mathrm{nm}$) to the electrical power. The generated voltage on the photodiode depends on the incident light power and it is in the range of 0.5 V-0.65 V. On the other hand, the output IR laser diode has a turn on voltage of 0.85 V approximately, and hence, it cannot be biased in the aforementioned range. Another on-chip photodiode ($D2$) is used to generate the necessary voltage drop on the laser diode. The anode of $D2$ is connected to the common node; and its cathode is connected to the cathode of output laser diode. When the 650 nm laser source is applied both onto $D2$ and $D1$, a negative voltage is induced at the cathode of $D2$, as a result the output laser diode turns on. The system operates continuously at very low voltages with performance trade-offs of noise and gain in the continuous mode configuration.

The second configuration, the intermittent configuration is based on boosting photo-generated voltage of $D1$ via a DC-DC converter. The photodiode and DC-DC converter combination forms the optical power supply unit which not only serves as the supply for the laser diode; it also acts as the main power supply of the whole system. However, due to low power conversion efficiency of the optical power supply unit, the system cannot be operated continuously. This problem is solved by connecting a transmission gate switch and a storage capacitor (C_S) to the DC-DC converter output (V_S) and forming a power supply unit in which the storage capacitor acts as a battery which is charged and discharged intermittently via the switch. The switch is controlled by $D2$ that is connected to V_S via a pull-up resistor (R_S). The incident light induces a negative voltage on $D2$ and thus opens the switch and allows charging of C_S. When there is no incident light on $D2$, it does not conduct; hence the switch closes and the stored charge is transferred to the receiver. This operation principle serves for obtaining higher current that is in the milliampere range. In the intermittent configuration, the laser diode is connected directly to the laser driver, since the voltage drop on the laser is sufficient for turning the laser diode on.

External receiver part of the system is shared by both configurations; it is basically an IR optical receiver cascaded by an amplifier. This signal can be transmitted to signal processing equipments for further processing, however in this work, the output signal is acquired by a spectrum analyzer for experimental reasons.

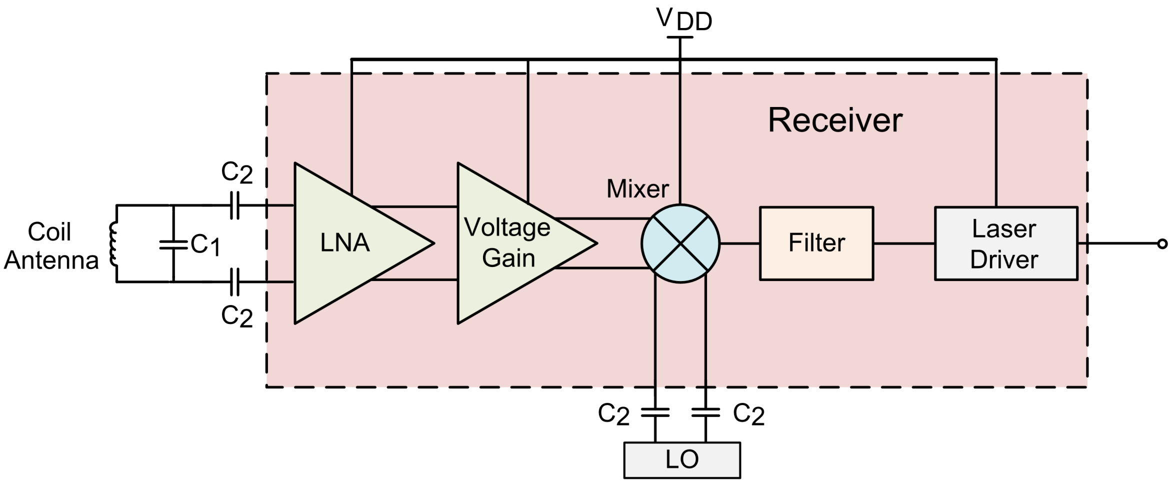

Figure 4.2. The block diagram of the second generation direct conversion receiver.

4.1. Receiver Architecture

4.1.1. Fully Differential Low Noise Amplifier

4.1.1.1. Definition of the Noise Figure. The noise in an RF system can be characterized by the noise figure (NF) value which is a measure of the degradation in the signal-to-noise (SNR) ratio. For a noiseless system, the input and output signal-to-noise ratios are equal. If the system is noisy then the output noise power increases greater than the signal power, thereby an SNR reduction is observed. Noise figure value represents the amount of reduction in the SNR. The noise figure value is defined as [59]

$$NF = \frac{\mathrm{SNR_i}}{\mathrm{SNR_o}} = \frac{S_i/N_i}{S_o/N_o}, \tag{4.1}$$

where S_i is input signal power, N_i is input noise power, S_o is the output signal, and N_o is the output noise power. Practically, the noise figure is always greater than one

($NF > 1$) since all electronic components contain a some form of noise. The noise figure value is usually expressed in dB as $10\log_{10}(NF)$.

A typical receiver system is formed by a number of cascaded stages. Noise contributions of the cascaded stage to the overall noise performance can be calculated with noise figure and gain values of each stages. If a receiver contains n stages, the noise figure of the overall system can be calculated as [59]

$$NF = NF_1 + \frac{NF_2 - 1}{G_1} = \frac{NF_3 - 1}{G_1 G_2} + ... + \frac{NF_n}{\prod_{m=1}^{n} G_m}, \tag{4.2}$$

where NF_m is the noise figure of the mth stage and G_m is the gain of the mth stage.

The Equation 4.2 clearly shows that the noise of overall system is dominated by the first stages. Hence, designing a low noise high gain first stage carries a high importance in the RF receiver systems [59, 61].

4.1.1.2. Design of the Fully Differential Low Noise Amplifier. The first block of the receiver is a two-stage amplifier formed by an LNA and an additional voltage amplifier. LNA is designed using noise matching via passive amplification method [93] instead of currently prevailing method of power matching. The passive amplification method relies on the principle of amplifying the signal and the noise in the antenna. Hence, compared to the input referred noise of the LNA, the input noise dominates resulting in a very low noise figure. A solenoid micro-coil type antenna is used in the system, and thus it can be assumed as an inductor in series with a parasitic resistance. Therefore, amplifying the induced signal is possible using a resonant capacitance for a target frequency. It is evident that the LC tank circuit of antenna and the resonant capacitor must be connected to a very high impedance node. Since the LC tank is connected to the gates of the MOS transistors in the LNA through a 100 nF DC blocking capacitors (C_2), the desired high input impedance node is inherently present in the design. Used method also serves for the purpose of using the receiver for wide range of applications, since setting the frequency of operation is simplified into finding a resonant capacitance value.

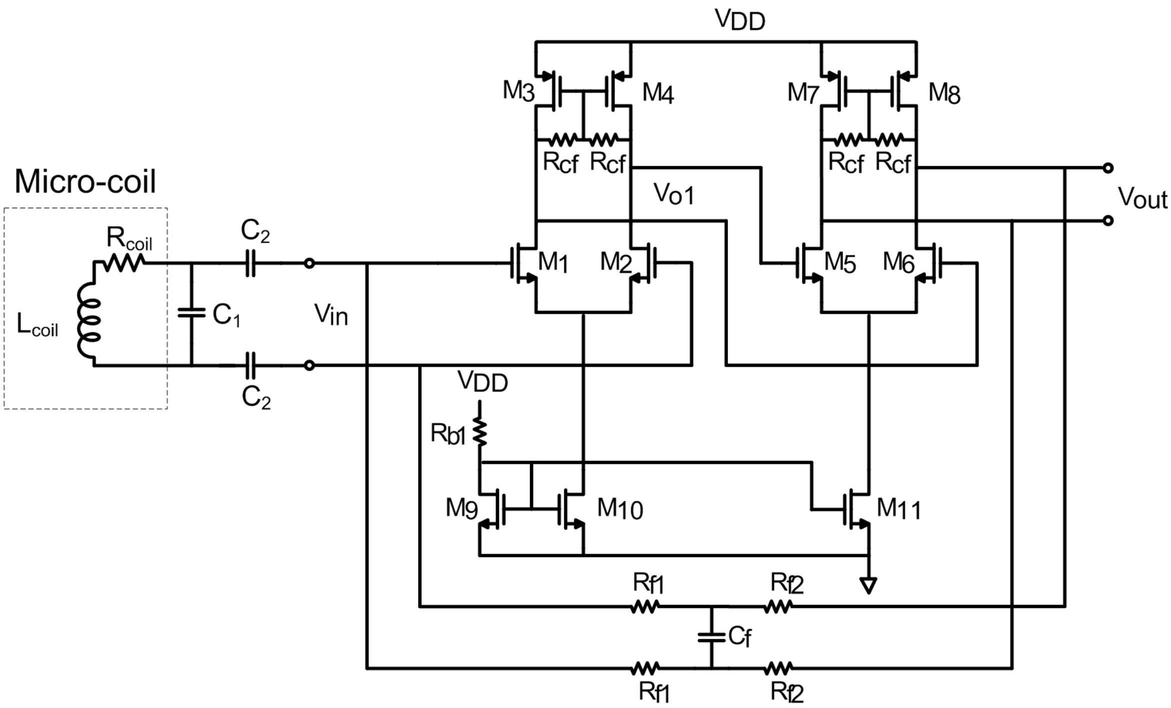

Figure 4.3. Schematic of the implemented fully differential LNA.

Figure 4.3 shows the schematic of the designed fully differential LNA. The inductance of the input micro-coil antenna is measured as 282 nH while the parasitic series resistance is 5 Ω. 22 pF capacitor (C_1) is connected to the micro-coil to form the LC tank resonating at 63.9 MHz, which is chosen for the purposes to be discussed in the experimental results section. The local common-mode feedback topology formed by R_{cf} resistors of 10 kΩ is utilized to suppress the common mode signals. For achieving a high voltage gain, a second stage with the same topology is cascaded to the LNA. The two stage amplifier has an internal feedback network formed by $R_{f1} = 66\,\mathrm{k}\Omega$, $R_{f2} = 600\,\mathrm{k}\Omega$ and $C_f = 10\,\mathrm{pF}$. The feedback network provides bias to the input differential pair; additionally, it also provides the stability.

The gain of the LNA can be calculated as

$$A_v = \frac{v_{o1}}{v_{in}} \simeq -g_{m1}(R_{cf}//r_{o1}//r_{o3}), \tag{4.3}$$

where g_{m1} is the transconductance of the M_1 transistor, r_{o1} and r_{o3} are the output resistances of transistors M_1 and M_3. The noise figure of the LNA can be calculated [81];

$$NF = 10\log_{10}\left[1 + \frac{2}{\alpha_Q^2 R_{\text{coil}}}\left(\frac{1}{g_{m1}^2 R_{cf}} + \frac{\gamma_M}{g_{m1}} + \frac{\gamma_M g_{m3}}{g_{m1}^2}\right)\right], \tag{4.4}$$

where where α_Q is the voltage gain of the passive network, R_{coil} is the parasitic resistance of the micro-coil, g_{m3} is the transconductance of the M_3 transistor, and γ_M is a parameter which is equal to 2/3 for long channel devices. In deep sub-micron devices, γ_M exceeds the value of 2/3 and is about 50% larger for 0.18 μm CMOS techology [94]. The LNA is designed to consume a current of 1 mA. It is important to note that transconductance of the M_1 (g_{m1}) should be high to obtain a low noise and high gain amplifier. The voltage gain of the designed LNA is calculated with g_{m1}=6.3 mS and $r_{o1}//r_{o3} = 3.5$ kΩ as 24 dB. The voltage gain of the second stage is calculated as 16 dB making a total voltage gain of 40 dB.

Noise performance of the fabricated LNA is measured using HP 8970B noise figure (NF) analyzer. Obtained NF values are used to extract the input referred noise voltage density of the LNA, v_{an}, using the following equation;

$$NF = 10\log_{10}\left(1 + \frac{\overline{v_{an}^2}}{\overline{v_n^2}}\right), \tag{4.5}$$

where $\overline{v_n^2}$ is 8.3×10^{-20} V^2/Hz which is the theoretical thermal noise power spectral density of 50 Ω input at 300 K temperature. Simulations and measurements are carried out at different voltage levels since voltage at the DC-DC converter output is not constant; it can take a value in the range between 0.5 V- 1.8 V (Figure 3.24) during the intermittent operation. The simulated and measured gain and input referred noise voltage density curves of the two-stage amplifier are shown in Figure 4.4. The results show that passive amplification in the LC tank in combination with the very high input impedance of the LNA is sufficient for suppressing the noise and obtaining a low input referred noise voltage density of 4 nV/$\sqrt{\text{Hz}}$ at 0.65 V supply voltage and 2.5 nV at 1.6 V supply voltage. The gain obtained from the passive amplification in the LC

tank is 28 dB; thus, the designed two-stage amplifier has a total gain value of 58 dB at 0.65 V and 68 dB at 1.6 V. The results confirm that the presented design can still operate at a voltage supply of 0.65 V consuming 0.35 mA. At 1.2 V supply voltage, the total current consumption of the two stage amplifier increases to 1.2 mA.

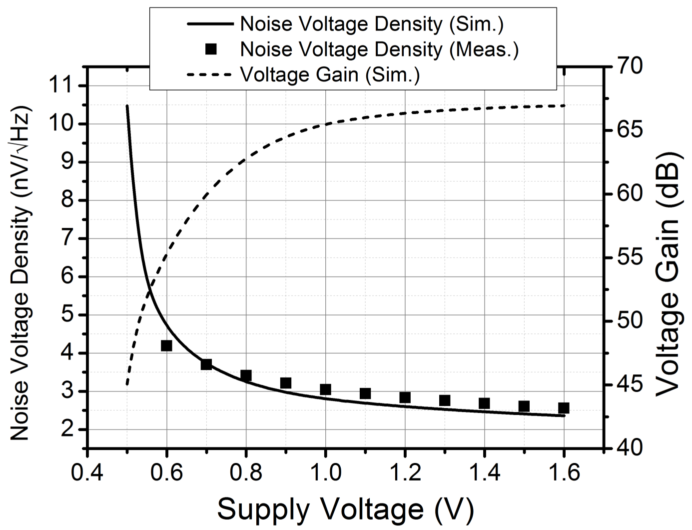

Figure 4.4. Simulated and measured input referred noise voltage density,voltage gain and supply voltage relation of two-stage amplifier at 63.86 MHz.

4.1.2. Active Loaded Gilbert Cell Mixer

Downconversion of MRI signals is carried out by the implemented active loaded fully differential Gilbert mixer shown in Figure 4.5. Gilbert-cell mixer is one of the most commonly used CMOS mixer topologies, due to its high LO rejection, high conversion gain, high dynamic range, and high port to port isolation [59, 61, 95].

The RF inputs of the mixer are directly connected to the outputs of the LNA, while the LO inputs are connected to the outside by DC blocking capacitors. The RF input signal is amplified in the transconductance stage formed by M_1 and M_2 transistors, downconverted to an IF current signal in the LO switch stage formed by M_3, M_4, M_5 and M_6 transistors, and then converted to a voltage by the active load network of M_7 and M_8 transistors. The output of the mixer is connected to a one pole low-pass filter formed by $R_{LP} = 16\,\text{k}\Omega$ and C_{LP} =1 pF, resulting in a corner frequency of 10 MHz. This low pass filter eliminates the high frequency component of the output

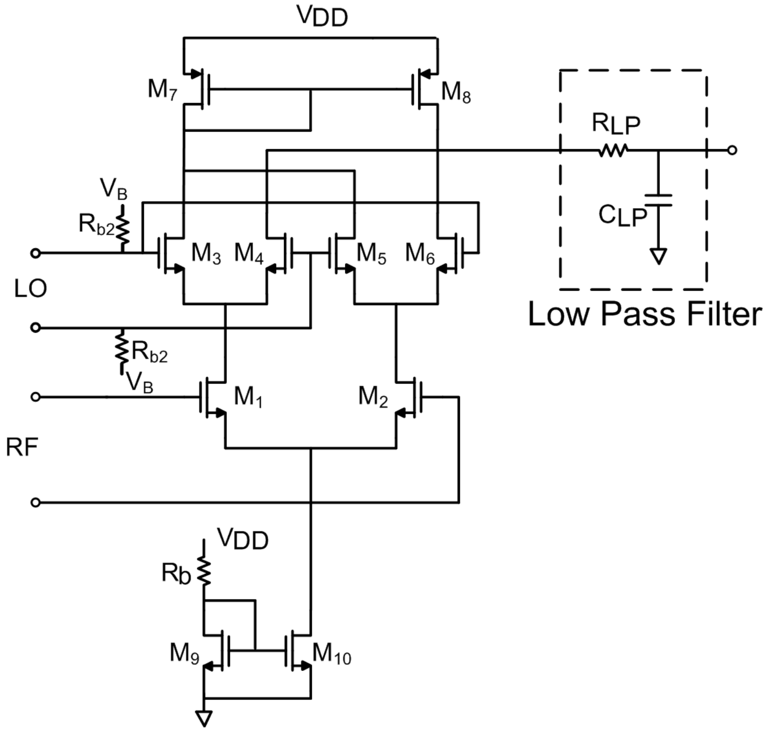

Figure 4.5. Schematics of designed active loaded fully differential Gilbert-cell mixer schematic with the one-pole low pass filter.

signal.

Figure 4.6 shows the simulated single sideband noise figure of the mixer while LO input is at 63.5 MHz and RF input is at 64 MHz at different LO powers. The optimum LO power that provides the minimum noise figure is determined as -4 dBm. The simulations show that noise figure at this LO power is 4.2 dB.

The voltage gain of the mixer is simply

$$A_v \simeq \frac{2}{\pi} g_{m1}(r_{O2}//r_{O8}//(R_{LP} + \frac{1}{\omega C_{LP}})), \tag{4.6}$$

where g_{m1} the transconductance of M1. The mixer is designed to provide 20 dB voltage gain. This is satisfied by setting g_{m1} to 1 mS.

Figure 4.7 shows the the downconversion gain of the mixer at different LO power levels. At 0dBm power simulations show that the mixer has 19.4 dB gain which confirms

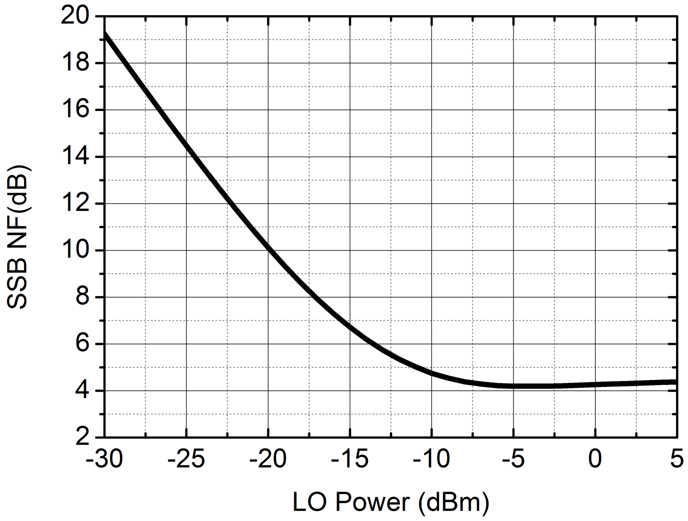

Figure 4.6. The single sideband noise figure of the mixer vs. LO power while LO input is at 63.5 MHz and RF input is at 64 MHz.

the calculations.

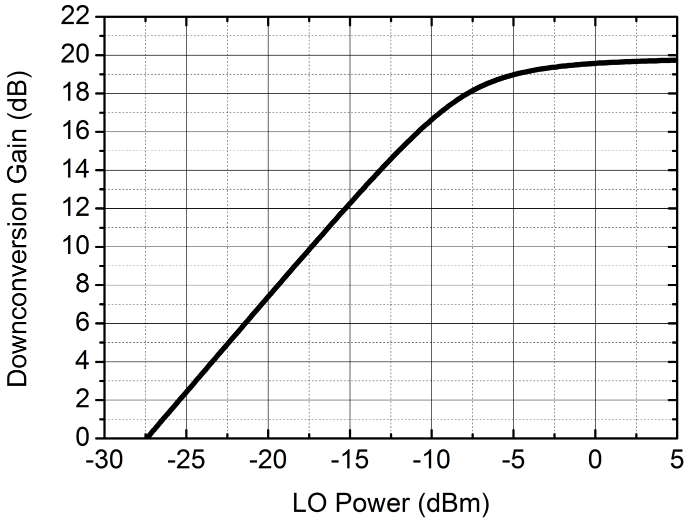

Figure 4.7. The simulated downconversion gain vs. LO power while LO input is at 63.5 MHz and RF input is at 64 MHz.

Together with the passive amplification, the two-stage amplifier, and the mixer, a total 80 dB voltage gain is available in the front-end. The input referred 1-dB compression point is -48 dBm for the designed mixer circuit.

The mixer consumes 0.25 mA at 1.2 V and 0.065 mA at 0.65 V supply voltage, thus the total power consumption of the front-end of the circuit is 1.45 mA at 1.2 V.

4.1.3. Laser Driver

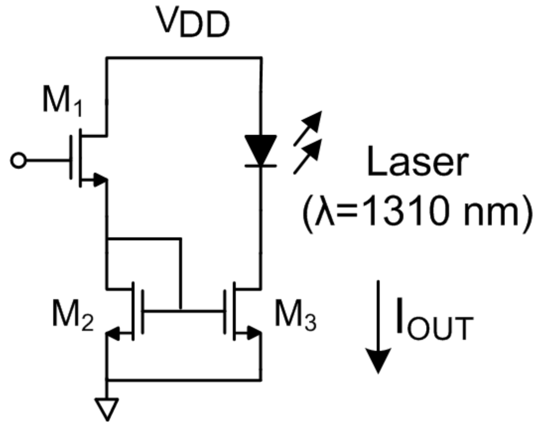

Figure 4.8. The schematic of the laser driver.

The last block of the receiver is the laser driver block. The driver is designed to supply bias current to the output laser diode. Therefore, a current source architecture shown in Figure 4.8 is preferred over a transconductance amplifier structure [96] to ensure the minimum current consumption for different output loads. The M_1 transistor of the driver converts the downconverted voltage to the current which is mirrored and amplified by the current mirror pair of M_2 and M_3. When the anode of the laser diode is connected to the positive supply, the laser driver acts as a current sinking device.

The output current, I_{OUT} of the driver can be calculated as;

$$I_{OUT} \simeq \frac{1}{2}\frac{(W/L)_3}{(W/L)_2}k_p(W/L)_1(V_{OV1})^2, \tag{4.7}$$

where $(W/L)_1$,$(W/L)_2$, and $(W/L)_3$ sizes of M_1, M_2, and M_3 transistors. k_p is the intrinsic transconductance parameter of the technology and V_{OV1} is the overdrive voltage of M_1 transistor. The output current is set to 1 mA at 1.5 V to ensure a detectable light from the output laser. DC Current gain $(W/L)_3/(W/L)_2$ is selected as 8, and $(W/L)_1$ is set to 2.6. Since $k_p \simeq 400 \times 10^{-6}$ A^2/V for the technology, required V_{OV1} is calculated as 0.49 V.

In the continuous mode, the voltage drop on the laser diode is insufficient for turning on the laser diode that has a threshold voltage of 0.85 V. Hence, the operation is not possible with this configuration. Therefore, for the continuous mode, a different configuration is applied; a resistive load (R_L) is connected instead of the laser diode. Cathode of the laser diode is connected to the driver output via a DC blocking capacitor (C_3) and at the same time it is connected to the negative supply on-chip photodiode ($D2$) to obtain the necessary voltage drop on the laser diode for a proper operation.

4.1.4. Optical Receiver

An optical receiver is connected to the fiber coupled laser diode at the output of the receiver. The optical receiver has a peak optical responsivity at 1310 nm which is also the wavelength of the fiber coupled laser diode. An additional amplifier is connected to the receiver output to amplify the signal further for processing.

4.2. Experimental Results

The micrograph of fabricated IC is shown in Figure 4.9. The dimensions of the die are 1.5 mm×1.5 mm. The receiver consumes 230 μm×330 μm area.

There is a range of supply voltage values from 0.6 V to 1.8 V for the system, due to the different configurations. Hence, the supply current - supply voltage relation shown in Figure 4.10 is measured. Results show the receiver together with the output IR laser diode consumes 900 μA at 0.65 V and 2.74 mA at 1.2 V. The values are in good agreement with the simulation results.

4.2.1. Continuous Mode Configuration

For the characterization of the continuous mode, the IC is placed on a PCB which is mounted on an optical breadboard. The system is powered by a 650 nm laser source that can generate a maximum of 200 mW optical power. The laser beam is focused by a convex lens (50 mm of focal length) on two on-chip photodiodes generating

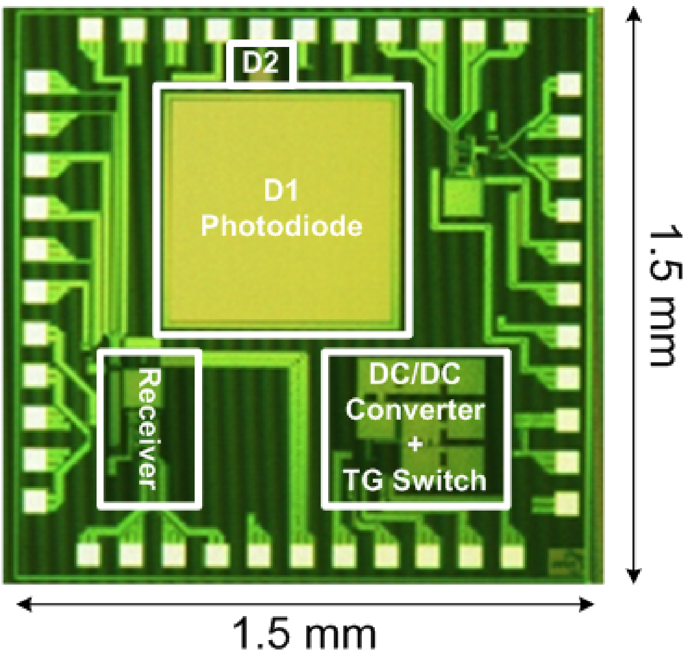

Figure 4.9. Micrograph of the fabricated second generation IC.

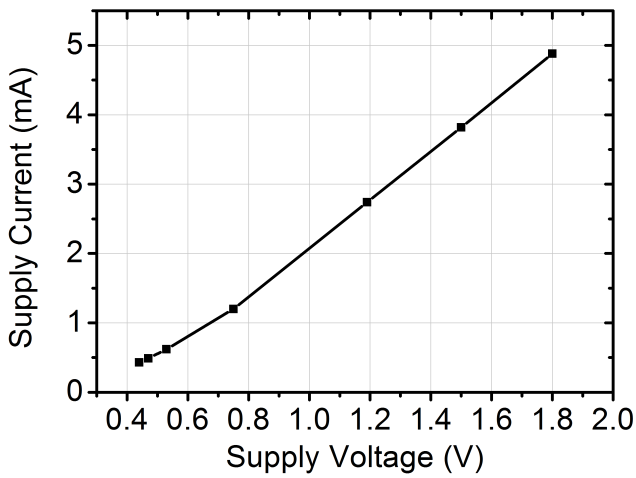

Figure 4.10. Supply current vs supply voltage relation of the second generation system.

positive and negative supply voltages. Rohde & Schwarz SMB100A signal generator emulates the input signal and a Tektronix AFG 3101 function generator supplies the local oscillator signal. The resistive load is $R_L = 1\,\mathrm{k}\Omega$ and the DC block capacitor is $C_3 = 15$ nF. Optical port of the fiber-coupled IR laser is connected to the Avago HFBR 2316TZ IR optical receiver which is cascaded with an external LNA. The external LNA output voltage is monitored by a Rohde & Schwarz FSH600 spectrum analyzer. First, the output spectrum is observed by sweeping the RF signal frequency from

63.81 MHz to 63.91 MHz while keeping LO frequency at 63.46 MHz. Power levels of the laser source, RF input and LO input are set to −15.4 dBm (35 mW), −50 dBm and −7 dBm, respectively. Photo generated voltage of $D1$ is measured as 0.614 V while the voltage induced on $D2$ is 0.24 V. The sweep result showing 100 kHz band centered at 400 kHz in a 200 kHz frequency span is given in Figure 4.11a. The signal-to-noise ratio for the 200 kHz span is measured to be approximately 18 dB at 35 mW optical power. At this optical power level, measurements show that the receiver with the output laser diode consume 700 μW power in the continuous mode configuration. The second experiment measures the forward power transmission at various optical powers while RF input of −50 dBm at 63.86 MHz and the LO input of −7 dBm at 63.46 MHz are used. The results are given in Figure 4.11b. The results show that the system gain can be increased by increasing the incident optical power. The gain of the system is 15 dB at 100 mW optical power; and it is 10 dB at 40 mW optical power. At 20 mW optical power, the gain drops down to 1 dB. Therefore, the minimum detectable signal (MDS) value is also optical power dependent. For a 5 kHz frequency span, the MDS value is measured as −70 dBm at an optical power level of 20 mW; and it is measured as −80 dBm at 40 mW optical power.

4.2.2. Intermittent Mode Configuration

The intermittent operation comprises charging and discharging cycles which result in a fluctuating charge pump output voltage V_S and supply voltage V_{DD}. The fluctuation affects the system performance, hence it is important to create a model to predict V_S value at a certain time.

$$V_S(t) \approx \begin{cases} V_S((n-1)T)e^{\frac{-t+(n-1)T}{\tau_1}} + V_{S,max}\left(1 - e^{\frac{-t+(n-1)T}{\tau_1}}\right) & (4.8) \\ \quad , \text{ for } (n-1)T < t \leq (n-1+D)T, & (4.9) \\ & \\ V_S((n-1+D)T)e^{\frac{-t+(n-1+D)T}{\tau_2}} & \\ \quad , \text{ for } (n-1+D)T < t \leq nT. & (4.10) \end{cases}$$

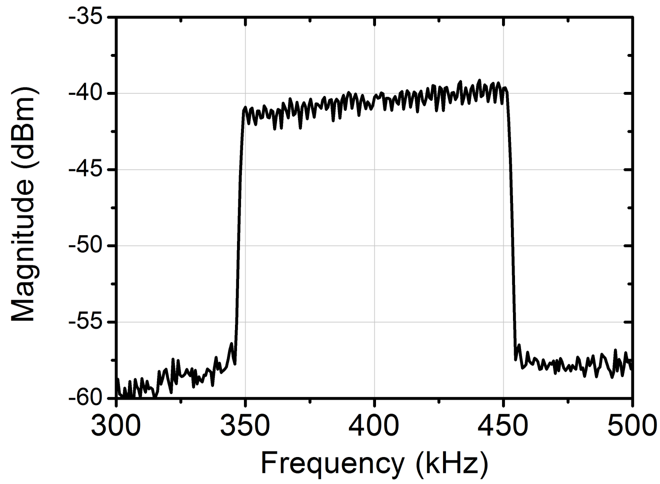

(a)

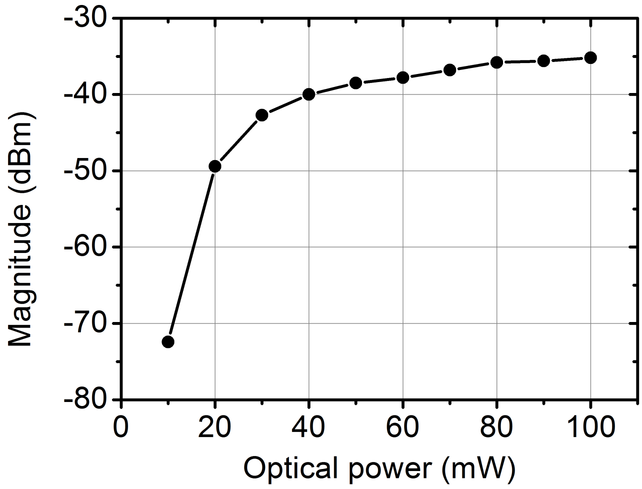

(b)

Figure 4.11. (a) The output spectrum when the input is swept from 63.81 MHz to 63.91 MHz, the LO is -7 dBm at 63.46 MHz, the input is -50 dBm; (b) output power-optical power level relation.

When no initial charge is present in the storage capacitor C_S (i.e. $V_S(0) = 0$) and the incident optical power density assumed constant, the output $V_S(t)$ can be expressed as the functions (3a) and (3b), where $n = 1, 2, ...$ is the cycle number, T is the period of the transmission gate control signal, D is the duty cycle of the control signal, $\tau_1 = R_{O,dcdc}C_S$ where $R_{O,dcdc}$ is calculated as $1\,\mathrm{k\Omega}$ and the storage capacitor (C_S) is $10\,\mu$F, thus τ_1=10 ms. $\tau_2 \approx R_{DD}C_S$ where R_{DD} is the equivalent system resistance and it can be calculated using Figure 4.10 as $350\,\Omega$. Thus $\tau_2 \approx 3.5$ ms. V_{Smax} is calculated as 1.95 V using Equation 3.6, when V_{PD}=0.65 V and I_S=0. However, due to parasitic losses, V_{Smax} is measured as 1.6 V which is used in the calculations. The model is verified experimentally as shown in Figure 4.12. An off-chip 330 kΩ pull-up resistance (R_S) is used in the experiments. The 650 nm laser source is modulated with a signal that has T=40 ms period. The duty cycle of the signal (D) is set to 95%. The laser power is set to 40 mW. The model successfully predicts the behavior of the system. Using the values above, the peak value of V_S is calculated as 1.58 V and the minimum V_S is calculated as 0.88 V which is experimentally found to be 0.92 V. It is important to note that there is a trade-off between operation speed and the V_S value. The operation duration can be decreased by decreasing T and increasing D; on the other hand both parameters affect the achievable peak and the minimum V_S values.

Additionally, the average supply current value I_{DD} that is consumed during the discharge can be calculated using the following equation

$$I_{DD} = C_S \frac{\Delta V_{DD}}{\Delta t}, \tag{4.11}$$

where C_S is the storage capacitor of 10 μF, ΔV_{DD} is the voltage drop of $1.6\,\mathrm{V} - 0.92\,\mathrm{V} = 0.68\,\mathrm{V}$, and Δt is the discharge time of 2 ms. I_{DD} is found to be 3.4 mA which is in good agreement with the simulated results. The overall average power consumption is inversely proportional to D, and it can be calculated as $(1 - D)V_{Sa}I_{DD}$ where V_{Sa} is the average V_S value during discharge time. With D =0.95 and V_{Sa}=1.26 V, the average power consumption is 214 μW for the experiment.

After confirmation of the successful operation of the optical power supply unit, the performance of the receiver is tested in the same configuration. The input power is set to -50 dBm at a frequency of 63.86 MHz and LO power is set to -7 dBm at 63.46 MHz frequency. The spectrum of detected signal shown in Figure 4.13 has multiple components centered around 400 kHz due to the rectangular shape of the output signal. The maximum peak is observed at 400 kHz with a power of -34 dBm which is approximately 6 dB greater than the result obtained in the continuous mode.

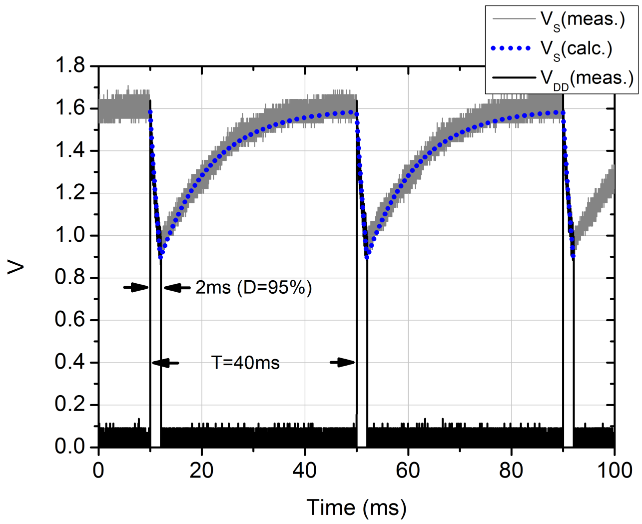

Figure 4.12. V_S and V_{DD} node voltages in the switched mode configuration at 40 mW peak optical power, T=40 ms, D=95%.

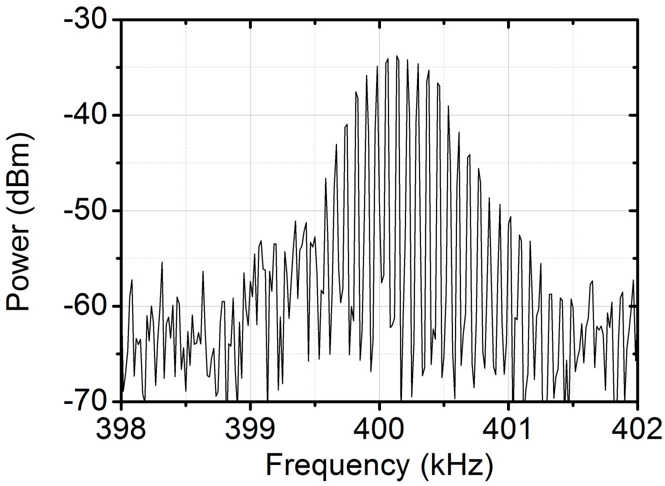

Figure 4.13. The spectrum of detected signal in intemittent mode configuration, when the input is -50 dBm at 63.86 MHz, the LO is -7 dBm at 63.46 MHz, optical power is 40 mW, T=40 ms, D=95%.

Measurement results show that both configurations can be used for detecting ultra low power signals down to -80 dBm, however both configurations have their own advantages. The continuous mode has higher transmission throughput with higher power consumption; on the other hand, due to the limited efficiency of the optical power supply unit, the intermittent mode consumes lower power with a lower throughput. However, the higher supply voltage value results a higher gain in the receiver for the intermittent mode. In addition, the intermittent configuration requires an optical switching operation which is a more complex operation than the continuous operation.

5. THIRD GENERATION ARCHITECTURE

In the third generation architecture, some design goals are set to improve the second generation and to realize a monolithic architecture that can be tested in MRI environment. The first design goal is improving the overall receiver front-end gain from 80 dB to 120 dB by adding some IF gain stages. Secondly, in order to obtain a monolithic architecture, the discrete components used in the previous generation are replaced by their on-chip counterparts. Additionally, in order to test the system in MRI environment, novel operational schemes are implemented to supply the LO signal in a wireless manner.

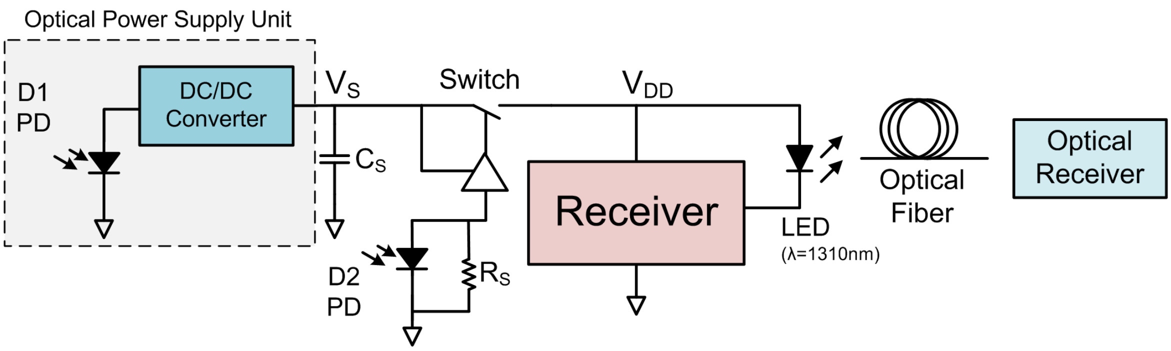

Figure 5.1. Intermittent configuration implemented in the third generation system.

The intermittent configuration for the third generation architecture is shown in Figure 5.1. In the configuration point of view, the only change is in the switch architecture, where a transmission gate type of switch is changed with a simple pMOS switch. D2 photodiode in this generation is a secondary triple-well photodiode, and it is connected to a low voltage buffer that boosts the photodiode voltage. Only three discrete components are used. A resistor, R_S, that enables a discharge path for the D2 photodiode is required. However, in future realizations, this resistor can also be implemented on-chip. Storage capacitor C_S acts as the battery, and due to the required large value, it is kept as a discrete component. The last discrete component is the output LED. In this generation, LED is preferred over laser, due to its availability as a receiver-transceiver pair. The continuous mode configuration is not targeted for this generation of the system.

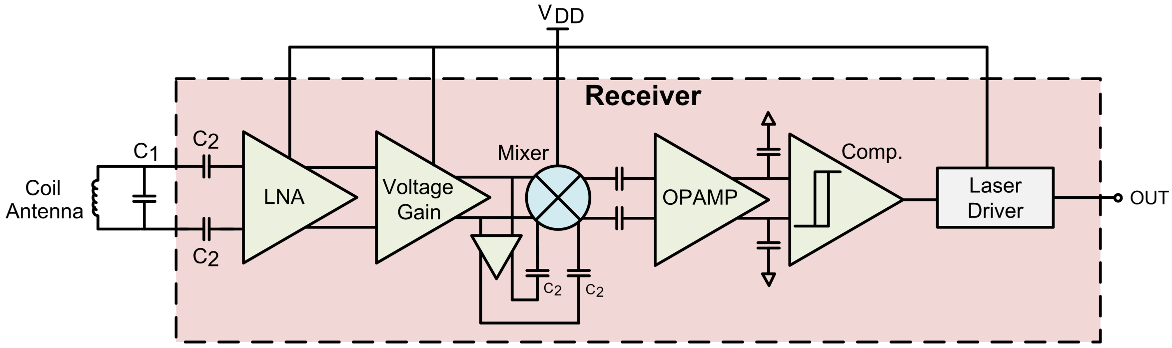

Figure 5.2. The block diagram of the third generation direct conversion receiver in the self-mixing configuration.

5.1. Receiver Architecture

The receiver architecture is updated to the architecture shown in Figure 5.2. Fully differential LNA from the previous generation is kept. Electrostatic discharge (ESD) protection diodes are added to the inputs of the LNA to provide a passive detuning for the MRI experiments, and protect the circuits from high powered RF excitation pulses. All DC blocking capacitors are implemented as on-chip in this generation. Instead of previously utilized 100 nF discrete capacitors, 10 pF on-chip counterparts are preferred. Mixer is also updated to a fully differential Gilbert-cell mixer. Output of the mixer is connected to the IF stages formed by an op-amp and a comparator. Additional IF stages provides additional gain that the over-all voltage gain in the receiver chain is increased to 120 dB that will permit acquiring very low power MRI signals. Self-mixing architecture is utilized by providing a secondary RF pulse as a LO oscillator signal. This signal is generated by the MRI scanner by programming a dedicated localization pulse sequence [97].

In order to provide a constant light intensity for the LED at the large voltage supply ripple present due to the intermittent nature of the operation, a self-biasing supply independent current source is designed. The updated driver can deliver 2.0 mA current within the supply range of 0.5 V to 1.8 V. In this way, power dissipation is minimized for the target range. Overall receiver consumption is simulated to be 3 mA at 1.2 V.

5.1.1. Fully Differential Gilbert-Cell Mixer

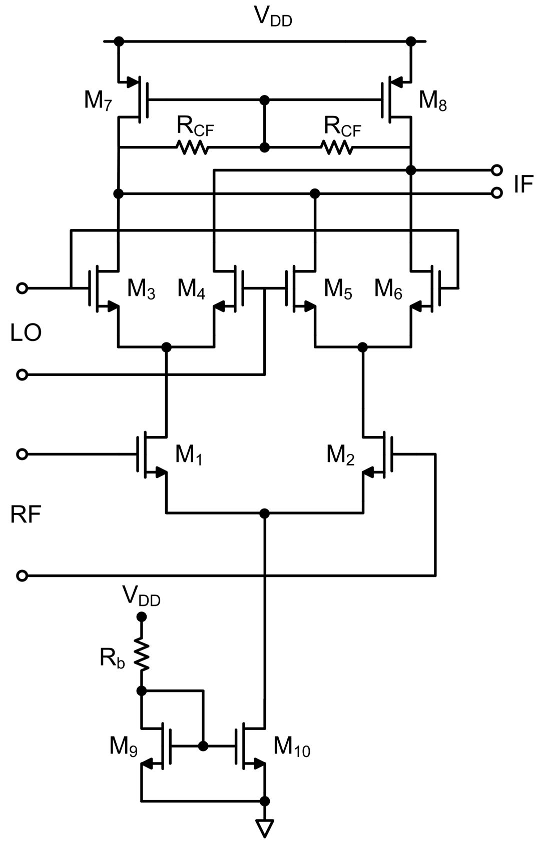

Figure 5.3. The mixer circuit incorporated in the third generation receiver.

Figure 5.3 shows the double balanced Gilbert-cell mixer utilized in the third generation receiver, the mixer is improved upon the previous generation by adding the local common mode feedback circuit formed by R_{Cf} resistors. The added local common mode feedback circuit surpasses any common mode signal at the output nodes of the mixer to increase the dynamic range of the receiver. The mixer can be used as a squarer for the self-mixing architecture. The mixer can provide 20 dB downconversion gain and 5.45 dB NF while consuming 0.24 mA at 1.2 V supply voltage. The noise figure value increase over the second generation mixer is related to the implemented local resistive common mode feedback network that increases the input noise of the mixer.

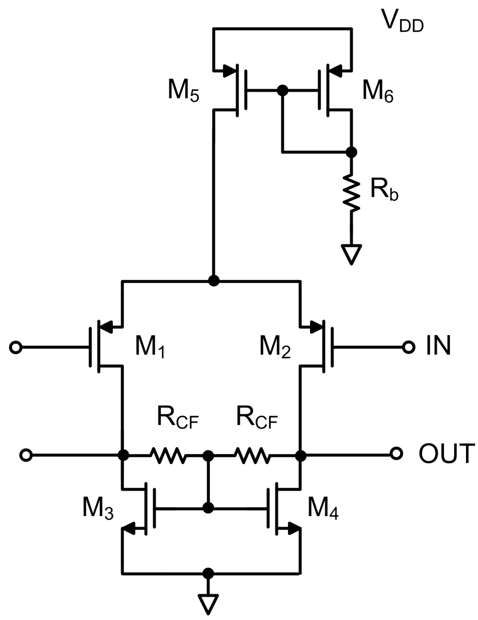

Figure 5.4. The differential amplifier utilized to boost the downconverted IF signal.

5.1.2. Fully Differential Amplifier

A simple fully differential amplifier is designed to increase the amplitude of the downconverted IF signals. The amplifier has the local common-mode feedback circuit formed by R_{cf} resistors to cancel the common-mode noise out. AC coupling is considered, since the direct coupling of the amplifier requires modification of the previous block which is the mixer. The coupling capacitors are 10 pF. The biasing voltage is set to 575 mV at 1.2 V and it is supplied via a 100 kΩ resistor to the input transistors of the amplifier. The differential amplifier consumes 170 μA current at 1.2 V supply voltage. Simulated frequency response of the amplifier is shown in Figure 5.5. The differential gain of the amplifier is 29.7 dB. The lower 3 dB frequency is 106 kHz; and, the upper 3dB frequency is 11.5 MHz.

5.1.3. Comparator

Figure 5.6b shows the comparator utilized to obtain square like signals from the amplified downconverted IF signals. The comparator is formed by a cross-coupled pair. Both outputs of the amplifier is connected to the corresponding comparator inputs. In this way, the induced FID signals that have an amplitude of 10 μV generate a pulse

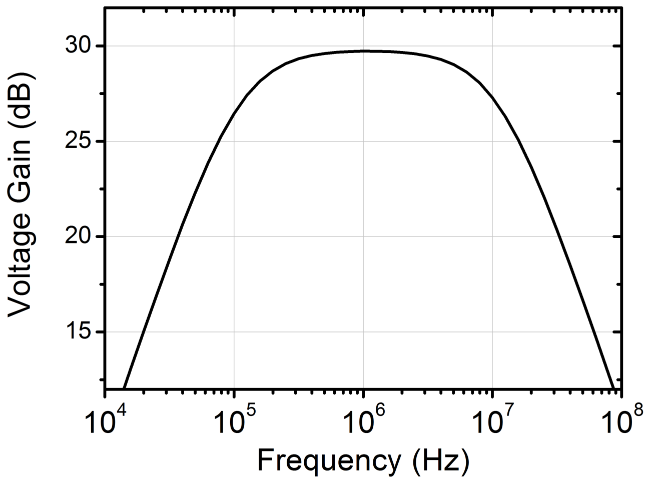

Figure 5.5. Frequency response of the differential amplifier.

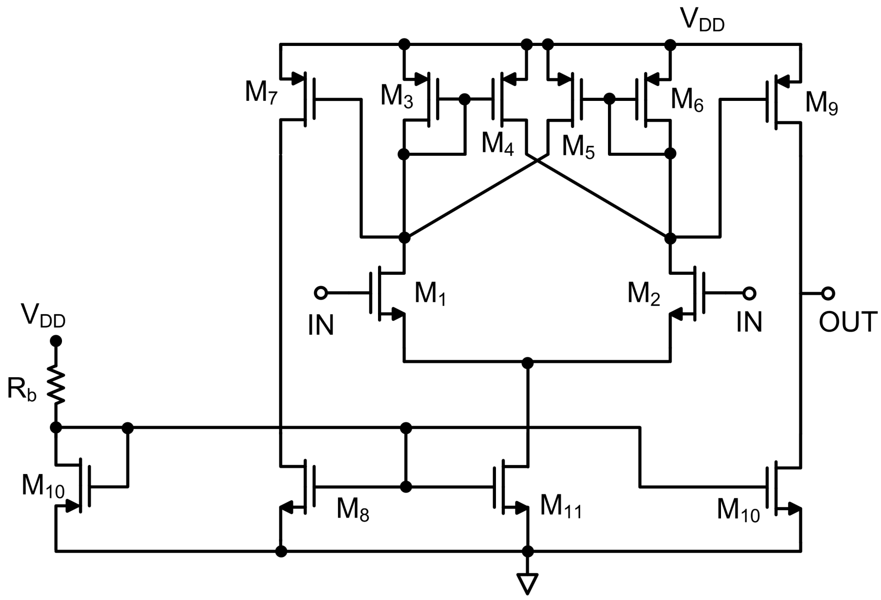

Figure 5.6. The comparator added to obtain square shaped IF signals.

shaped signal at the comparator output. The pulse signal is preferred to obtain a better performance in the laser driver; since the output laser diode is considered to be modulated in a switching fashion. The comparator consumes an average current of $35\,\mu$A at $1.2\,$V supply voltage.

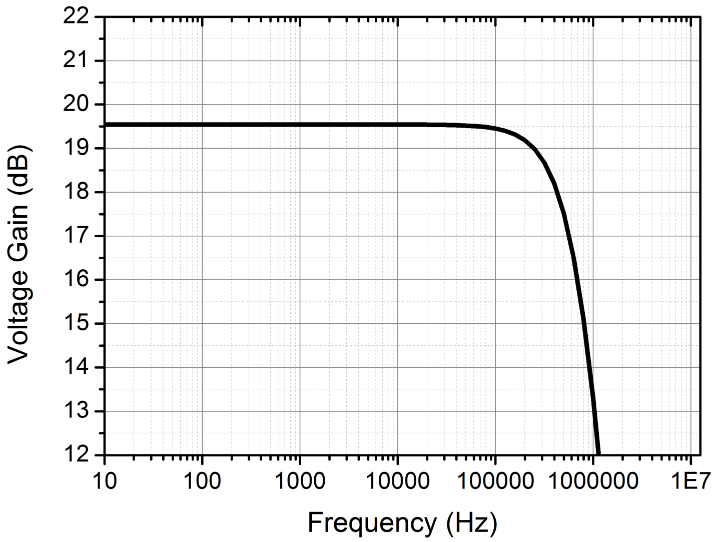

Figure 5.7. Frequency response of the comparator.

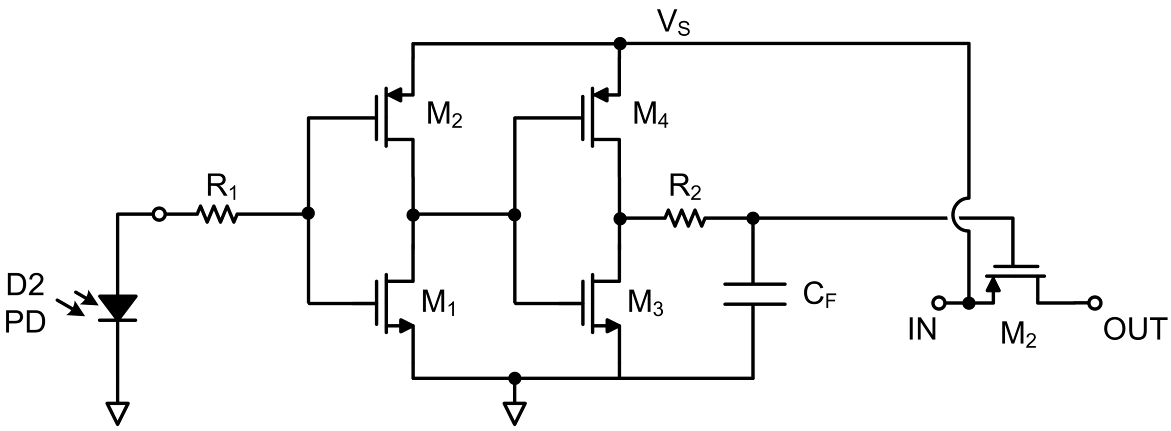

Figure 5.8. Schematic of the third generation optical switch.

5.1.4. Optical Switch

Optical switch is shown in Figure 5.8. The structure is much more advanced then the previous generation simple transmission gate switch. Control input of the switch is connected to a triple-well photodiode. The low voltage on the photodiode is increased by a buffer designed with low voltage transistors. Power to the buffer is supplied from the input node, which is the output of the charge-pump and denoted as V_S. Simulation given in Figure 5.9 shows that the switch can operate properly down to 0.2 V control input voltage. In the simulation, a 320 Ω resistor is connected to the output of the switch as the impedance of the receiver together with the laser diode. The resistance of the switch is calculated to be 5.41 Ω, therefore, the input and output of the switch can be considered equal in the calculations. The low control voltage range of the switch also allows to a broader range of optical powers to be used in coupling process, since the sensitivity of the switch increased.

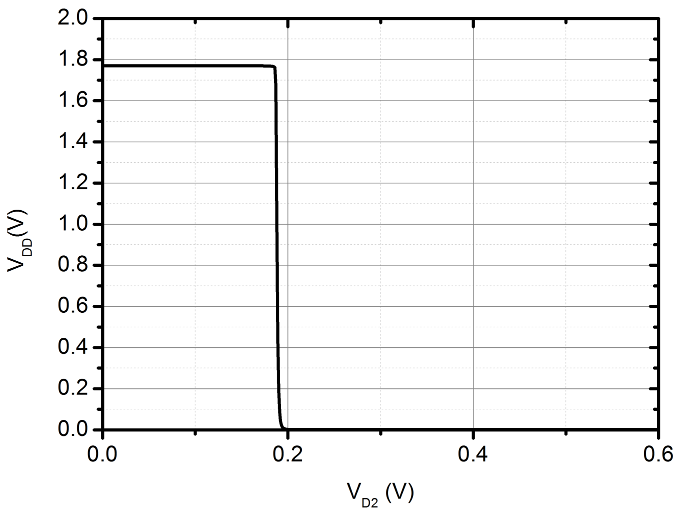

Figure 5.9. DC simulation of the optical switch, the series resistance is 5.41 at 320Ω equivalent system resistance.

5.1.5. ESD Protection Diodes

ESD diodes are added to protect the circuit against damage during RF excitation in MRI experiments. The diodes also work as a passive detuning circuit which used to alter the resonance frequency of the circuit formed by the input antenna and matching capacitor. The high power RF excitation signal turns on this diodes and added capacitance value shifts the resonance frequency value to lower bands. In this way, the homogeneity is preserved in the MRI scanner.

5.1.6. Self Biasing LED Driver

The output of the second generation LED/laser driver shown in Figure 4.8 is supply dependent. The dependency of the output current to the supply voltage is a big concern for the intermittent configuration, due to the large supply voltage ripple that can have the values up to 500 mV. Since intensity of light emitted by the LED

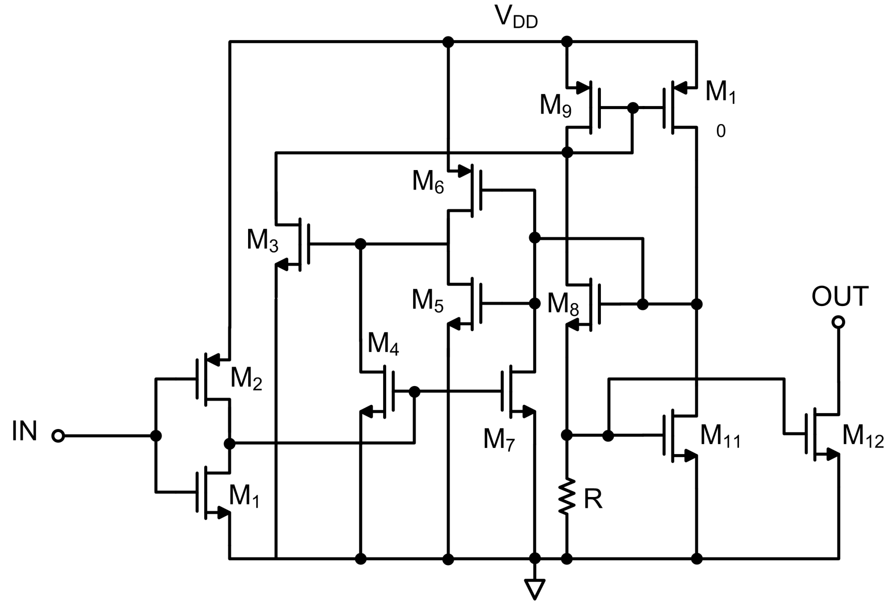

Figure 5.10. Schematics of the designed self-biasing, supply independent LED driver.

is linearly proportional to the applied current [51], there is a relation between supply voltage and the light intensity for a supply dependent driver. This dependency may result an insufficient optical transmission even the receiver architecture is operating properly. Hence, a supply independent LED driver is required for ensuring a proper optical transmission.

In the third generation, the output driver architecture has been updated to a self-biasing, supply independent architecture shown in Figure 5.10. The circuit is basically a self-biasing current source circuit [77]. The supply independency of the circuit can be explained as follows. The connection of a current source formed by M_8, M_{11} and R and the current mirror formed by M_9 and M_{10} constitute a positive feedback loop. The gain around this loop is the gain of the current source. If this gain is set to a value less than unity, the positive feedback loop becomes stable which results in a supply independent operation.

However, in practice, there is also a secondary stable point where the loop gain is less than unity. At the start up of the circuit, transistor currents are too small and due to the leakage currents and other effects, the loop gain becomes less than unity. As a result, this type of circuits usually unable to drive themselves out of the zero initial current point.

The zero-current state can be avoided by utilizing a start-up circuit that ensures some current flow in the transistors. As an additional requirement, this start-up circuit must not interfere with the operation of the current-source architecture. In the designed driver, M_5, M_6, and M_3 form a start-up circuit. M_5 and M_6 act as an inverter that turns on M_3 transistor if the gate of M_8 is stucked at ground. M_3 then generates at the gates of the current-mirror formed by M_9 and M_{10} . After the circuit starts to operate, the potential of the gates of M_5 and M_6 reaches a high value and all start-up configuration ceases to work.

The output of the driver is defined by the current source formed by M_8, M_{11} . The output of the current source can be written as [77]

$$I_2 = \frac{V_{GS11}}{R} = \frac{V_t + V_{OV11}}{R} = \frac{V_t + \sqrt{\frac{2I_1}{k_p(W/L)_{11}}}}{R}. \tag{5.1}$$

The output of the driver is supplied by M_{12} transistor which mirrors the output of the current source.

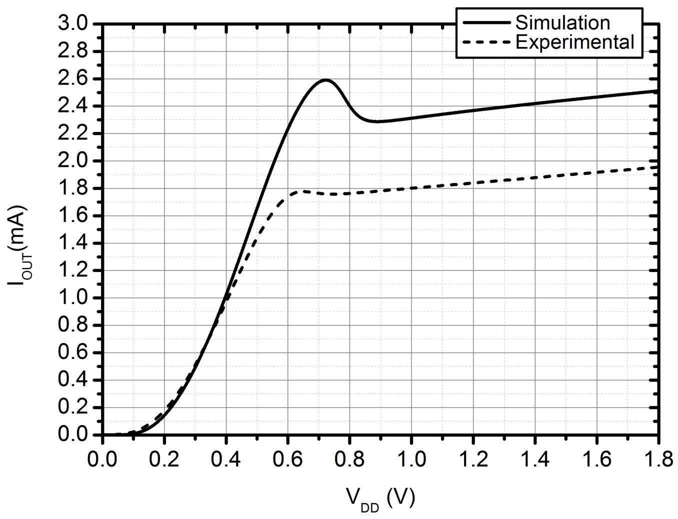

Figure 5.11. The output current vs supply voltage graphic of the laser driver when the driver input is grounded.

The LED driver is designed to deliver 2 mA current to the LED. Simulation results and the experimental results are given in the Figure 5.11. In the measurement and simulation, the supply voltage is swept from 0 V to 1.8 V. Measurements show that the circuit can supply a stable current for the supply voltages higher than 0.6 V. There is a 500 μA difference between measured and simulated values due to the fact that input of the source is not readily available for output connections. Nevertheless, measurements confirm the supply independency of the driver.

5.1.7. Output LED

At the output of the receiver, an LED (Avago 1312TZ) with a wavelength of 1310 nm is used. The current-voltage characteristics area shown in Figure. The LED requires 0.85 V while it consumes 2 mA current which supplied by the laser driver. An optical receiver (Avago 2316) is connected to the output LED. The optical receiver has a peak optical responsivity at 1310 nm. An additional amplifier is connected to the receiver output to amplify the signal further for processing.

5.2. Experimental Results

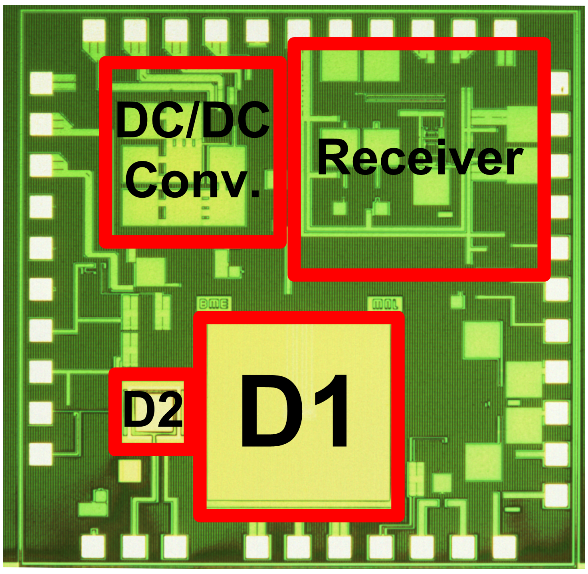

Figure 5.12. Micrograph of the third generation IC.

The micrograph of fabricated IC is shown in Figure 2.11. The dimensions of the die are 1.5 mm×1.5 mm. Receiver covers an area of 0.25 mm^2 which is approximately

11% of the overall integrated circuit.

The system is characterized for determining the required parameters for the MRI Environment. Several experiments are carried out to determine the system performance. The system is in the intermittent configuration in all of the experiments. A test PCB, shown in Figure 5.13, with a C_S of 22 μF and R_S of 330 kΩ is fabricated. No other discrete component is used. Butt-coupled ICs are placed on this PCB during the experiments.

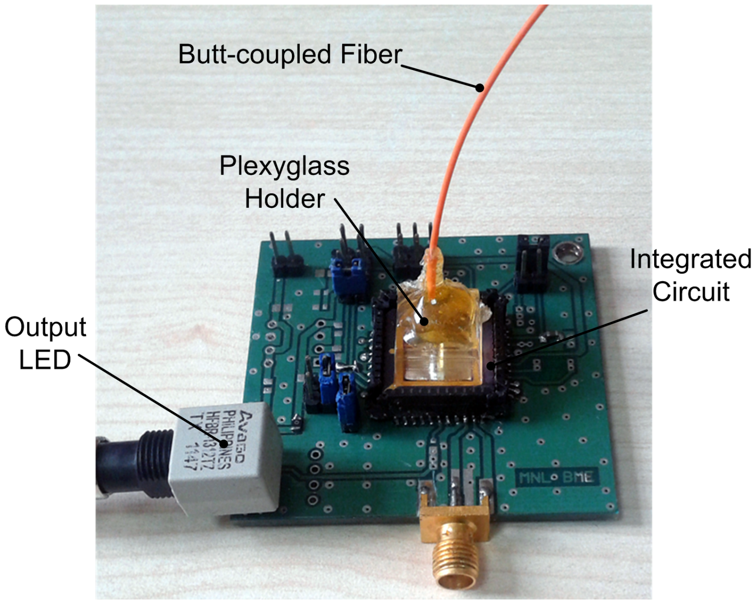

Figure 5.13. Photograph of the test board that holds the butt-coupled third generation IC.

5.2.1. System Characterization

The DC power consumption is an important parameter due to intermittent nature of the operation. The experimental result is shown in Figure 5.14. The system consumes 3.5 mA at 1.2 V. The equivalent impedance is calculated to be 320 Ω.

Due to the implemented noise figure method, the coil has to resonate with the receiver in order to obtain low noise figure. The input impedance measurements are carried out. Figure 5.15 shows the result which is 4.445 pF at 123.2 MHz. This value resonates with 402.22 nH at 120 MHz.

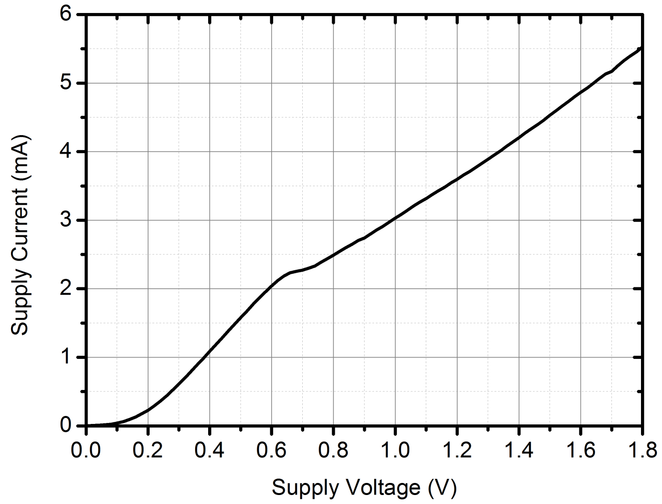

Figure 5.14. The supply current-supply voltage relation of the overall third generation system.

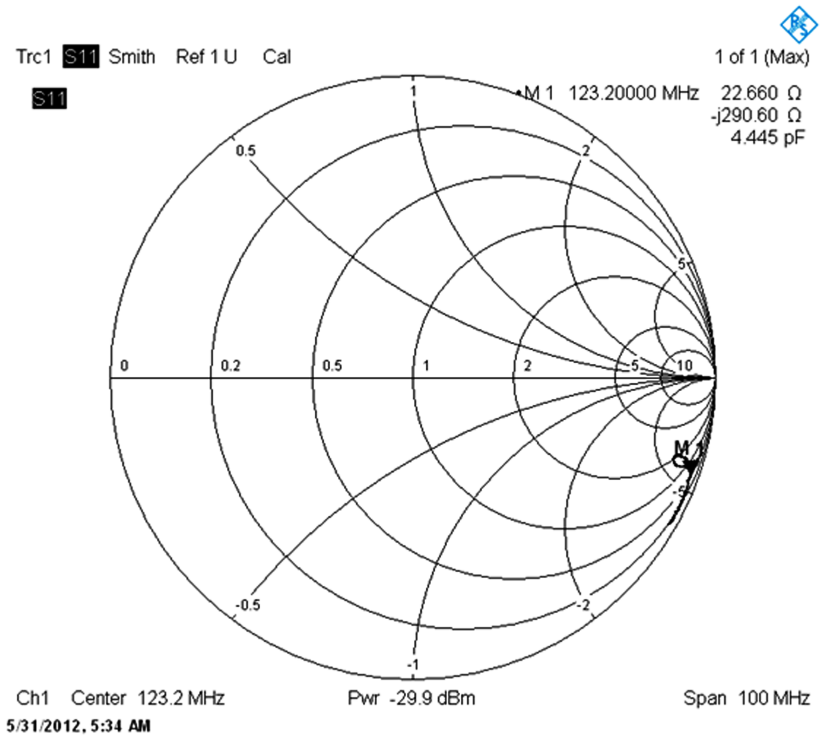

Figure 5.15. S11 measurement of the third generation receiver.

SNR dependance on the other circuit paramaters are also tested. Rohde&Schwartz SMB100A signal generator is used as the MRI response input while Hameg HMF2550 function generator is used as the secondary RF local oscillator signal. These two signals are combined with a Minicircuits ZFSC 2-372-S+ combiner which is connected to the input of the receiver. Measured SNR and the supply voltage relation, V_{DD}, is shown in Figure 5.16. Experimental results show that the SNR value is maximized when the supply voltage is 1.3 V. This supply voltage value is targeted in the MRI experiments.

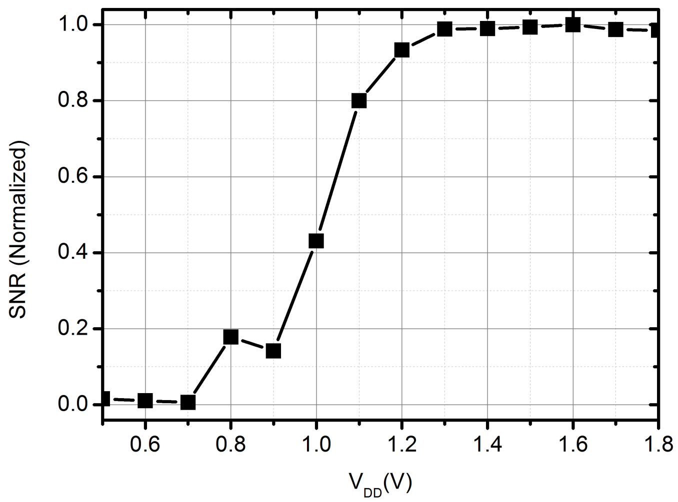

Figure 5.16. SNR relation to the V_{DD} value.

A fiber coupled 660 nm laser (CUBE 660-75 FP) laser is connected to the IC to the butt-coupled pig tailed fiber cable. Laser is modulated with a rectangular pulse signal with period, T, of 40 ms and duty cycle of 90%. SNR change with the optical power shown in Figure 5.17 is observed. The results show that after 45mW of optical power the receiver saturates and SNR reaches its maximum value. Thus, greater optical power levels than 45 mW is needed to obtain the maximum performance.

The SNR relation to the period of the modulation signal is also observed. The experimental results are given in Figure 5.18. The results show that the system can deliver satisfying SNR values with signals that has a period of 20 ms; however, for obtaining the maximum performance, the period should be increased above 40 ms.

Finally the time domain experiments are carried out. The V_S and V_{DD} values are observed with a LéCroy WR6100A oscilloscope. The period of the modulation signal is set to 40 ms, pulse width is set to 1 ms, and the optical power is set to 60 mW. Experimental results are shown in Figure 5.19. The results show that the supply voltage varies between 1.5 V and 1.25 V which is in the desired range. These values are

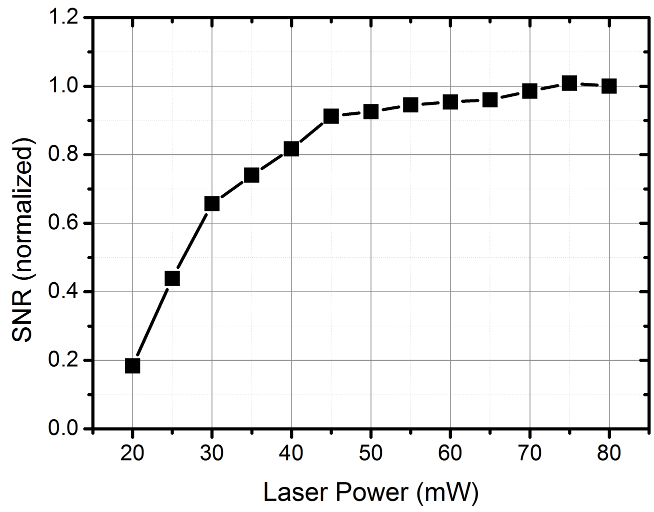

Figure 5.17. SNR value relation to the applied optical power, T=40 ms, DC= 90%.

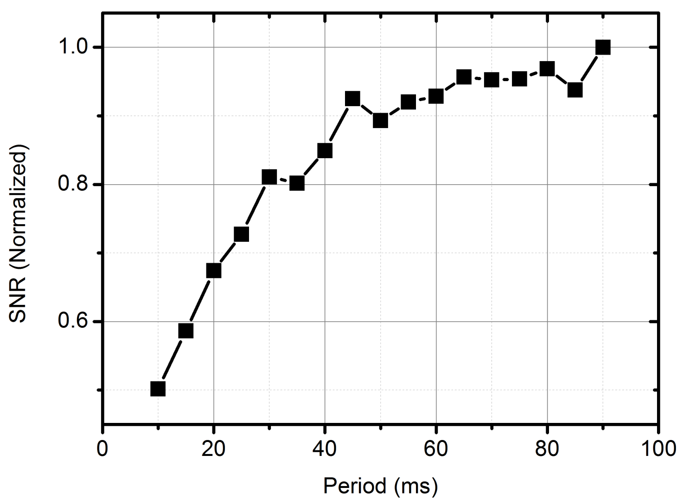

Figure 5.18. SNR relation with the period of the rectangular pulse in the intermittent mode.

set in the system for the MRI experiments.

5.2.2. Experiments in the MRI Environment

The system is tested in Simens 3 T MAGNETOM Trip MRI environment in UMRAM, Bilkent University CyberPark, Ankara. The experimental setup is shown in Figure 5.20. A synchronization signal is taken form the MRI scanner. This signal is

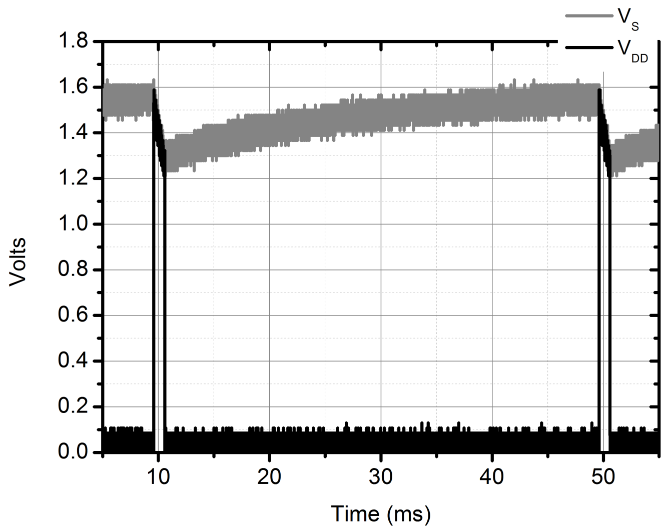

Figure 5.19. Intermittent mode measurement, T=40 ms, DC=90% at the optical power of 60 mW.

used as the modulation signal. Signal period is set to 40 ms and the acquisition time is set to 1 ms. The laser is connected to the IC which is placed in the MRI bore via a 6 m long multi mode fiber cable with a core diameter of 62.5 μm. The output of the LED is connected to the outside optical receiver via a 6 m multimode fiber cable with a core diameter of 62.5 μm. Output of this receiver is connected to an Agilent DSO6104A oscilloscope via a Stanford Research Systems SR445A voltage amplifier with a pre-set voltage gain of 56 dB.

Photograph of the scanner-side of the experimental setup is shown in Figure 5.21. The coil is placed in a phantom prepared with a 0.9% NaCl solution that is filled in a plastic capsule. This capsule is sealed with an epoxy adhesive. The small volume of the capsule prevents the receiver of the MRI scanner operate properly. Therefore, the PCB is attached to a phantom bottle to increase the number of spins in the MRI scanner. Additionally, this bottle acts like the tissue which covers the catheter tip. The coil is placed into a plexyglass phantom holder to confine the antenna orientation.

The RF excitation pulse power and the secondary RF pulse power is varied on the MRI scanner by adjusting the flip angles. RF excitation pulse flip angle (FA) is swept from 5° to 30°. Higher flip angles are avoided since it may result an inhomogeneity

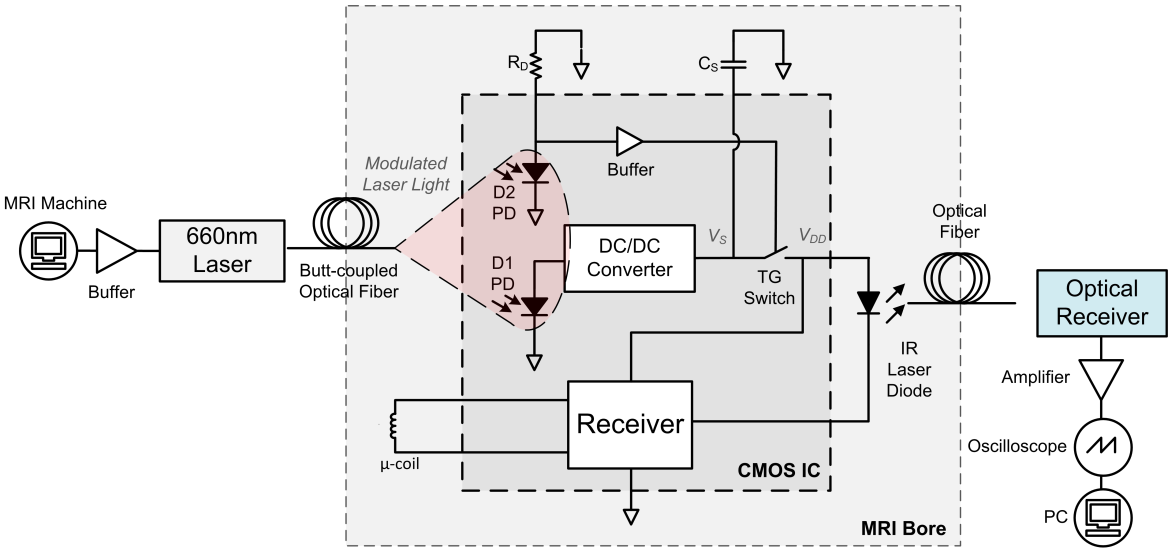

Figure 5.20. The MRI experiment setup.

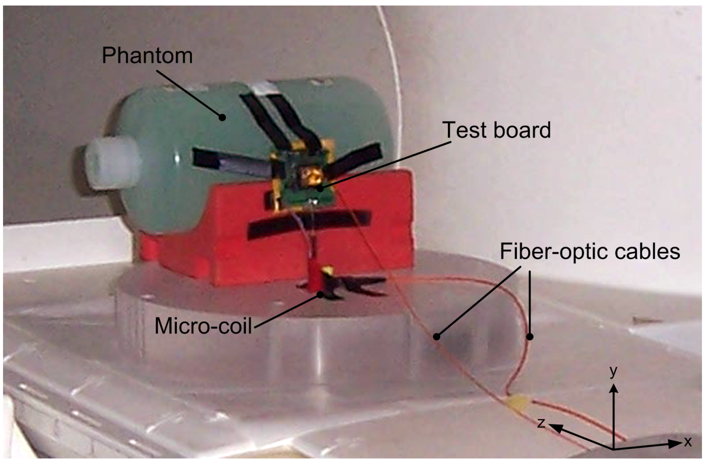

Figure 5.21. Experiment setup in the Siemens 3 T MRI machine.

in the magnetic field. The secondary RF pulse that used as a reference value is a rectangular pulse. Its flip angle (RPA) is swept from 0.5° to 4°. Higher flip angles for the rectangular pulse are avoided to prevent the DC-offset generation in the mixer circuitry. All experiments are done with different gradient values that change from 2.35 mT/m to 7.05 mT/m. A custom localization pulse sequence is developed for the experiments [97]. Dephasing gradient (Figure 5.22a) is applied to generate echo signals. The data taken by the oscilloscope (Figure 5.22b) are processed in MATLAB software. A Fast-Fourier transform is applied to obtain the spectrum of the signals.

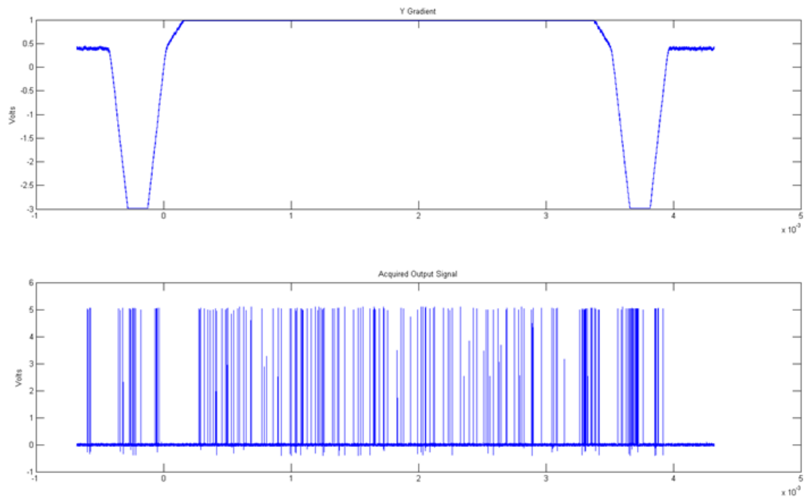

Figure 5.22. Applied x-gradient, and an example received time domain signal.

The locations of the coil can be found from the frequency values as;

$$\Delta x = \frac{f_x - (f_{\text{isocenter}} - f_{ref})}{\gamma G_x}, \tag{5.2}$$

where Δx is the distance from the isocenter, f_x is the received frequency, f_{ref} is the frequency of the secondary RF pulse, $f_{\text{isocenter}}$ is the frequency of the isocenter, and G_x is the gradient strength applied in the x direction.

The setup is moved to four different locations in the x-dimension (left-right or lateral) of the MRI scanner. FA=20°, RPA=2°, laser power is set to 60 mW, G_x is set to 7.05 mT/m, $f_{\text{isocenter}}$ is 123.248102 MHz, and the secondary pulse is at 122.948102 MHz which makes $(f_{\text{isocenter}} - f_{ref})$=300 kHz. This means that a perfect alignment of the coil with the isocenter of the MRI scanner results a 300 kHz signal, and the downconverted band is centered at 300 kHz.

Expected frequency bandwidth is related to G_x and the bore diameter of the scanner. The MRI bore is 0.7 m in diameter, therefore the expected frequency bandwidth is $0.7\gamma G_x$. Hence, the frequency of the output signals are expected to be in the 300 kHz-$0.35\gamma G_x \leq f_x \leq$300 kHz+$0.35\gamma G_x$. Since the G_x is set to 7.05— mT/m, the signals are expected to be in the frequency band between 150 kHz and 450 kHz. Peak detection algorithm is used in this range to find the maximum peak in the band.

The frequency (f_x) obtained from four positions are 263620 Hz, 282690 Hz, 299180 Hz, and 347930 Hz respectively. Equation 5.2 results spatial locations of -12.12 cm, -5.77 cm, -0.27 cm, and 15.97 cm respectively. The negative sign indicates the left half of the lateral plane while the positive values depict the right half. For the sake of clarity these positions are given names as *Left 1*, *Left 2*, *Center*, and *Right* respectively in the text.

The spectrum of the received signals and images gathered by the MRI scanner are shown in Figure 5.22. The coil and the phantom covers it result a white spot in the MRI image, therefore it shows the real location of the coil. Locations from the spectrum are calculated using Equation 5.2, and a white cross hair is placed on the MRI image to indicate the calculated position. Figure 5.22 shows a successful tracking operation for four different positions. The positions are in a great match with the real locations. However, there is an offset of 2 mm for all four positions, which is related to the relatively short acquisition time of 1 ms. The offset is same for all positions, hence it can be considered as a negligible effect.

During the experiments different aspects of the system are tested. The first test is carried out to compare and see the effect of gradient strength on the SNR of the acquired data. For the *Left 1* location, three gathered spectrums are shown together in Figure 5.24 to show the effect of BW on the SNR value. For all locations, gradient is swept from 2.35 mT/m to 7.05 mT/m The results are given in Figure 5.25.

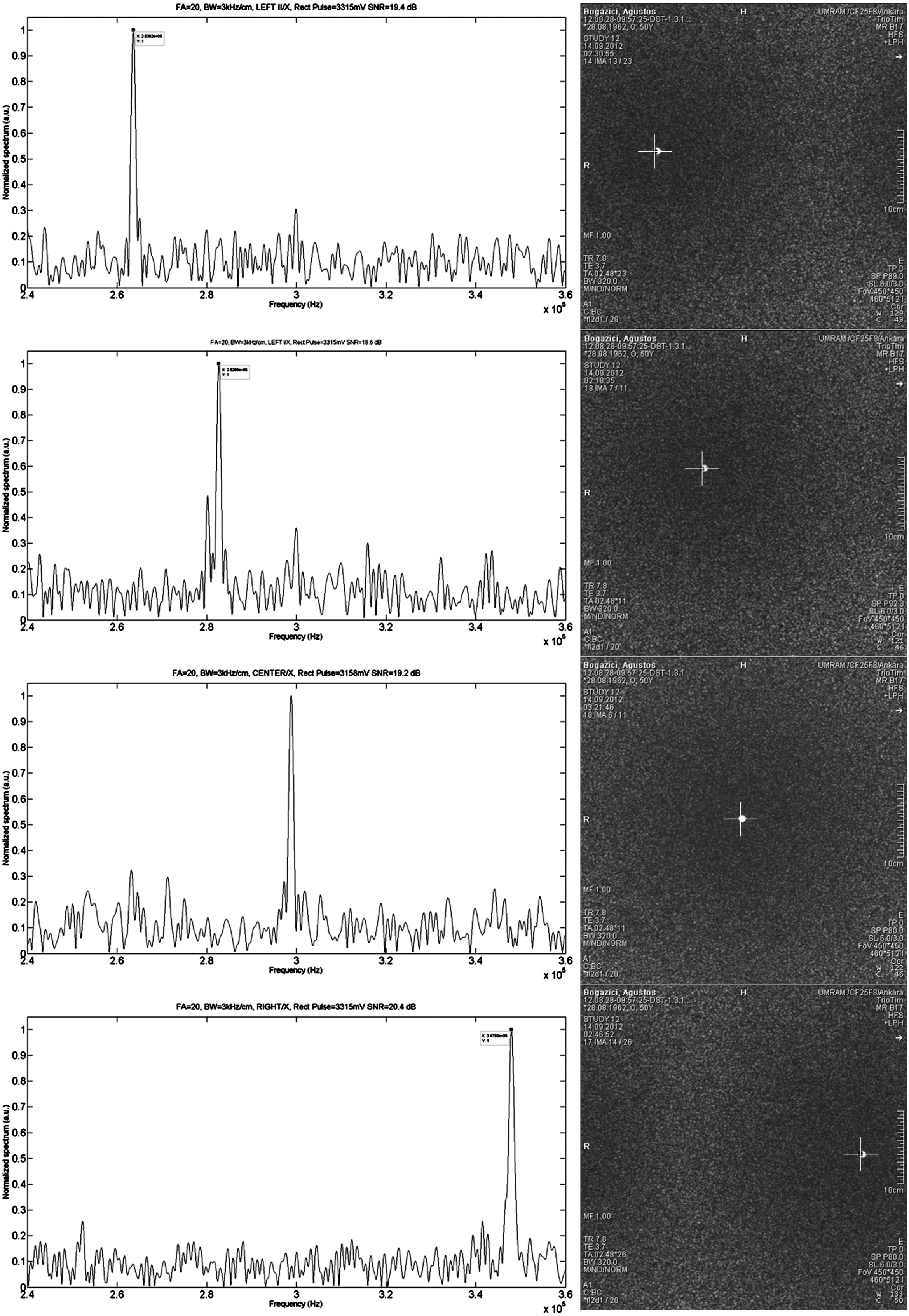

Figure 5.23. Received echo signal spectrum and the representation of the location on the MRI image; the white cross hair shows the calculated locations, FA=20°, G_x=7.05 mT/m, laser power is 60 mW.

Theoretically, SNR of the acquired data is related the gradient by [98]

$$SNR \propto \frac{1}{\sqrt{G}}. \tag{5.3}$$

SNR value is proportional to inverse square root of the gradient, thus, to the spatial resolution. The experiment results confirm the inverse relationship. Maximum SNR is obtained at 2.35 mT/m that is the weakest gradient value applied. The relationship is confirmed for other locations as well. Figure 5.25 shows the results obtained for different locations.

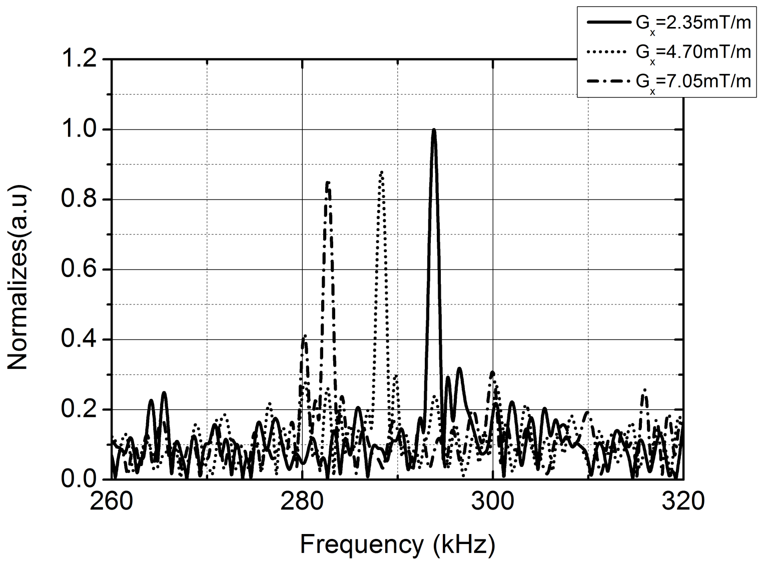

Figure 5.24. Spectrum comparison of the signals gathered from $Left1$ location for different G_x values; FA=20°, RPA=2°, laser power is 60 mW, acquisition time is 1 ms.

In the experiments, flip angle is also varied to observe the effect of the flip angle on the SNR. Figure 5.26 shows the measurement results for the *Center* position. RPA=2°, G_x=7.05 mT/m, laser power is 60 mW, and acquisition time is 1 ms for the experiments. Increasing flip angle increases the SNR since the flip angle is linearly proportional to the applied RF pulse power. Higher flip angles require higher B_1 field strengths and RF pulse powers. However due to the nonlinearity of the receiver SNR value starts to saturate at higher angles.

Rectangle pulse amplitude (RPA) effect on the receiver performance is also

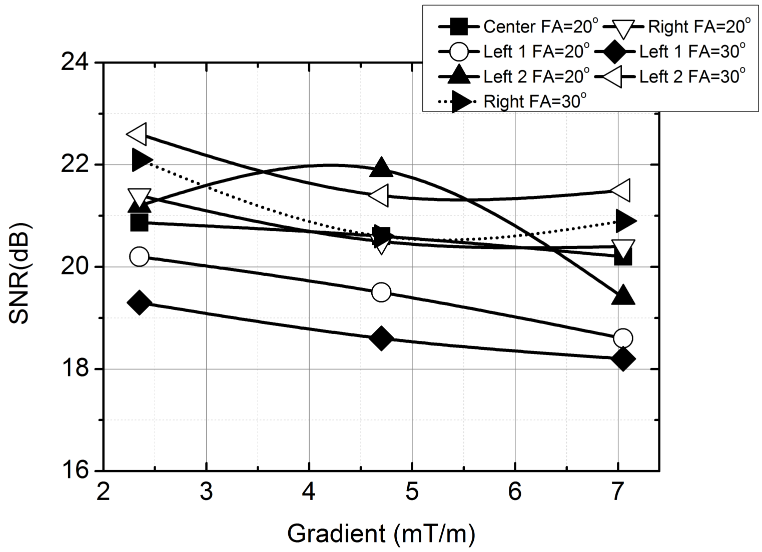

Figure 5.25. Measured SNR vs Gradient strength (G_x) relationship for the four locations at a various FA; RPA=2°, laser power is 60 mW and acquisition time is 1 ms for the experiment.

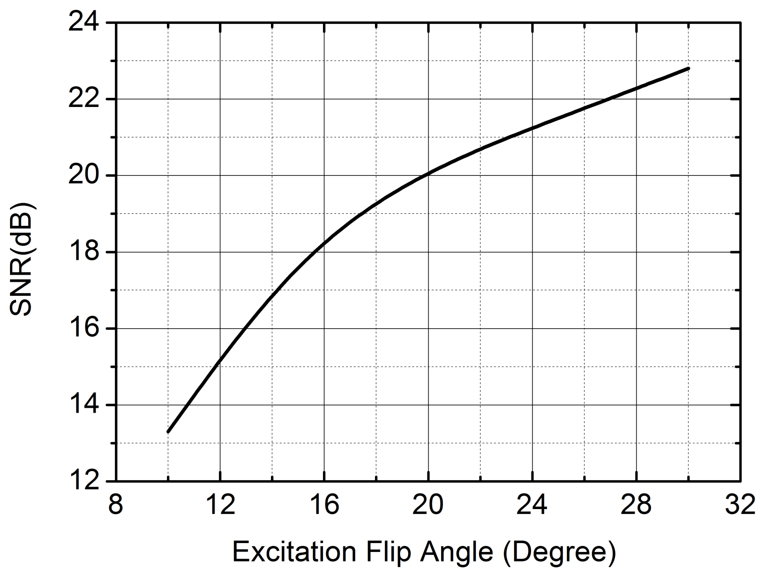

Figure 5.26. Measured SNR vs Flip angle (FA) relationship at *Center* location; RPA=2°, G_x=7.05 mT/m, laser power is 60 mW and acquisition time is 1 ms for the experiment.

tested. Figure 5.27 shows the measurement results for the *Center* location while FA=20°, G_x=7.05mT/m, laser power is 60 mW, and acquisition time is 1 ms. However measurement results are inconclusive about the effect of the rectangular pulse strength on SNR, it can be accepted that the mean of SNR value is constant across the different pulse powers. This is due to the fact that in order to the keep the homogeneity in the magnetic field, a weak non-selective rectangular pulse is chosen. Hence, the effect of the pulse strength is not clearly observable at this low power range.

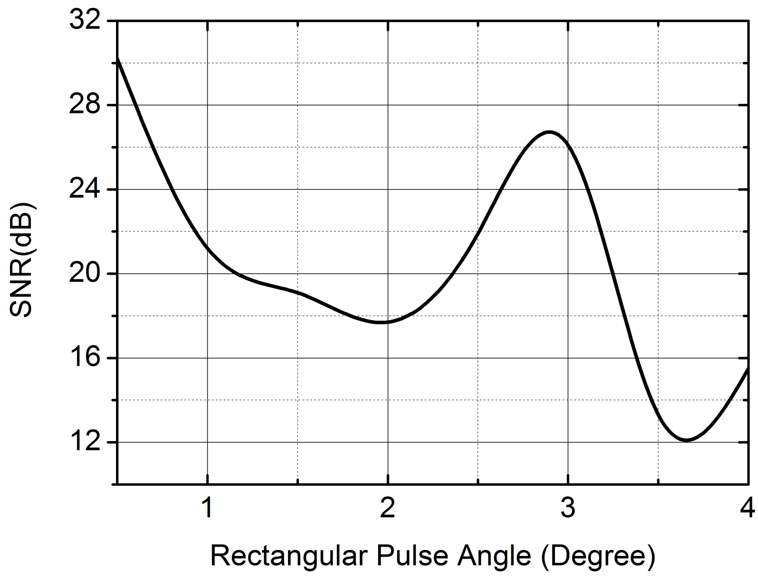

Figure 5.27. Measured SNR vs RPA (FA) relationship at *Center* location; FA=20°, G_x=7.05 mT/m, laser power is 60 mW and acquisition time is 1 ms for the experiment.

In the last bunch of experiments, the laser power is swept to detect the minimum optical power needed for a proper operation. In order to see this effect, repetition time (TR) is set to 50 ms to allow the intermittent operation. The acquisition time is kept at 1 ms, thus duty cycle of the modulation signal is set to 98% . Measured results are shown in Figure 5.28. FA=20°, RPA=0.5°, G_x=7.05 mT/m for the experiment. The results clearly confirms the experiments shown in Figure 5.17 which is carried out in the laboratory environment. The performance of the receiver starts to saturate at 40 mW of optical power. The system is also successfully operated at 10 mW of optical power, which is evidently important since low optical powers are desired to reduce the temperature of the tip.

5.2.3. Spatial Resolution of the System

The spatial resolution depends both on MRI parameters and the acquisition method used. Applied gradient field strength, relaxation times of the sample, the size

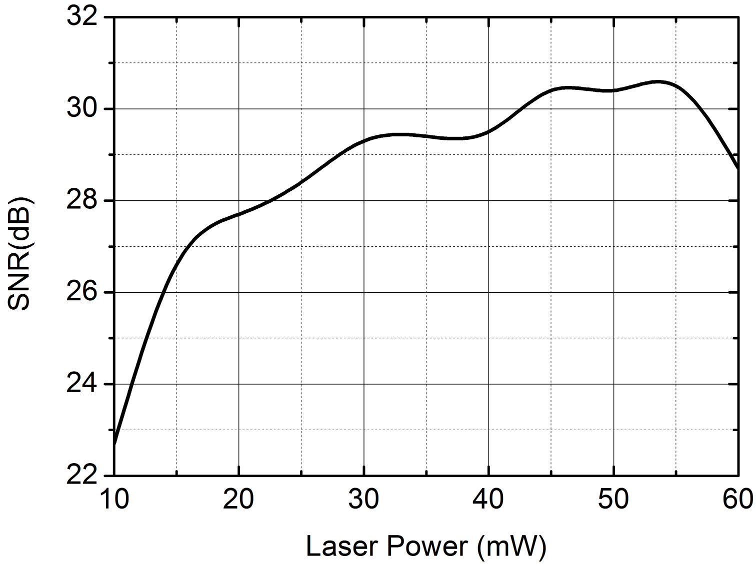

Figure 5.28. Measured SNR vs laser power relationship at *Center* location; FA=20°, RPA=0.5°, G_x=7.05 mT/m, acquisition time is 1 ms, and repetition time is 50 ms for the experiment.

of the coil, and acquisition time is most important parameters in determination of the spatial resolution [58].

Spatial resolution is directly limited by the frequency resolution. For a time domain signal that is acquired for a T time, the frequency resolution is simply $\Delta f = 1/T$. Any integer multiple of the frequency resolution is detectable. In our experiments, relatively a very short acquisition time of 1 ms is used, thus frequency resolution is said to be 1 kHz for the experiment. In the experiment, MRI frequency bandwidth per cm ($10^{-2}\gamma G_x$) is 3 kHz for applied G_x of 7.05 mT/m. As a result, the resolution is calculated to be 3mm for the experiment. This is a relatively high resolution value for the intravascular operations when we consider that the coil diameter is 2 mm. On the other hand, the frequency resolution can be increased without degrading the SNR with a zero-filling (zero padding) algorithm [12, 99, 100]. In this algorithm, data is filled with zeros to virtually increase the acquisition time. Since there is no signal or noise information in additional data, zero-filling has no effect on SNR [12]. The main impact of zero filling algorithm is that the computational time required to add zeros to the raw data which may increase the localization time. On the other hand, current computational systems can realize zero-filling algorithm in a very short amount of time that has no significant effect on the localization time. In the experiments, the acquisition time is increased to 100 ms with the zero-filling algorithm setting the spatial resolution limit to 30μm.

Obtaining the ideal resolution is not possible due to noise contributions of the receiver, finite length of the coil antenna, gradient strength, and relaxation times. The optimum resolution is proportional to the relaxation times as [58]

$$R_{i,opt} \propto \sqrt{\frac{(1+e^{-T_R/T_1})}{T_2^*(1-e^{-T_R/T_1})}}. \tag{5.4}$$

The resolution of the system can be calculated from the measurements by finding standard deviation of the frequency values taken at the same conditions. In [58], it is proposed that for a system that uses FID signals for localization, the spatial resolution is calculated as

$$R_i = \frac{R_{\nu 0}}{\gamma G_i}, \tag{5.5}$$

where R_i is the spatial resolution, $R_{\nu 0}$ is the resonance frequency resolution which is defined as $3\sigma_{\nu 0}$, and G_i is the applied gradient strength for i dimension. The factor three is introduced arbitrarily to take into consideration that noise fluctuations and resonance frequency shifts are indistinguishable. In order to extract a meaningful σ value, very high number of measurements (i.e > 100) have to be done, which is not the case for the experiments done with the proposed system. Nevertheless, it has been tried to make a broad approximation of the spatial resolution from 13 measurements taken at the *Center* position. G_x is set to 7.05 mT/m. 11 measurements are taken with and laser power of 60 mW. Two measurements taken with 40 mW and 50 mW are also added to the data to make a pessimistic prediction. σ is found to be 35 Hz, thus $R_{\nu 0}$=105 Hz. Using Equation 5.5, we can estimate a spatial resolution as 350 μm which is an acceptable value for interventional surgical operations.

It can be calculated that there is an optimum gradient strength for a particular coil diameter. This value can be used to obtain optimum spatial resolution. Optimum gradient strength can be approximated as

$$G_{i,opt} = \frac{8\pi}{\gamma \Delta i T_2^*}, \tag{5.6}$$

where Δi is the diameter of the coil. T_2^* value is highly variable for different tissues. However it can be accepted to be approximately 50 ms [101, 102]. Coil diameter Δi is 2 mm, thus optimum gradient strength $G_{i,op}$ is approximately 5.9 mT/m which corresponds to a resolution bandwidth (γG_i) of 2.5 kHz/cm.

6. CONCLUSIONS AND FUTURE WORK

6.1. Conclusions

A fully optical CMOS based localization system is designed, implemented, and tested in the MRI Environment successfully in the thesis. The implemented system is aimed to solve the RF induced heting problem that is present in conventional catheter localization systems. The implemented system composed is based on an integrated circuit that consists of a receiver and an optical power supply unit. Three generations of integrated circuits are designed in $0.18\mu m$ UMC triple well technology. The first generation is dedicated to the design of the optical power supply unit.

Before the design process, a series of experiments are carried out using discrete component based circuits. An LNA with a 0.4 dB noise figure and 58 dB forward gain is designed using discrete SIEGET transistors. A micro-coil antenna designed for a 7 Fr catheter is successfully localized in 1.5 T MRI environment. This tests provide the system specifications for the integrated receiver realization.

The implemented optical power supply unit is formed by a single on-chip photodiode and a DC-DC converter that can boost low voltage of a photodiode to voltages greater than 1.5 V. This unit is required since the receiver electronics require high voltage for high dynamic range. The unit is successfully tested for voltages down to 0.4 V showing the potential of it for further ultra low voltage applications. It has been also introduced that an intermittent operation in which the system is operated for a short period of time to gather higher dynamic range and noise performances. A storage capacitor acts as a batter that stores charge for this short period of time. Then, with through a optically driven switch, the accumulated charge on the capacitor is transferred to the electronics. This operation is novel in way that it is fully optical and the switch control is done through modulation of the applied light. A series of on-chip photodiodes are designed and implemented as a optical-to-electrical converter. The implemented designs provide efficiency calues upto 5% with currents higher than

15 mA. The photodiode and the DC-DC converter they can provide 800μW power that is more than sufficient for various wireless applications.

Various coupling methods are tested. A MEMS silicon micro mirror is fabricated using KOH etching process. The reflectivity of the mirror is increased by aluminum coating. A fiber optical cable is placed in the etched V-groove. The first generation integrated circuit, fiber optic cable and the MEMS platform is integrated on a probe station and this overall fiber coupled unit is successfully tested. Butt-coupling is also implemented by aligning fiber optic cables to the integrated circuit by micro-manipulators. The aligned fiber-optic cable is sealed in a Plexyglass cube by an epoxy adhesive. This integrated unit is also tested succesfully.

The second generation circuit is designed to investigate receiver architecture performance. A low-IF architecture is designed and implemented. The receiver is formed by a low noise amplifier, a voltage gain stage, a active loaded Gilbert-cell mixer, a one-pole RC filter and a simple laser driver. The receiver is operated in two different configurations; continuously and intermittently. In the continuous configuration, the receiver is shown to function properly while powered by a set of on-chip photodiodes. The receiver consumes 700 μW continuously. A better system performance is obtained in the intermittent mode. The forward gain of the circuit is improved 6 dB while the average power consumption is reduced to 214 μW. The receiver is shown to detect signals down to -80 dBm, which clearly proves an optically powered MRI localization system is possible.

With the light of the previous two generations, a third generation receiver is designed. The receiver is improved by additional IF gain stages. The overall receiver gain is increased to 120 dB. The output driver is also improved by re-designing it as a self-biasing suplly independent current source architecture. Overall receiver is operated in a self mixing architecture in which the input is squared. The system is butt-coupled to a fiber optical cabled. Overall system is tested in 3 T MRI environemnt successfully. Fully optical localizations are realized. The architecture is novel in two ways; (i) it is operated full optically that the power and the output transmission is done in optical means. (ii) The local oscillator signal required for the receiver is provided wirelessly from the MRI scanner by programming a custom pulse sequence. Several tests are carried out and it is shown that it is possible to localize micro-coils with optical powers as low as 10 mW. The overall system incorporates minimum amount of discrete components that permit a full system integration within a 7 Fr catheter. Spatial resolution for the experment is calculated as 350μm which shows the proposed system cane be used for catheter tracking in minimally invasive operations.

As a conclusion, the thesis is successfully finished by realizing a very compact localization system that provides a safe solution for catheter localization procedures performed in the MRI environment.

6.2. Future Work

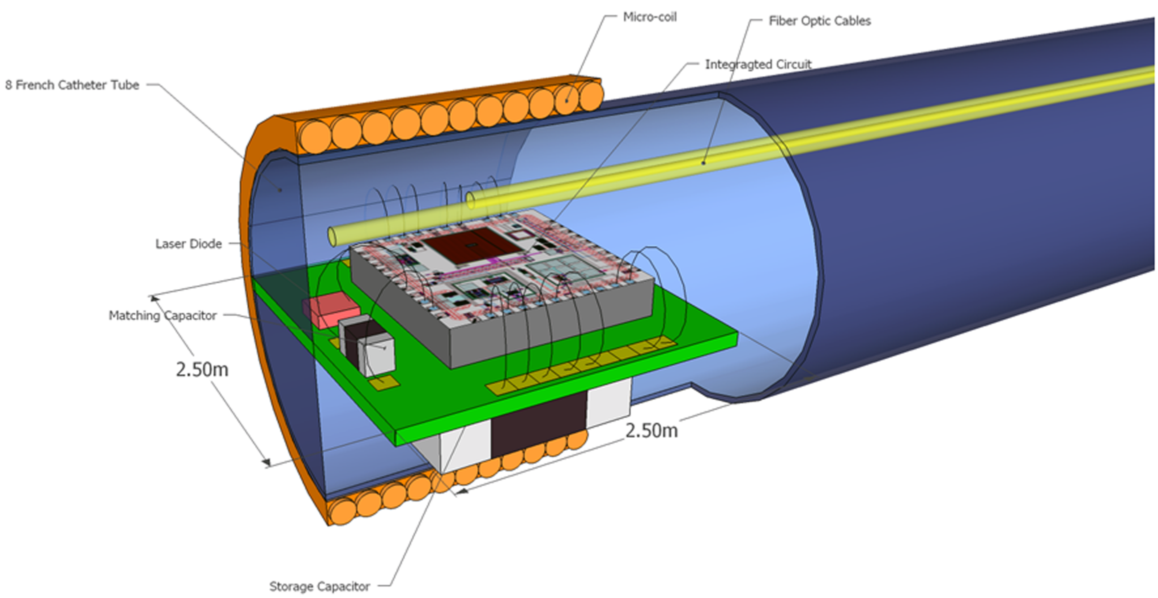

Figure 6.1. The overall system blocks depicted in a 7 Fr catheter.

The most important future work is full integration of the system with a catheter. The system is designed with only three external components. One of which is a resistor to create a discharge path for the photodiode. This resistor in future implementations can be realized on-chip. However, even with this resistor the system can fit into a 7 Fr catheter with its current configuration. The other two components are a storage capacitor and the light emitting diode. A fourth capacitor for antenna matching may require but this capacitor can easily be implmented on-chip since its value will be in pico farads range if we consider a nano henry range coil antenna for a 3 T implementation. These components do not cover a large area. The full integration of the system with the extra components and coil antenna is shown in Figure 6.1. The sizes are one-to-one in the figure. The figure clearly shows the possibility of this integration. A micro mirror will be added to reflect to light onto the chip.

A second possible improvement over this system is designing a optical power supply unit that can provide a continuous power to the system. This implementation will clearly improve spatial resolution since the MR signal detection time will increase and hence the frequency resolution will increase. In order to achieve this, different DC-DC converter architecture can be designed with higher stage capacitances. The photodiode can also be implmented underneath the capacitors to increase the current value.

Lastly, a fully automatic localization pulse sequence can be programmed for the system. In this way, system can set its parameters such as applied optical power, intermittent signal period, and acquisition time.

APPENDIX A: MRI PULSE SEQUENCE

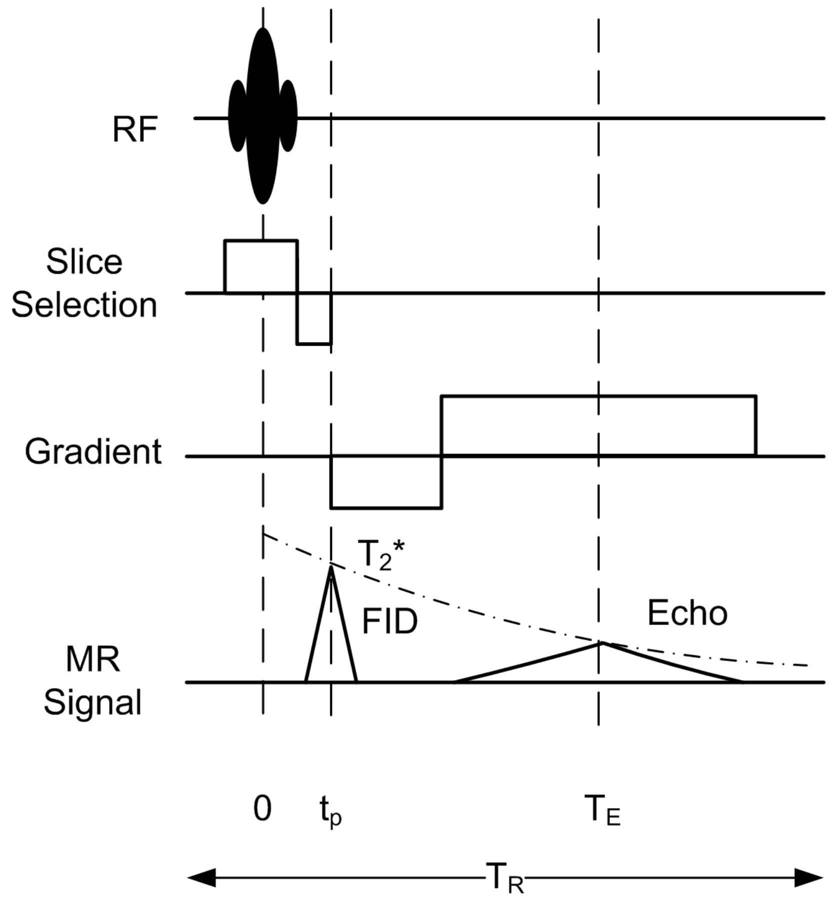

Figure A.1. An example gradient echo MRI pulse sequence.

In order to create images from the spins, a set of RF excitation pulses and gradients have to applied in a sequential manner. This sequence is called an MRI pulse sequence and there are vast number of pulse sequences available for different purposes [12]. An example gradient echo pulse sequence is shown in Figure A.1. Here, a selective RF excitation pulse is applied to the sample. During this time, the slice is selected by a slice selection gradient. Please note that the localization operation does not require slice selection. The volume is excited entirely to permit an out-of-slice localization. After the slice selection a dephasing frequency encoding gradient is applied to generate an echo signal. The duration between, the time of the maximum peak of the RF excitation pulse and the time of maximum peak of echo signal is denoted Echo Time or T_E, while the overall operational time is called Repetition Time or T_R. These two parameters can be changed to obtain optimum image for a specific tissue.

The other important parameter in the sequence is the field-of-view or FOV. FOV represents the area (mm^2) of the imaged slice. FOV is usually taken as to be in square ratios. FOV value for a frequency encoding can be calculated as

$$FOV = \frac{f_s}{\gamma G}, \tag{A.1}$$

where f_s is the sampling rate of data acquisition of the MR signal.

APPENDIX B: LAYOUTS OF THE INTEGRATED CIRCUITS

B.1. First Generation Integrated Circuit

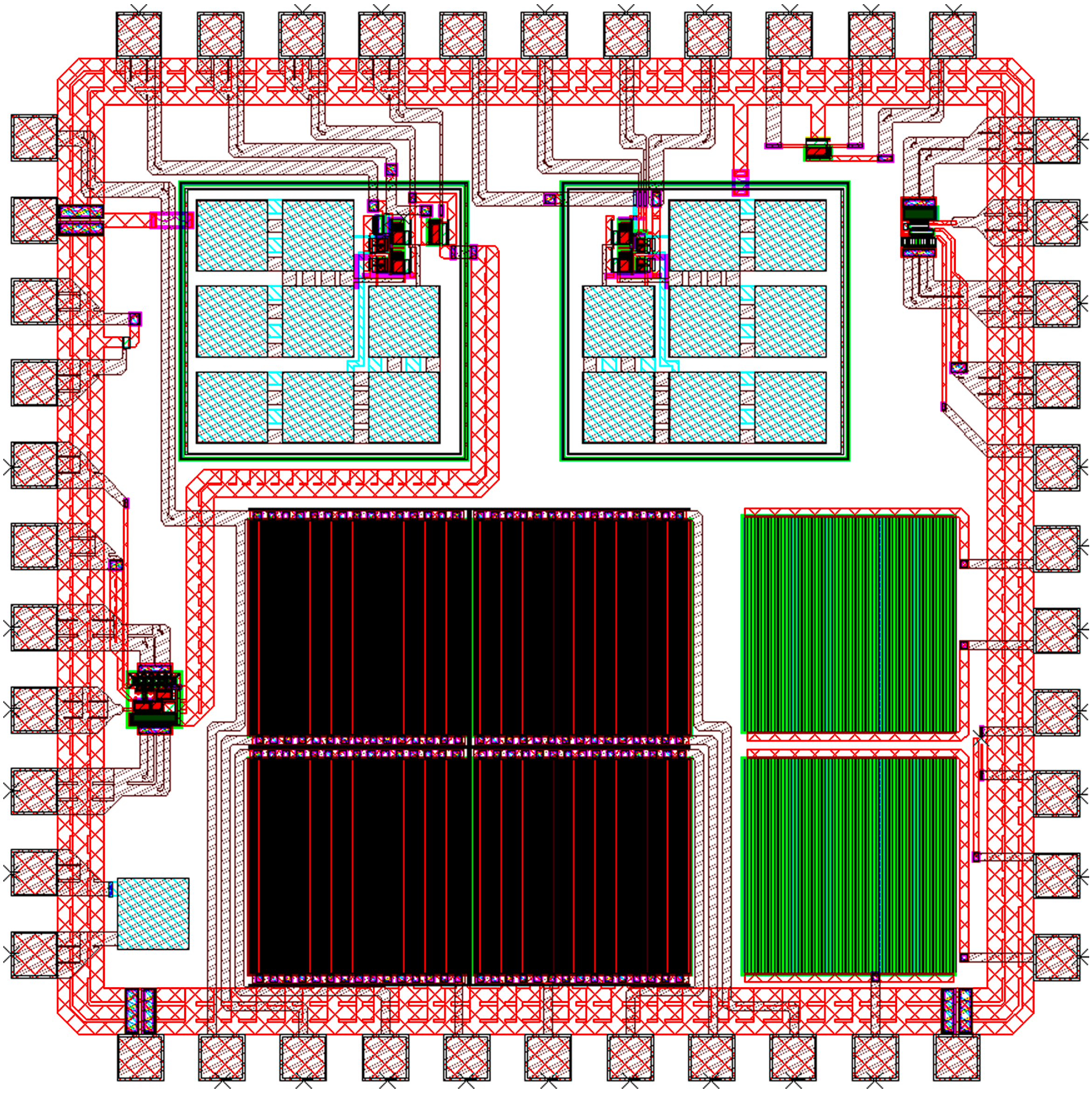

Figure B.1. Layout of the first generation IC.

B.2. Second Generation Integrated Circuit

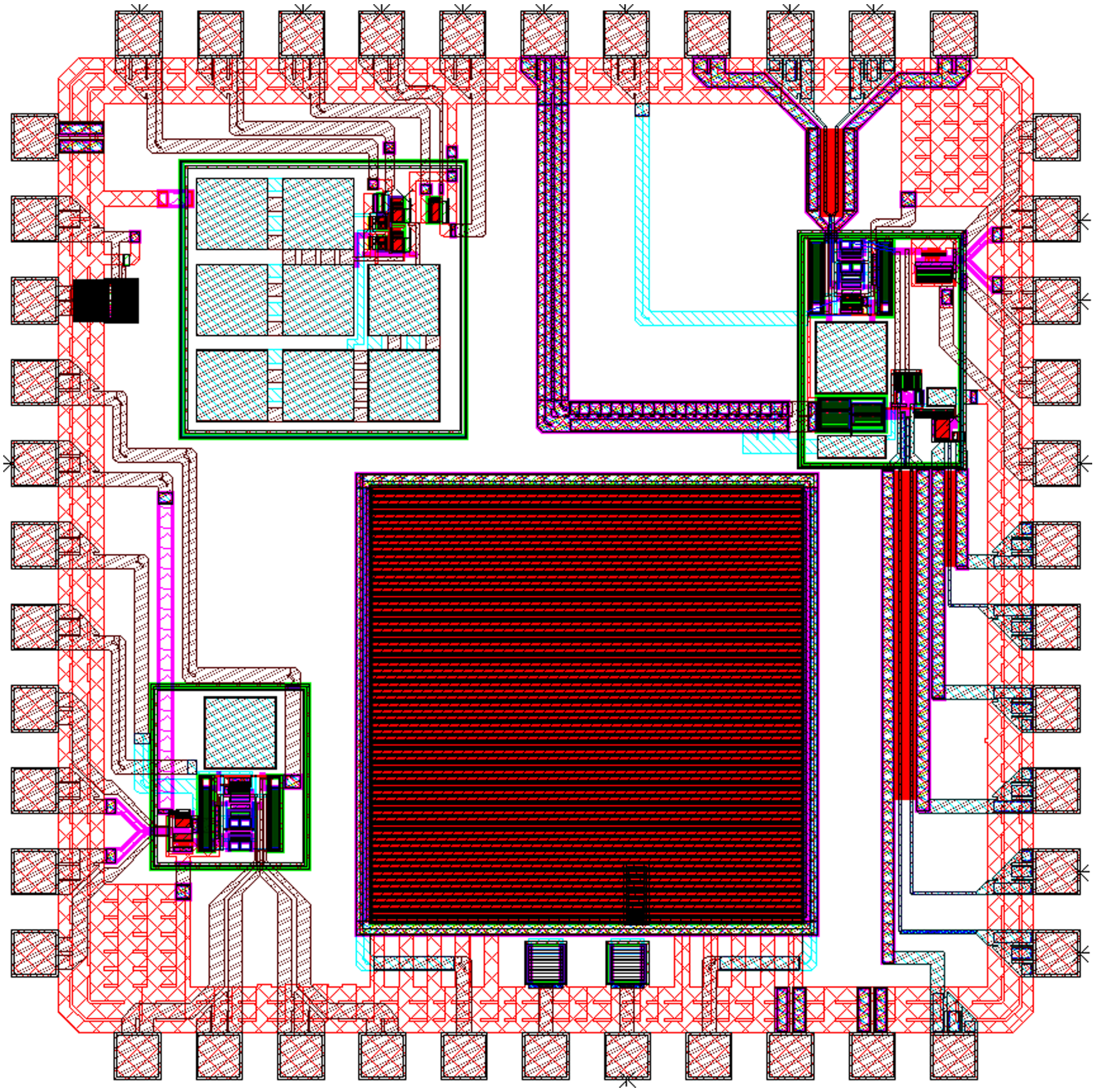

Figure B.2. The layout of the second generation IC.

B.3. Third Generation Integrated Circuit

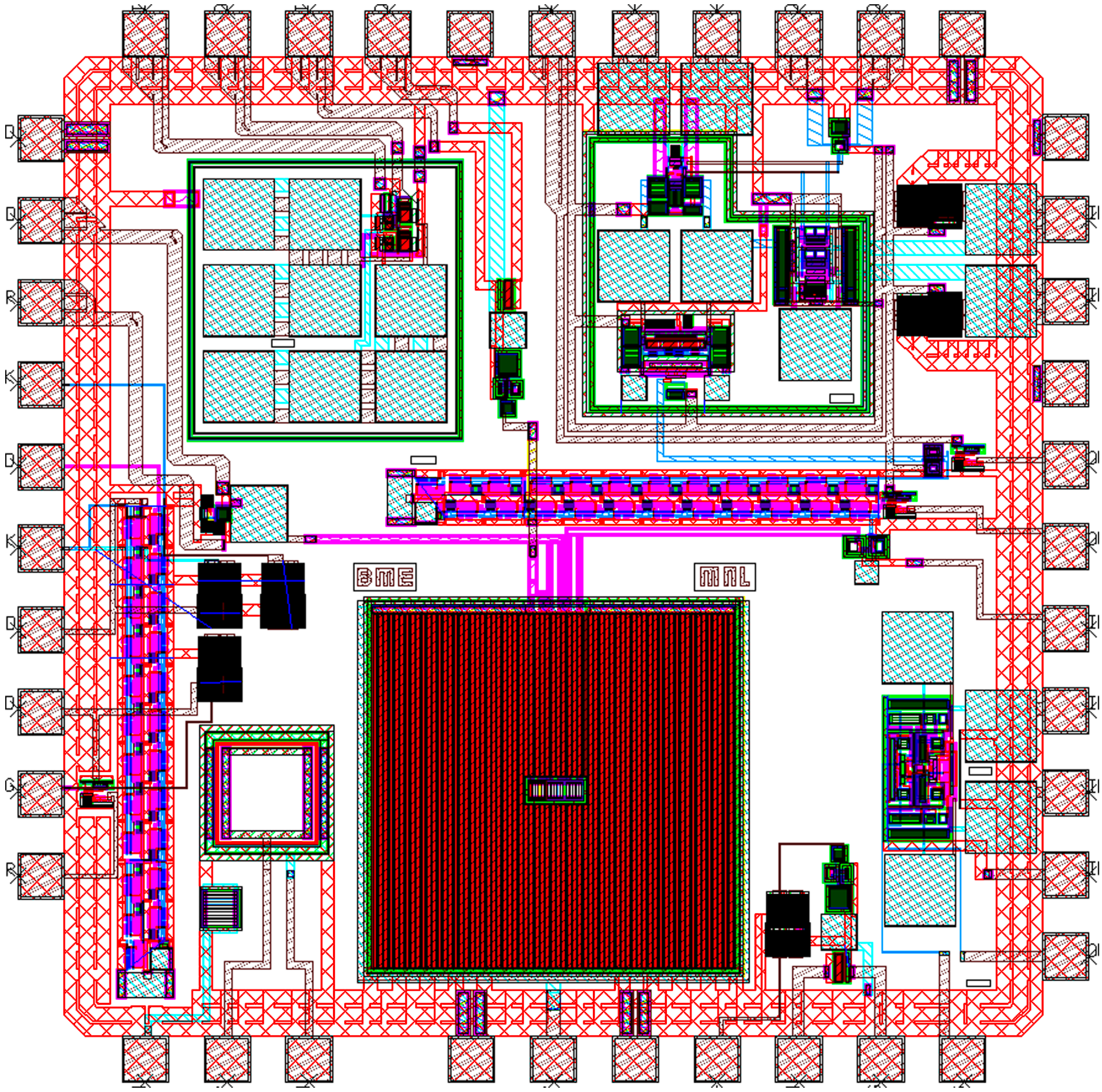

Figure B.3. Layout of the third generation IC.

REFERENCES

1. Smith, A. S., *Quantitative MRI in Cancer*, chap. Physics of MRI, pp. 17–26, Taylor&Francis, Boca Raton, 2011.

2. Miquel, M. E., S. Hegde, V. Muthurangu, B. J. Corcoran, S. F. Keevil, D. L. G. Hill and R. S. Razavi, "Visualization and Tracking of an Inflatable Balloon Catheter Using SSFP in a Flow Phantom and in the Heart and Great Vessels of Patients", *Magnetic Resonance in Medicine*, Vol. 51, No. 5, pp. 988–995, 2004.

3. Unal, O., J. Li, W. Cheng, H. Yu and C. M. Strother, "MR-Visible Coatings for Endovascular Device Visualization", *Journal of Magnetic Resonance Imaging*, Vol. 23, No. 5, pp. 763–769, 2006.

4. Fink, C., M. Bock, R. Umathum, S. Volz, S. Zuehlsdorff, R. Grobholz, H. U. Kauczor and P. Hallscheidt, "Renal Embolization: Feasibility of Magnetic Resonance-guidance Using Active Catheter Tracking and Intraarterial Magnetic Resonance Angiography.", *Investigative Radiology*, Vol. 39, No. 2, pp. 111–119, 2004.

5. Quick, H. H., H. Kuehl, G. Kaiser, S. Bosk, J. F. Debatin and M. E. Ladd, "Inductively Coupled Stent Antennas in MRI", *Magnetic Resonance in Medicine*, Vol. 48, No. 5, pp. 781–790, 2002.

6. Langford-Smith, F., *Radio Designer's Handbook*, Elsevier, Charlottesville, 1997.

7. Palik, E. D., *Handbook of Optical Constants of Solids*, Elsevier Science, San Diego, 1998.

8. Radovanovič, S., A. J. Annema and B. Nauta, *High-Speed Photodiodes in Standard CMOS Technology*, Springer, Heidelberg, 2006.

9. Vlaardingerbroek, M. T. and J. A. den Boer, *Magnetic Resonance Imaging : Theory and Practice*, Springer, Heidelberg, 2003.

10. Webster, J. G., *Minimally Invasive Medical Technology*, Taylor&Francis, Boca Raton, 2010.

11. Placidi, G., *MRI: Essentials for Innovative Technologies*, Taylor & Francis, Boca Raton, 2012.

12. Bernstein, M. A., K. F. King and X. J. Zhou, *Handbook of MRI Pulse Sequences*, Elsevier Science, San Diego, 2004.

13. Iserson, K. V., "J.-F.-B. Charrière: The man behind the 'French' gauge", *Journal of Emergency Medicine*, Vol. 5, No. 6, pp. 545–548, 1987.

14. Kleinerman, R. S., "Cancer Risks Following Diagnostic and Therapeutic Radiation Exposure in Children", *Pediatric Radiology*, Vol. 36, pp. 121–125, 2006.

15. Andreassi, M., L. Ait-Ali, N. Botto, S. Manfredi, G. Mottola and E. Picano, "Cardiac cCatheterization and Long-Term Chromosomal Damage in Children with Congenital Heart Disease.", *European Heart Journal*, Vol. 27, pp. 121–125, 2006.

16. Rubin, D. L., A. V. Ratner and S. W. Young, "Magnetic Susceptibility Effects and Their Application in the Development of New Ferromagnetic Catheters for mMagnetic Resonance Imaging", *Investigative Radiology*, Vol. 25, No. 12, pp. 1325–1332, 1990.

17. Unal, O., F. R. Korosec, R. Frayne, C. M. Strother and C. A. Mistretta, "A Rapid 2D Time-Resolved Variable-Rate K-Space Sampling MR Technique for Passive Catheter Tracking During Endovascular Procedures", *Magnetic Resonance in Medicine*, Vol. 40, No. 3, pp. 356–362, 1998.

18. Bakker, C. J., R. M. Hoogeveen, J. Weber, J. J. van Vaals, M. A. Viergever and W. P. Mali, "Visualization of Dedicated Catheters Using Fast Scanning Techniques with Potential for MR-guided Vascular Interventions.", *Magnetic Resonance in Medicine*, Vol. 36, No. 6, pp. 816–820, 1996.

19. Glowinski, A., J. Kursch, G. Adam, A. Bucker, T. Noll and R. W. Gunther, "Device Visualization for Interventional MRI Using Local Magnetic Fields: Basic Theory and Its Application to Catheter Visualization", *IEEE Transactions on Medical Imaging*, Vol. 17, No. 5, pp. 786–793, 1998.

20. Eggers, H., S. Weiss, P. Boernert and P. Boesiger, "Image-Based Tracking of Optically Detunable Parallel Resonant Circuits", *Magnetic Resonance in Medicine*, Vol. 49, No. 6, pp. 1163–1174, 2003.

21. Hofmann, L. V., R. P. Liddell, J. Eng, B. A. Wasserman, A. Arepally, D. S. Lee and D. A. Bluemke, "Human Peripheral Arteries: Feasibility of Transvenous Intravascular MR Imaging of the Arterial Wall", *Radiology*, Vol. 235, No. 2, pp. 617–622, 2005.

22. Wacker, F. K., D. Elgort, C. M. Hillenbrand, J. L. Duerk and J. S. Lewin, "The Catheter-Driven MRI Scanner: A New Approach to Intravascular Catheter Tracking and Imaging-Parameter Adjustment for Interventional MRI", *American Journal of Roentgenology*, Vol. 183, No. 2, pp. 391–395, 2004.

23. Shellock, F. G., "Radiofrequency Energy-Induced Heating During MR Procedures: A Review", *Journal of Magnetic Resonance Imaging*, Vol. 12, No. 1, pp. 30–36, 2000.

24. Yeung, C. J., R. C. Susil and E. Atalar, "RF Safety of Wires in Interventional MRI: Using a Safety Index", *Magnetic Resonance in Medicine*, Vol. 47, No. 1, pp. 187–193, 2002.

25. Konings, M. K., L. W. Bartels, H. F. M. Smits and C. J. G. Bakker, "Heating

Around Intravascular Guidewires by Resonating RF Waves", *Journal of Magnetic Resonance Imaging*, Vol. 12, No. 1, pp. 79–85, 2000.

26. Ladd, M. E. and H. H. Quick, "Reduction of Resonant RF Heating in Intravascular Catheters Using Coaxial Chokes", *Magnetic Resonance in Medicine*, Vol. 43, No. 4, pp. 615–619, 2000.

27. Woodward, T. K. and A. V. Krishnamoorthy, "1-Gb/s Integrated Optical Detectors and Receivers in Commercial CMOS Technologies", *IEEE Journal of Selected Topics in Quantum Electronics*, Vol. 5, No. 2, pp. 146–156, 1999.

28. Razavi, B., "Prospects of CMOS Technology for High-Speed Optical Communication Circuits", *IEEE Journal of Solid-State Circuits*, Vol. 37, No. 9, pp. 1135–1145, 2002.

29. Memis, O. G., Y. Eryaman, O. Aytur and E. Atalar, "Miniaturized Fiber-Optic Transmission System for MRI Signals", *Magnetic Resonance in Medicine*, Vol. 59, No. 1, pp. 165–173, 2008.

30. Guilar, N. J., T. J. Kleeburg, A. Chen, D. R. Yankelevich and R. Amirtharajah, "Integrated Solar Energy Harvesting and Storage", *IEEE Transactions on Very Large Scale Integration (VLSI) Systems*, Vol. 17, No. 5, pp. 627–637, 2009.

31. Ammar, A., S. Mesut, D. S. Freedman, E. Cevik, P. S. Spuhler and M. S. Unlu, "Floating Light-Activated Microelectrical Stimulators Tested in the Rat Spinal Cord", *Journal of Neural Engineering*, Vol. 8, No. 5, p. 056012, 2011.

32. Schanze, T., L. Hesse, C. Lau, N. Greve, W. Haberer, S. Kammer, T. Doerge, A. Rentzos and T. Stieglitz, "An Optically Powered Single-Channel Stimulation Implant as Test System for Chronic Biocompatibility and Biostability of Miniaturized Retinal Vision Prostheses", *Biomedical Engineering, IEEE Transactions on*, Vol. 54, No. 6, pp. 983–992, 2007.

33. Haque, R. M. and K. D. Wise, “A 3D Implantable Microsystem for Intraocular Pressure Monitoring Using a Glass-in-Silicon Reflow Process”, *IEEE International Conference on Micro Electro Mechanical Systems*, pp. 995–998, 2011.

34. Shellock, F. G., “Biomedical Implants and Devices: Assessment of Magnetic Field Interactions with a 3.0-Tesla MR system”, *Journal of Magnetic Resonance Imaging*, Vol. 16, No. 6, pp. 721–732, 2002.

35. Fandrey, S., S. Weiss and J. Muller, “A Novel Active MR Probe using a Miniaturized Optical Link for a 1.5-T MRI scanner”, *Magnetic Resonance in Medicine*, Vol. 67, No. 1, pp. 148–155, 2012.

36. Ayazian, S., V. A. Akhavan, E. Soenen and A. Hassibi, “A Photovoltaic-Driven and Energy-Autonomous CMOS Implantable Sensor”, *IEEE Transactions on Biomedical Circuits and Systems*, Vol. PP, No. 99, p. 1, 2012.

37. Brett, A. W., M. D. Scott, B. S. Leibowitz, L. Zhou, C. L. Bellew, J. A. Chediak, J. M. Kahn, B. E. Boser and K. S. J. Pister, “An Autonomous 16mm 3 Solar-Powered Node for Distributed Wireless Sensor Networks”, *IEEE International Conference on Sensors*, pp. 1510–1515, 2002.

38. O’brien, D., J. Liu, G. Faulkner, S. Sivathasan, W. Yuan, S. Collins, S. Elston and V. Pithamiron, “Design and Implementation of Optical Wireless Communications with Optically Powered Smart Dust Motes”, *IEEE Journal on Selected Areas in Communications*, Vol. 27, No. 9, pp. 1646–1653, 2009.

39. Marwick, M. A. and A. Andreou, “Photo-Battery Fabricated in Silicon on Sapphire CMOS”, *Electronics Letters*, Vol. 44, No. 12, pp. 766–767, 5 2008.

40. Kitamura, K., S. Sasak, Y. Matsuya and T. Douseki, “Optical Wireless Digital-Sound Transmission System with 1-Bit $\Delta\ \Sigma$-Modulated Visible Light and Spherical Si Solar Cells”, *IEEE Sensors Journal*, Vol. 10, No. 11, pp. 1753–1758,

2010.

41. Aktan, O., B. Sarioglu, U. Cindemir, S. O. Unlu, G. Dundar, S. Mutlu and A. D. Yalcinkaya, "Optoelectronic CMOS Power Supply Unit for Electrically Isolated Microscale Applications", *IEEE Journal of Selected Topics in Quantum Electronics*, Vol. 17, No. 3, pp. 747–756, 2011.

42. Sarioglu, B., O. Aktan, A. Oncu, S. Mutlu, G. Dundar and A. D. Yalcinkaya, "An Optically Powered CMOS Receiver System for Intravascular Magnetic Resonance Applications", *IEEE Journal on Emerging and Selected Topics in Circuits and Systems*, Vol. 2, No. 4, pp. 683–691, 2012.

43. Sarioglu, B., O. Aktan, U. Cindemir, S. Mutlu, G. Dundar and A. D. Yalcinkaya, "An RF Front-End with Optically Powered CMOS Power Supply", *International Conference on Optical MEMS and Nanophotonics*, pp. 193–194, Istanbul, 2011.

44. Sarioglu, B., O. Aktan, U. Cindemir, G. Dundar, C. Ozturk, S. Mutlu and A. D. Yalcinkaya, "Optoelectronic CMOS Power Supply Unit for Interventional MRI Devices", *Proceedings of International Society for Magnetic Resonance in Medicine Conference*, Montreal, 7-13 2011.

45. Aktan, O., B. Sarioglu, U. Cindemir, G. Dundar, S. Mutlu and A. D. Yalcinkaya, "Compact CMOS Optoelectronic Power Supply Unit", *12th National Optics, Electro-Optics and Photonics Meeting*, Istanbul, 8 2010.

46. Sarioglu, B., O. Aktan, U. Cindemir, G. Dundar, S. Mutlu, C. Oztürk and A. D. Yalcinkaya, "Optoelektronik Güç Kaynağı ile Beslenen RF Ön-Uç Devresi Gerçeklenmesi", *13rd National Optics, Electro-Optics and Photonics Meeting*, Istanbul, 14 2012.

47. Sarioglu, B., B. Camli, A. U. Cakaci, S. Mutlu, G. Dundar and A. D. Yalcinkaya, "MEMS Miktoayna ile Tümleşik MRG Alıcı Mikrosistem Tasarımı", *14th National Optics, Electro-Optics and Photonics Meeting*, Istanbul, 8 2012.

48. Enz, C. C. and E. A. Vittoz, *CMOS Low-power Analog Circuit Design*, IEEE Service Center, 1996.

49. Davis, C. C., *Lasers and Electro-optics: Fundamentals and Engineering*, Cambridge University Press, Cambridge, 1996.

50. Schubert, E. F., *Light-Emitting Diodes*, Cambridge University Press, Cambridge, 2006.

51. Held, G., *Introduction to Light Emitting Diode Technology and Applications*, CRC Press, Boca Raton, 2009.

52. Sullivan, P., S. Schumann, R. D. Campo, T. Howells, A. Duraud, M. Shipman, R. A. Hatton and T. S. Jones, "Ultra-High Voltage Multijunction Organic Solar Cells for Low-Power Electronic Applications", *Advanced Energy Materials*, Vol. 3, No. 2, pp. 239–244, 2013.

53. Ishii, A. and T. Miyasaka, "A High Voltage Organic-Inorganic Hybrid Photovoltaic Cell Sensitized with Metal-Ligand Interfacial Complexes", *Chem. Commun.*, Vol. 48, pp. 9900–9902, 2012.

54. Fandrey, S., S. Weiss and J. Muller, "Development of an Active Intravascular MR Device with an Optical Transmission System", *IEEE Transactions on Medical Imaging*, Vol. 27, No. 12, pp. 1723–1727, 2008.

55. Anderson, K. J. T., G. C. Scott and G. A. Wright, "Catheter Tracking with Phase Information in a Magnetic Resonance Scanner", *IEEE Transactions on Medical Imaging*, Vol. 31, No. 6, pp. 1173–1180, 2012.

56. Robins, W. P., *Phase Noise in Signal Sources: Theory and Applications*, P. Peregrinus, London, 1984.

57. Hajimiri, A. and T. H. Lee, "A General Theory of Phase Noise in Electrical

Oscillators", *IEEE Journal of Solid-State Circuits*, Vol. 33, No. 2, pp. 179–194, 1998.

58. Anders, J., P. SanGiorgio, X. Deligianni, F. Santini, K. Scheffler and G. Boero, "Integrated Active Tracking Detector for MRI-guided Interventions", *Magnetic Resonance in Medicine*, Vol. 67, No. 1, pp. 290–296, 2012.

59. Pozar, D. M., *Microwave and RF Wireless Systems*, Wiley, New York, 2000.

60. Crols, J. and M. S. J. Steyaert, "Low-IF Topologies for High-Performance Analog Front Ends of Fully Integrated Receivers", *IEEE Transactions on Circuits and Systems II: Analog and Digital Signal Processing*, Vol. 45, No. 3, pp. 269–282, 1998.

61. Ellinger, F., *Radio Frequency Integrated Circuits and Technologies*, Springer, Heidelberg, 2008.

62. Silva, G. J., A. Datta and S. P. Bhattacharyya, *Pid Controllers for Timedelay Systems*, Birkhäuser, Berlin, 2005.

63. Sangster, F. L. J. and K. Teer, "Bucket-Brigade Electronics: New Possibilities for Delay, Time-Axis Conversion and Scanning", *IEEE Journal of Solid-State Circuits*, Vol. 4, No. 3, pp. 131–136, 1969.

64. Bult, K. and H. Wallinga, "A CMOS Analog Continuous-Time Delay Line with Adaptive Delay-Time Control", *IEEE Journal of Solid-State Circuits*, Vol. 23, No. 3, pp. 759–766, 1988.

65. Razavi, B., "Design Considerations for Direct-Conversion Receivers", *IEEE Transactions on Circuits and Systems II: Analog and Digital Signal Processing*, Vol. 44, No. 6, pp. 428–435, 1997.

66. Crols, J. and M. S. J. Steyaert, "A Single-Chip 900 MHz CMOS Receiver

Front-End with a High Performance Low-IF Topology", *IEEE Journal of Solid-State Circuits*, Vol. 30, No. 12, pp. 1483–1492, 1995.

67. Zhang, Q., M. Wendt, A. J. Aschoff, L. Zheng, J. S. Lewin and J. L. Duerk, "Active MR Guidance of Interventional Devices with Target-Navigation", *Magnetic Resonance in Medicine*, Vol. 44, No. 1, pp. 56–65, 2000.

68. Zhang, Q., M. Wendt, A. J. Aschoff, J. Andrik, J. S. Lewin and J. L. Duerk, "A Multielement RF Coil for MRI Guidance of Interventional Devices", *Journal of Magnetic Resonance Imaging*, Vol. 14, No. 1, pp. 56–62, 2001.

69. Hillenbrand, C. M., J. A. Jesberger, E. Y. Wong, S. Zhang, D. T. Chang, F. K. Wacker, J. S. Lewin and J. L. Duerk, "Toward Rapid High Resolution in Vivo Intravascular MRI: Evaluation of Vessel Wall Conspicuity in a Porcine Model Using Multiple Imaging Protocols", *Journal of Magnetic Resonance Imaging*, Vol. 23, No. 2, pp. 135–144, 2006.

70. Peck, T. L., R. L. Magin and P. C. Lauterbur, "Design and Analysis of Microcoils for NMR Microscopy", *Journal of Magnetic Resonance, Series B*, Vol. 108, No. 2, pp. 135–144, 1995.

71. Berry, L., L. Renaud, P. Kleimann, P. Morin, M. Armenean and H. Saint-Jalmes, "Development of Implantable Detection Microcoils for Minimally Invasive NMR Spectroscopy", *Sensors and Actuators A: Physical*, Vol. 93, No. 3, pp. 214–218, 2001.

72. Minard, K. R. and R. A. Wind, "Solenoidal Microcoil Design—Part II: Optimizing Winding Parameters for Maximum Signal-to-Noise Performance", *Concepts in Magnetic Resonance*, Vol. 13, No. 3, pp. 190–210, 2001.

73. Webb, A. G., "Radiofrequency Microcoils for Magnetic Resonance Imaging and Spectroscopy", *Journal of Magnetic Resonance*, 2012.

74. Minard, K. R. and R. A. Wind, “Solenoidal Microcoil Design. Part I: Optimizing RF Homogeneity and Coil Dimensions”, *Concepts in Magnetic Resonance*, Vol. 13, No. 2, pp. 128–142, 2001.

75. Massin, C., G. Boero, F. Vincent, J. Abenhaim, P. A. Besse and R. S. Popovic, “High-Q Factor RF Planar Microcoils for Micro-Scale NMR Spectroscopy”, *Sensors and Actuators A: Physical*, Vol. 97–98, No. 0, pp. 280–288, 2002.

76. Massin, C., C. Azevedo, N. Beckmann, P. A. Besse and R. S. Popovic, “Magnetic Resonance Imaging Using Microfabricated Planar Coils”, *IEEE-EMB Special Topic Conference on Microtechnologies in Medicine & Biology*, pp. 199–204, 2002.

77. Gray, P. R., P. J. Hurst, R. G. Meyer and S. H. Lewis, *Analysis and Design of Analog Integrated Circuits*, John Wiley & Sons, New York, 2008.

78. Ludwig, R. and P. Bretchko, *RF Circuit Design: Theory and Applications*, Prentice-Hall, New Jersey, 2000.

79. Bahl, I., *Fundamentals of RF and Microwave Transistor Amplifiers*, Wiley, New York, 2009.

80. Suster, M., W. H. Ko and D. J. Young, “An Optically Powered Wireless Telemetry Module for High-Temperature MEMS Sensing and Communication”, *Microelectromechanical Systems, Journal of*, Vol. 13, No. 3, pp. 536–541, 2004.

81. Aktan, O., *The Design Aspects of an Optically Powered CMOS Receiver Front-End for Electrically Isolated Applications*, Ph. D. Thesis, Bogazici University, 2011.

82. Ferri, M., D. Pinna, E. Dallago and P. Malcovati, “Integrated Micro Solar Cell Structures for Harvesting Supplied Microsystems in 0.35μm CMOS Technology”, *Sensors, 2009 IEEE*, pp. 542–545, 2009.

83. Fang, X., K. S. Hsiao, V. P. Chodavarapu, A. H. Titus and A. N. Cartwright, "Colorimetric Porous Photonic Bandgap Sensors with Integrated CMOS Color Detectors", *Sensors Journal, IEEE*, Vol. 6, No. 3, pp. 661–667, 2006.

84. Feruglio, S., F. Haned, G. Vasilescu, M. B. Chouikha, G. Sou, V. F. Hanna and G. Alquie, "A General Model of the CMOS Buried Double Junction Photodetector", *IEEE International Workshop on Imaging Systems and Techniques*, pp. 60–65, 2004.

85. Xu, W., D. L. Mathine and J. K. Barton, "High-Gain Differential CMOS Transimpedance Amplifier with On-Chip Buried Double Junction Photodiode", *Electronics Letters*, Vol. 42, No. 14, pp. 803–805, 2006.

86. Yang, F. and A. H. Titus, "Integrated Colour Detectors in 0.18 μm CMOS Technology", *Electronics Letters*, Vol. 43, No. 23, 2007.

87. Law, M. K. and A. Bermak, "High-Voltage Generation with Stacked Photodiodes in Standard CMOS Process", *Electron Device Letters, IEEE*, Vol. 31, No. 12, pp. 1425–1427, 2010.

88. Liu, J., G. E. Faulkner, S. Collins, D. C. O'Brien and S. J. Elston, "An Optically Powered, Free Space Optical Communications Receiver", *IEEE International Symposium on Circuits and Systems*, pp. 197–200, 2008.

89. Pelliconi, R., D. Iezzi, A. Baroni, M. Pasotti and P. Rolandi, "Power Efficient Charge Pump in Deep Submicron Standard CMOS Technology", *IEEE Journal of Solid-State Circuits*, Vol. 38, No. 6, pp. 1068–1071, 2003.

90. Baderna, D., A. Cabrini, M. Pasotti and G. Torelli, "Power Efficiency Evaluation in Dickson and Voltage Doubler Charge Pump Topologies", *Microelectronics Journal*, Vol. 37, No. 10, pp. 1128–1135, 2006.

91. Palumbo, G., D. Pappalardo and M. Gaibotti, "Charge Pump Circuits: Power

Consumption Optimization", *Circuits and Systems I: Fundamental Theory and Applications, IEEE Transactions on*, Vol. 49, No. 11, pp. 1535–1542, 2002.

92. Sadler, D., M. J. Garter, C. H. Ahn, S. Koh and A. L. Cook, "Optical Reflectivity of Micromachined 111-Oriented Silicon Mirrors for Optical Input-Output Couplers", *Journal of Micromechanics and Microengineering*, Vol. 7, No. 4, p. 263, 1997.

93. Sun, N., Y. Liu, H. Lee, R. Weissleder and D. Ham, "CMOS RF Biosensor Utilizing Nuclear Magnetic Resonance", *IEEE Journal of Solid-State Circuits*, Vol. 44, No. 5, pp. 1629–1643, 2009.

94. Sansen, W. M. C., *Analog Design Essentials*, Springer, Heidelberg, 2006.

95. andB. A. Xavier, P. J. S. and W. H. Ku, "Low Voltage Performance of a Microwave CMOS Gilbert Cell Mixer", *IEEE Journal of Solid-State Circuits*, Vol. 32, No. 7, pp. 1151–1155, 1997.

96. Zivojinovic, P., M. Lescure and H. T. Beteille, "Design and Stability Analysis of a CMOS Feedback Laser Driver", *IEEE Transactions on Instrumentation and Measurement*, Vol. 53, No. 1, pp. 102–108, 2004.

97. Tümer, M., *Design of a Tracking System for MRI Environment*, Ph. D. Thesis, Bogazici University, in progress.

98. Bushberg, J. T., *The Essential Physics of Medical Imaging*, Wolters Kluwer Health, Philadelphia, 2011.

99. Lee, V. S., *Cardiovascular MRI: Physical Principles to Practical Protocols*, Lippincott Williams & Wilkins, Philadelphia, 2006.

100. Carmi, E., S. Liu, N. Alon, A. Fiat and D. Fiat, "Resolution enhancement in MRI", *Magnetic Resonance Imaging*, Vol. 24, No. 2, pp. 133–154, 2006.

101. Chabanova, E., S. B. Dorthe, E. Thisted, J. C. Holm and H. S. Thomsen, "MR Spectroscopy of Liver in Overweight Children and Adolescents: Investigation of 1H T2 Relaxation Times at 3T", *European Journal of Radiology*, Vol. 81, No. 5, pp. 811–814, 2012.

102. Zhao, J. M., C. S. Clingman, J. M. Närväinen, R. A. Kauppinen and P. C. M. van Zijl, "Oxygenation and Hematocrit Dependence of Transverse Relaxation Rates of Blood at 3T", *Magnetic Resonance in Medicine*, Vol. 58, No. 3, pp. 592–597, 2007.